DEPARTAMENTO DE ASTROFÍSICA

Universidad de La Laguna

El Papel de las Galaxias Satélites en la Formación de la Vía Láctea

Memoria que presenta
Dña. Margherita Bettinelli
para optar al grado de
Doctor por la Universidad de La Laguna.

INSTITUTO Đ ASTROFISICA Đ CANARIAS
mayo de 2019

Examination date: July, 2019
Thesis supervisors:
Dr. Sebastián L. Hidalgo
Prof. Santi Cassisi
Prof. Giampaolo Piotto

Contents

1 The Importance of Studying the Resolved Stellar Populations in Dwarf Galaxies of the Milky Way **13**
1.1 Introduction . . . 13
1.2 What is a Dwarf Galaxy? . . . 14
1.2.1 How are Local Group Dwarf Galaxies Classified? . . . 16
1.2.2 Dwarf Spheroidal Galaxies . . . 16
1.2.3 Dwarf Irregular Galaxies . . . 18
1.2.4 Ultrafaint Dwarf Galaxies . . . 20
1.2.5 Dwarf Elliptical Galaxies . . . 22
1.3 Small but Important for the Study of Galaxy Formation . . . 23
1.3.1 Monolithic Collapse Scenario . . . 23
1.3.2 Hierarchical Scenario . . . 27
1.3.3 Downsizing . . . 28
1.4 The Physical Phenomena that can shape the SFHs of Dwarfs Galaxies . . . 30
1.4.1 The Influence of Cosmic Reionization on the Early Evolution of Dwarf Galaxies . . . 30
1.4.2 SNe Feedback . . . 32
1.5 Thesis Work . . . 34

2 The Star Formation History of the Sextans Dwarf Spheroidal Galaxy: a True Fossil of the pre-Reionization Era **37**
2.1 Abstract . . . 37
2.2 Introduction . . . 38
2.3 Observations and Data Reduction . . . 39
2.4 The Colour-Magnitude Diagram . . . 40
2.5 Derivation of the SFH . . . 42
2.5.1 The Case of Sextans . . . 42

2.6 Confining the First Event of Star Formation 46
2.6.1 Radial SFH 49
2.7 Discussion 56
2.8 Summary and Conclusions 62

3 The Star Formation History of the Sculptor Dwarf Spheroidal Galaxy 63
3.1 Abstract 63
3.2 Introduction 63
3.3 Observations and Data Reduction 67
3.3.1 The Colour-Magnitude Diagram 70
3.4 Derivation of the SFH 70
3.4.1 The Global SFH of Sculptor 74
3.4.2 The Radial SFH of Sculptor 75
3.4.3 Constraining the duration of the main SFH burst 81
3.5 Discussion 88
3.6 Summary and Conclusions 95

4 The Canarias Einstein Ring: a Newly Discovered Optical Einstein Ring 97
4.1 Abstract 97
4.2 Introduction 97
4.3 Discovery 98
4.4 Follow-Up Spectroscopy 100
4.5 Analysis and Discussion 101
4.5.1 Lens 101
4.5.2 Source 102
4.5.3 Enclosed Mass Derivation 102
4.6 Conclusions 104

5 Comparison with other Galaxies 105
5.1 Overview 105
5.2 Comparison between Sextans dSph and Sculptor dSph 105
5.3 Metallicity-Luminosity Plane 106
5.4 Mass-Metallicity Relation 108

6 Conclusions 113
6.1 Summary and Conclusions 113

7 Future Work **117**
7.1 Future Work 117

8 Acknowledgements **119**
8.1 119

Bibliography **121**

A Methodology for the Derivation of the Star Formation History from the Colour-Magnitude Diagram of Resolved Stellar Systems **133**
A.1 The History of Star Formation Histories 133
A.1.1 The Synthetic Colour-Magnitude Analysis 134
A.2 Basic Concepts and Definitions 135
A.3 The Algorithms for the Obtaintion of the Star Formation History 136
A.3.1 IAC-star 136
A.3.2 Obsersin 138
A.3.3 MinnIAC 138
A.3.4 IAC-pop 141

Resumen

Esta tesis presenta el análisis de dos galaxias esferoidales de la Vía Láctea (VL): Sextans y Sculptor. La metodología seguida en ambos los casos es la misma y ha dado lugar a resultados científicos notables que se han publicado en revistas científicas arbitradas.

El ingrediente básico para este análisis está dado por la historia de formación estelar de las estrellas más antiguas a las más jóvenes. Para lograr esto, se necesitan diagramas color magnitud (DCM) profundos que alcancen los *turn-offs* mas viejos con suficiente precisión fotométrica.

Ambos estudios se han desarrollado partiendo de la fotometría terrestre de estas galaxias mediante el análisis de datos de gran campo desde el telescopio de clase 8 m Subaru y el telescopio 4 m Blanco para Sextans y Sculptor, respectivamente.

El primer paso consistió en la reducción de datos con el objetivo de obtener imágenes profundas de una buena parte de los objetos en estudio, compatibles con buena calidad de observación. Se ha realizado la fotometría de *Point-Spread Function*, obteniendo así dos catálogos: para Sextans en el sistema fotométrico Johnson (magnitudes B, V y I), y para Sculptor en el sistema fotométrico DECam (g y r magnitudes). Gracias a los DCM profundos que alcanzan el *turn-off* más viejo, en ambos casos, ha sido posible analizar la formación estelar hasta las épocas más remotas aplicando los algoritmos desarrollados por el grupo de Población Estelares al Instituto de Astrofísica de Canarias.

Se ha presentado un análisis detallado del primer evento de formación de estrellas en las dos galaxias satélite con el objetivo de identificar si estaba presente una escala de tiempo evolutiva común y mediante cálculos específicos dimos estimaciones sobre cómo los fenémenos físicos, como la retroalimentación de SNe, podrían haber influido en el destino final de estas galaxias.

Los resultados muestran que Sextans y Sculptor, aunque se consideran dSphs clásicos, son objetos diferentes. Ambas galaxias presentan gradientes radiales de poblaciones estelares pero a diferentes escalas radiales y con diferente intensidad. Hay fuertes indicios que sugieren la presencia, en ambas galaxias, de una población estelar pobre de metales primordial y extendida caracterizada por un evento bastante corto de formación estelar. Hemos podido restringirlo a 0.5 Gyr en Sculptor debido a su configuración compacta que nos ha permitido medir diferentes escalas temporales radiales de formación de estrellas, mientras que en Sextans calculamos una duración global de 0.6 Gyr, dentro de su core radius que se extiende hasta 27 arcmin. Esto indica un posible camino evolutivo común, también conocido como outside-in scenario.

Una investigación adicional que se ha llevado a cabo durante esta tesis es

el descubrimiento y la posterior confirmación de un anillo óptico de Einstein muy extendido. Este objeto ha sido descubierto durante la inspección visual de las imágenes profundas de Sculptor, lo que revela la gran potencialidad de estos datos en diferentes campos de investigación.

Este campo de investigación está bastante alejado del tema principal de la presente tesis, pero se ha decidido dedicar un tiempo de investigación a este descubrimiento debido a la peculiaridad de este objeto, principalmente a su simetría y extensión. Además, para confirmar su naturaleza, también hemos sido galardonados con tiempo discrecional del Director al Gran Telescopio Canarias (GTC), un telescopio de clase de 10 m. De esta manera, también tuve la oportunidad de manejar los espectros, para enriquecer mi experiencia personal sin afectar mi planificación doctoral.

Summary

This thesis presents the analysis of two dSphs galaxies of the Milky Way (MW): Sextans and Sculptor. The methodology followed is the same in both cases and it has led to remarkable scientific results that have been published on refereed scientific journals. The basic ingredient for this analysis is given by the star formation history (SFH) from the oldest stars to the youngest ones. To achieve this, deep colour-magnitude diagrams (CMDs) reaching the oldest main-sequence (MS) turn-offs (TOs) with sufficient photometric precision are needed.

Both studies have been developed starting from ground-based photometry of these galaxies by analizing deep wide-field data from the 8 m class telescope Subaru and 4 m telescope Blanco for Sextans and Sculptor respectively.

The first step consisted in the reduction of raw data with the objective to obtain deep stacked images of a good portion of the objects under study, compatibly with mean good seeing quality. It has been performed Point-Spread Function (PSF) photometry, thus obtaing two catalogues: for Sextans in the Johnson photometric system (B, V and I filters), while for Sculptor in the DECam photometric system (g and r filters). Thanks to the deep CMDs that reach the oldest MS TO, in both cases, it has been possible to analyze the star formation till the remotest epochs applying the algorithms developed by the Stellar Population group at the Instituto de Astrofísica de Canarias.

It has been presented a detailed analysis of the first event of star formation in the two satellite galaxies with the objective to identify if a common evolutionary time scale was present and trough targeted calculations we gave estimates on how physical phenomena, such as SNe feedback, could have influenced the final fate of these dSphs.

The results show that Sextans and Sculptor, even though are considered classical dSphs, are different objects. Both galaxies present radial gradients of stellar populations but at different radial scales and with different strength. There are strong hints that suggest the presence, in both galaxies, of an extended primordial metal poor stellar population characterized by a quite short event of star formation. We have been able to constrain it to 0.5 Gyr in Sculptor due to its compact configuration that has permitted us to measure different radial timescales of star formation, while in Sextans we calculated a global duration of 0.6 Gyr, within its core radius which is extended up to 27 arcmin. This indicates a possible common evolutionary path, also known as outside-in scenario.

An additional research that has been pursued during this thesis is the discovery and subsequent confirmation of an extended optical Einstein ring. This

object has been discovered during the visual inspection of the stacked images of Sculptor, thus revealing the great potentiality of this data in different fields of investigation.

Of coarse, this field of investigation is quite far from the main theme of the present thesis, but it has been decided to devote some time of investigation to this discovery because of the peculiarity of this object, mainly to to its symmetry and extension. Moreover, in order to confirm its nature, we have been also awarded with Director's discretionary time at the Gran Telescopio Canarias (GTC), a 10 m class telescope. In this way I also had the opportunity to handle spectra, so to enrich my personal expertise without affecting my doctoral planning.

Riassunto

Questa tesi presenta la analisi dettagliata di due galassie sferoidali della Via Lattea: Sextans e Sculptor. La metodologia seguita in ambo i casi è la stessa ed ha condotto a risultati scientifici rilevanti pubblicati su riviste scientifiche arbitrate. L'ingrediente base dell'analisi è dato dalla storia di formazione stellare, dalle stelle più vecchie fino alle più giovani. Per ottenere ciò sono necessari diagrammi colore magnitudine (DCM) che raggiungano il *turn-off* (TO) più vecchio con una sufficiente precisione fotometrica.

Entrambi gli studi si sono sviluppati partendo da fotometria da terra di queste galassie, analizzando immagini di grande campo di telescopi di 8 m come il Subaru e di 4 m Blanco, per Sextans e Sculptor, rispettivamente.

Il primo passo è stato la riduzione dei dati con l'obiettivo di ottenere immagini profonde di una buona porzione di questi oggetti, compatibilmente con una buona qualità di *seeing*. È stata effettuta fotometria di PSF, ottenendo così due cataloghi: per Sextans nel sistema fotometrico di Johnson (filtri B, V ed I), mentre per Sculptor nel sistema fotometrico di DECam (filtri g ed r). Grazie ai DCM profondi che raggiungono il TO più vecchio è stato possibile analizzare la formazione stellare fino alle epoche più remote applicando gli algoritmi sviluppati dal gruppo di Popolazioni Stellari all'Instituto de Astrofísica de Canarias.

È stata presentata una analisi dettagliata del primo evento di formazione stellare nelle due galassie satellite con l'obiettivo di identificare se un tempo scala comune fosse presente e mediante calcoli mirati si sono date stime di come fenomeni fisici, come il *SNe feedback*, possano aver influenzato il fato di queste galassie nane sferoidali.

I risultati mostrano che Sextans e Sculptor, sebbene siano considerata dSph classiche, sono in realtà oggetti diversi. Entrambe le galassie presentano gradienti di popolazioni stellare ma su scale radiali e con intensità differenti. Ci sono forti indizi che indicano la presenza, in ambo le galassie, di una popolazione stellare primordiale estesta e povera di metalli, caratterizzata da un evento di formazione stellare piuttosto breve. In questa tesi si è confinato tale evento di formazione stellare a 0.5 Gyr in Sculptor, grazie alla sua configurazione compatta che ci ha permesso di misurare differenti scale radiali di formazione stellare. Per Sextans, abbiamo invece calcolato una durata globale di 0.6 Gyr entro il suo core radius che si estende fino a 27 arcmin. Indicando già questo risultato una evoluzione rapida. Questi elementi suggerirebbero una possibile evoluzione comune, conosciuta anche come outside-in scenario.

Una ricerca che è stata condotta durante questa tesi riguarda la scoperta e seguente conferma di un anello di Eintein. Questo oggetto è stato scoperto

fortuitamente durante la ispezione visuale delle immagini profonde di Sculptor. Questo rivela la grande potenzialità di questi dati nei campi di investigazione più disparati.

Certamente questo campo di studio è piuttosto lontano dal tema principale della mia tesi, ma è stato deciso di dedicare un certo tempo allo studio di questa scoperta per via della peculiarità dell'oggetto, soprattutto per la sua estensione e simmetria. Inoltre, per confermare la sua natura abbiamo ottenuto tempo di Direttore al Gran Telescopio Canarias (GTC), un telescopio di 10 m. In questo modo ho avuto la possibilità di analizzare spettri e di arricchire la mia esperienza personale senza intaccare la mia pianificazione di dottorato.

List of Figures

1.1 Plot showing the absolute magnitude, M_V, vs. central surface brightness, μ_V plane 15
1.2 Sculptor dSph 19
1.3 Leo A dIrr galaxy 21
1.4 NGG205 Dwarf Elliptical 24
1.5 Scaled 3D representation of the Local Group 25
1.6 Angular momentum differences in the monolithic collapse scenario 26
1.7 Scheme illustrating the hierarchical galaxy formation scenario . 29
1.8 Stages of the evolution of a simulated dwarf 33

2.1 Observed CMD of Sextans dSph 41
2.2 Synthetic CMD with the simulated observational effects (black) with overplotted the observed CMD (red) 44
2.3 Results of the Sextans SFH 47
2.4 Hess diagrams relative to the observed CMD (left panel), best solution CMD (middle panel) and residuals CMD (right panel). The residuals are in units of Poisson uncertainties 48
2.5 Observed abundance ratios and the best-fit gas flow and SFH model for Sextans 50
2.6 Stellar properties of the Sextans dSph 51
2.7 Recovering of an input simulated star formation burst 52
2.8 $FWHM_{in}$ of the mock bursts and their associated mean recovered $FWHM_{rec}$ 53
2.9 Stars spatial distribution 54
2.10 Resulting SFH for the three regions 55
2.11 Original SFH, obtained without assuming any a priori MDF (in black) and the SFH derived imposing the MDF by Kirby . . . 57
2.12 Cumulative mass fraction as a function of the lookback time . . 58

2.13 Regions of the gas mass (M_g) - mechanical luminosity of the starburst (L) plane in which blowout or blow-away can occur . 61

3.1 HI surface densities in Sculptor from Carignan et al. (1998) . . 65
3.2 Calibrated magnitudes plotted against the corresponding photometric errors 66
3.3 Calibrated CMD of Sculptor 71
3.4 Synthetic CMD with observational effects simulated with over plotted the observed CMD of Sculptor 73
3.5 Total SFH for Sculptor 75
3.6 Hess diagrams relative to the observed CMD (left panel), best solution CMD (middle panel) and residuals CMD (right panel). The residuals are in units of Poisson uncertainties. Residuals from $\sigma = 0$ to $\sigma = 3$ refer to the case in which the model predicts more stars in respect to the oCMD. Residuals from $\sigma = 0$ to $\sigma = -3$ refer to the case in which the model predicts less stars in respect to the oCMD. Gray levels show the density of stars. A factor of 2 in density exists between each two successive gray levels. The single dots are shown where the density is less than 2 stars per $(0.02)^2$ mag. The boxes show the areas of the CMD used for the derivation of the SFH. 76
3.7 Stellar spatial distribution 77
3.8 From left to right CMDs of Sculptor from the innermost elliptical region to the outer 78
3.9 CMDs of the inner and outer regions of Sculptor from Hurley-Keller et al. (1999) 80
3.10 Resulting radial SFH as a function of the look-back time 81
3.11 Resulting radial metallicity as a function of the look-back time 82
3.12 Resulting radial cumulative mass fraction of Sculptor 83
3.13 Hess diagrams relative to the CMD of the stars within $a \leq 8.59$ arcmin, see green points in Figure 3.7 (left panel), best solution CMD (middle panel) and residuals CMD (right panel). The residuals are in units of Poisson uncertainties. 84
3.14 Same as in Figure 3.13 but for stars within $8.59 < a \leq 13.41$, see magenta points in Figure 3.7 85
3.15 Same as in Figure 3.13 but for stars within $13.41 < a \leq 19.35$, see blue points in Figure 3.7. 85
3.16 Same as in Figure 3.13 but for stars within $a \geq 19.35$, see red points in Figure 3.7 86

3.17 $FWHM_{in}$ is the Full Width at Half Maximum of the input mock bursts, $FWHM_{rec}$, the recuperated FWHM relative to the SFH of each mock bursts. Points have been fitted with a quadratic polynomial. Knowing the FWHM of the best SFH solution, making use of the intercept on the fitting red line (see green box) we confine the star formation burst to a value of $FWHM_{in}^{obs} \sim$ 1.4 Gyr for region 1. 89
3.18 Same as Figure 3.17 but for region 2; we confine the star formation event to a value of $FWHM_{in}^{obs} \sim 1$ Gyr 90
3.19 Same as Figure 3.17 but for region 3; we confine the star formation event to a value of $FWHM_{in}^{obs} \sim 0.8$ 91
3.20 Same as Figure 3.17 but for region 4; we confine the star formation event to a value of $FWHM_{in}^{obs} \sim 0.5$ Gyr. 92
3.21 This figure summarizes the results achieved. The points represents the duration of the star formation in each region and a function of the distance from the center of Scultor. The horizontal error bars refer to the radial coverage of each individual region. 93
3.22 Observed abundance ratios and the best-fit gas flow and SFH model for Sculptor from Kirby et al. 2011 96

4.1 Composite g, r field of view of 2.5 arcmin $\times$ 2.5 arcmin centered on the Canarias Einstein ring 99
4.2 Resuling spectra of source and lense properly fitted with templates from literature 101
4.3 Best fitting SIE model obtained with the `gravlens/lensmodel` software 103

5.1 Comparison between the SFHs and the AMRs of Sextans and Sculptor 107
5.2 Absolute visual magnitude vs. stellar metallicity measurement 109
5.3 Mass-metallicity Relation 110

A.1 Data flow diagram of the methos used to derive the SFH 137
A.2 SFH of the global synthetic population associated with the sCMD 139
A.3 CMD of a global synthetic population (sCMD) 140

List of Tables

2.1 Sextans parameters 39
2.2 Observations 40
2.3 Parameters used for calibrating the photometry with the associated errors 41
2.4 Box sizes in each bundle that sample the observed CMD 46
2.5 Mass percentiles formed in Sextans as a function of redshift and look-back time. 46

3.1 The main properties of the Sculptor dSph 67
3.2 A summary of the available observational datasets 68
3.3 Parameters used for calibrating the photometry with the associated errors 69
3.4 Box sizes in each bundle that sample the observed CMD 74
3.5 Ratios between the number of stars in the RHB, BHB and the spur region in respect to the RGB 79
3.6 List of the recuperated FWHM relative to the SFH of each mock bursts for each elliptical region. 87
3.7 Constrainment of the period of star formation for each elliptical region. $FWHM_{rec}$ refers to the real measured $FWHM$ for each SFH, while $FWHM_{in}$ is the associated constrained burst found by means of the quadratic fit. We also provide the errors associated to $FWHM_{in}$ in the last column. 87

4.1 List of parameters 99

5.1 Mass percentiles formed in Sextans and Sculptor as a function of look-back time. 106

1

The Importance of Studying the Resolved Stellar Populations in Dwarf Galaxies of the Milky Way

1.1 Introduction

Dwarf galaxies are the more common and diffused type of galaxies in the Universe. Precisely for this reason, their deep understanding could strongly influence the theories of galaxy formation and evolution.
In the Λ cold dark matter (ΛCDM) scenario dwarf galaxies are building blocks of larger systems (Blumenthal et al. 1985, Navarro et al. 1997). Seen in this light, they are the survivors of early merging processes that led to the formation of bigger galaxies such as the Milky Way (MW).

Thanks to their proximity, MW satellite galaxies, can be resolved into stars. From deep colour-magnitude diagrams (CMDs) reaching the oldest main sequence (MS) turn-off, the star formation history (SFH) can be derived displaying all the stars born during the lifetime of the system (Hidalgo & Aparicio 2016). The SFH englobes several pieces of information, such as the rate at which stars form as a function of the time and the metallicity distribution of those stars also as a function of the time. In particular, in this thesis work, it is given relevance to the investigation of the first gigayears of star formation of the two dSphs, Sextans and Sculptor, because from the properties of their ancient stellar populations can be estimated the impact of a variety of different

physical mechanisms, such as the heating coming from the cosmic ultraviolet (UV) background radiation arising from the earliest star formation in the Universe (Bullock et al. 2000) and internal supernova (SN) feedback (Mac Low & Ferrara 1999).
The early time resolution of observationally derived SFHs is limited by many factors, in particular by the data used (Aparicio et al. 2016). So, a direct comparison of observationally derived SFHs with those derived from theoretical models of galaxy formation can be potentially biased. In this sense, it is of fundamental importance to correctly quantify the *observational effects* (Aparicio & Hidalgo 2009). Observational effects include limited signal-to-noise, incompleteness, source blending, image read-out noise as well as not fully removed artifacts in the data reduction process (flat-field correction, etc.). All together, their effects on the CMD are the loss of stars and dispersion and shift of points, all depending on magnitude and color.

This kind of studies is of great importance for an improvement of the understanding of the first stages of formation of larger galaxies such as the MW and the physical processes connected that regulate star formation. Still it lacks a global view capable to explain and connect the various morphologies of dwarf galaxies. The fixed point for all dwarfs of the LG is the fact that in the $M_V - \mu_V$ plane they overlap along a straight line (see Fig. 1.1), thus suggesting a continuity of structural properties from dSph to larger spheroidal and late-type systems, dominated by physical processes that scale with mass.

1.2 What is a Dwarf Galaxy?

Classically, the term *dwarf galaxy* refers to galaxies of small intrinsic size, small absolute luminosity, low surface brightness and a luminosity of $M_V \gtrsim -15$ (Hodge 1971). Subsequently, Tammann (1994) gave a working definition: all galaxies fainter than $M_B \leq -16$ ($M_V \leq -17$) and more extended than globular clusters (GC) are considered dwarf galaxies.

Mateo (1998) discussed the fact that dwarf galaxies, unlike globlular clusters, are dark matter (DM) dominated. This valorates the uncontroversional fact that dwarf galaxies are effectively *galaxies* following the well-defined relation between absolute magnitude M and central (or mean) surface brightness μ (Binggeli 1994). In fact, as follows from the works by Kormendy (1985) and Binggeli (1994), Tolstoy et al. (2009) shown in Figure 1a in her review (which is reported in Fig. 1.1) that there is no discontinuity with all the other galaxies. In particular early- and late-type dwarfs appear to fall along similar relations, overlapping with blue compact dwarf (BCD) and larger late-type systems, as well as faint spiral galaxy disks and those galaxies defined as spheroidals.

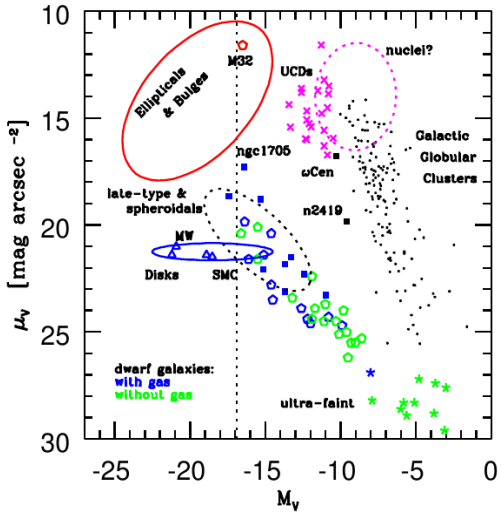

Figure 1.1: The plot taken from Tolstoy et al. (2009), shows the absolute magnitude, M_V, vs. central surface brightness, μ_V plane. The dotted line refers to the classical limit of the dwarf class as defined by Tammann (1994). Marked with coloured ellipses are the typical locations of elliptical galaxies and bulges (red), spiral galaxy disks (blue), galactic nuclei (dashed magenta) and large early (spheroidals) and late-type systems (dashed black). Galactic GCs are plotted individually as small black points. M 31, the MW, M 33 and the Large Magellanic Cloud (LMC) are shown as blue open triangles. Some of the BCDs with well studied CMDs are marked as blue solid squares. The peculiar GC ω Cen and NGC 2419 are marked close to the GC ellipse; M 32 in the region of Elliptical galaxies; the Small Magellanic Cloud (SMC) near the border of the dwarf class. The Ultra-compact dwarfs (UCDs) studied in the Virgo and Fornax clusters are marked with magenta crosses. LG dwarf galaxies are plotted as open pentagons, blue for systems with gas and green for systems without gas. The recently discovered uFds are given star symbols, and the same colour code.

1.2.1 How are Local Group Dwarf Galaxies Classified?

The LG contains basically three types of dwarf galaxies, as described in detail in Grebel (2001): dwarf spheroidal galaxies (dSphs), dwarf elliptical galaxies (dEs) and dwarf irregular galaxies (dIrrs). In the last decade have been discovered a huge number of so called ultra-faint dwarf galaxies (UFDs); UFDs of the MW include dwarf galaxies and star clusters as well as objects with intermediate properties. In the following section dSph galaxies will be presented in detail, since they are the main actors in this thesis (see Section 1.2.2); subsequently in Section 1.2.3 dwarf irregulars (dIrrs) will be described; in Section 1.2.4 an overview on uFds is given; in Section 1.2.5 are presented the dEs class. Finally in Section 1.5 is resumed the thesis work done.

1.2.2 Dwarf Spheroidal Galaxies

This thesis is centered on the detailed study of two close dSphs of the MW, Sextans and Sculptor, motivated by the fact that these objects, believed to be the most DM dominated stellar system known, are the key to understand the formation of larger galaxies. They are, at present, the smallest cosmological structures containing DM in the Universe, with mass-to-light ratios of $M/L_V \sim 10^{1-2}$ (Mateo 1998; Łokas 2009; Walker et al. 2009).

DSphs are defined as diffuse, gas deficient, low surface brightness dwarfs characterized by a low central stellar concentration (Grebel 2001). They are defined *early-type dwarf galaxies* as remarking the fact that they lack gas and recent star formation (van den Bergh 1999;Tolstoy et al. 2009).
Gallagher & Wyse (1994) define a dSph as a galaxy with $M_B > -14$ mag, low optical surface brightness ($V \geq 22$ mag arcsec^2) and no well defined nucleus.

DSphs' estimated masses, considering both the stars and the DM halo, are of the order of $10^7\,M_\odot$ to $10^8\,M_\odot$, within their half-light radii. Being objects not rotationally supported (Grebel et al. 2003), are indeed pressure supported. Interestingly, it has been measured that dSphs characterized by different total luminosities have a very similar stellar velocity dispersions of the order of 10 km s^{-1}, which remains approximately constant with the distance from the center of the galaxy (Muñoz et al. 2005; Walker et al. 2006a; Walker et al. 2006b; Muñoz et al. 2006; Walker et al. 2007). This suggests that the DM halos in dSphs are very similar, unlike their stellar component that can strongly vary from case to case.

DSphs are among the closest systems to us (within 200 kpc) in a sort of *morphological segregation* in rispect to other dwarfs types (Grebel 2001), but have been discovered very distant, isoleted dSph such as Cetus and Tucana,

which display all the characteristics common to the closest dwarfs, but at distances of the order of ~ 800 kpc, so well beyond the halo of the MW. The SFHs found for Cetus and Tucana show that their stellar population is predominantly old (Monelli et al. 2010a; Monelli et al. 2010b).

Historically, Sculptor (shown in Fig. 1.2) , Carina, Draco, Fornax, Leo I, Leo II, Sextans and Ursa Minor are considered as the prototypical dSphs. But each of the aforementioned dwarfs present peculiarities in their stellar populations that makes complicate the construction of a sharp classification, even if they belong to the same morphological type and they have similar luminosities (Grebel 1997).

This fact is well represented by Ursa Minor, Carina, Sextans and Draco, whose luminosities are very similar, $M_V = -8.8$, -9.1, -9.3 and -8.8 respectively (McConnachie 2012), but their SFHs quite different.

Ursa Minor's SFH is characterized by a single major burst of star formation about 13.5 Gyr ago with a duration of less than 2 Gyr (Mighell & Burke 1999); Carrera et al. (2002) found that 90% of the stars were formed before 13 Gyr ago. Carina's SFH consists of at least three separate episodes of star formation with the star fomation rate (SFR) apparently going to zero in between (Smecker-Hane et al. 1996; Hurley-Keller et al. 1998; Norris et al. 2017).

Sextans has been demontrated in Bettinelli et al. (2018) to be a true fossil of the pre-reionization era, as defined in Ricotti & Gnedin (2005); Bettinelli et al. (2018) have confined the first event of star formation to 0.6 Gyr. If compared to Sextans, Ursa Minor seems to have had a faster evolution, this fact is confirmed also by the results by Kirby et al. (2011a) who deduced that almost all the star formation of Ursa Minor occured over an interval of 0.4 Gyr, while for Sextans found 0.8 Gyr.

Draco, similarly to Ursa Minor, has a stellar mass comparable to a GC, of the order of $0.3 \times 10^6\ M_\odot$. Most of the star formation in Draco took place before ~ 10 Gyr ago (Aparicio et al. 2001). Kirby et al. (2011a) through their chemical evolution models found a star formation duration of 0.7 Gyr, thus closer to the case of Sextans.

Fornax is the brightest and most massive dSphs of the MW and the only known dSph, together with Sagittarius, to contain GCs. Fornax is almost intact, while Sagittarius is undergoing tidal disruption due to the interation with the Galaxy. Fornax displays an extended SFH, dominated by star formation at intermediate age (1 - 10 Gyr) (de Boer et al. 2012a; del Pino et al. 2013).

Leo I presents a large population of ancient (> 10 Gyr old) stars (Gallart et al. 1999); although this dwarf formed stars until recent epochs, ending only ~ 0.5 Gyr ago, it experienced most of its star formation at early epochs, $10 - 14$ Gyr ago (Smecker-Hane et al. 2009).

Finally, in order to complete this overview on the SFHs of the considered *classical* dSph galaxies, Leo II and Sculptor are still missing. These two dwarfs share a similar metallicity distribution function (MDF) Kirby et al. (2011a). Mighell & Rich (1996) estimated for Leo II an extended star formation of ~ 7 Gyr, while Kirby et al. (2011a) confined the initial burst to 1.6 Gyr, one of the longest duration measured for the sample of eight classical dwarf. The authors argue that the above duration could be subdivided in an array of short bursts, as shown in the work by Revaz et al. (2009), where a model with ~ 13 star formation episodes matches well the abundances by Shetrone et al. (2009). Sculptor, which is the second case analyzed in this thesis, presents a shorter period of star formation than Leo II. From our estimates the very first episode of star fomation lasted ~ 0.5 Gyr and produced the extended metal poor stellar structure of the galaxy; star formation in the central region lasted ~ 1.4 Gyr (Bettinelli et al. submitted). Kirby et al. (2011a) found a mean duration of the main burst of 1.1 Gyr, thus in accordance with our results.

In definitive, what appears from this brief summary on the SFHs of the so called *classical* dSph, is that there is no two dSph galaxies having the same SFH! There are systems that have the same luminosities, but completely different SFH; or systems characterized by the same MDF, and even in this case slightly different SFH.

Still lacks an exhaustive model capable to explain all these peculiarities, or to find some systematics. But implementing the results coming from the cosmological simulations, the chemical evolution models and the star formation histories, it will be possible to construct a consistent view for each case above. This is surely the starting point for the derivation of a global view of the various physical phenomena that intervene in the galaxy formation and evolution.

1.2.3 Dwarf Irregular Galaxies

DIrrs are galaxies characterized by an irregular appearence, as suggests its nomenclature, and by the presence of extended HI regions and scattered bright HII regions in the optical, thus indicating the presence of undergoing star fomation. These gas-rich dwarf galaxies are usually located far from either the MW or M31, contrarily to dSphs, as indicating a LG position-morphology relation, firstly highlighted by Einasto et al. (1974). This type of behaviour has been connected to environmental effects (Bouchard et al. 2009), but as discussed in Grebel et al. (2003), the removal of the interstellar medium (ISM) from a given dwarf would not produce a non rotating object; moreover, dSph are too metal rich for their luminosity in comparison to the old population of dIrrs galaxies,

Figure 1.2: This image, taken with the Wide Field Imager camera on the 2.2 m MPG/ESO telescope at European Southern Observatory (ESO)'s La Silla Observatory in Chile, shows the Sculptor dwarf galaxy. Image credit: ESO.

thus suggesting that the early evolution of early- and late-type galaxies has been different and not just due to environment.

They are typically at distances > 400 kpc, where the SMC is an exception being at ~ 64 kpc. Two interesting cases for which deep CMD reaching the oldest MS turn-off are Leo A and LGS-3.
Leo A (see Fig. 1.3) is a small ($M_* = 6 \times 10^6\ M_\odot$) blue dIrr galaxy located at a distance of 798 Kpc. Cole et al. (2007) found that 90% of the star formation in Leo A happened during the past 8 Gyrs. Moreover, at earliest times the star formation was small, as shown by the weak horizontal branch (HB), even though the presence of ancient stars has been confirmed by the detection of RR Lyrae variable stars (Dolphin et al. 2002).
LGS-3, in classified as a transition type (dIrr/dSph) galaxy because it contains HI gas but no HII , so there are no star forming regions. Hidalgo et al. (2011) derived the SFH of LGS-3 from deep Hubble Space Telescope (HST) observations and found that the galaxy formed the 90% of the stars in a main episode of star formation ~ 11.7 Gyr ago which lasted 1.4 Gyr. Subsequently, LGS-3 continued forming stars until the present, although at a much lower rate.

1.2.4 Ultrafaint Dwarf Galaxies

In the last decade have been discovered dozens of new Ultrafaint Dwarf Galaxies (UFDs). This has been possible thanks to a systematical scanning of the sky through surveys like the Sloan Digital Sky Survey (SDSS: Abazajian et al. (2009)), the Panoramic Survey Telescope and Rapid Response System (Pan-STARRS: Kaiser et al. (2010)) and the Dark Energy Survey (DES: Flaugher et al. (2012)).
These dwarfs are characterized by a very poor stars statistics and low surface brightness. In appearence they resemble more a diffuse metal-poor GC than a dwarf galaxy, so, in order to confirm the effective nature of these objects, that means, the presence or not of dark matter, a spectroscopic follow-up is needed. UFds in the $M_V - \mu_V$ plane are placed in the region of lowest absolute magnitudes and surface brightness. Nevertheless, they appear to be the natural extension of the dSph sequence at lower luminosities and not another class of distinct objects.

Brown et al. (2014) has derived for a sample of six uFds (Bootes I, Canes Venatici II, Coma Berenices, Hercules, Leo IV and Ursa Major I) deep HST CMDs and constrained the SFHs of each of them, making use also of spectroscopic data. The CMDs of these objects appears at a first inspection very similar, dominated by an ancient metal-poor population. The spectroscopy has confirmed that these galaxies are composed by very metal-poor stars ($[Fe/H] \sim$

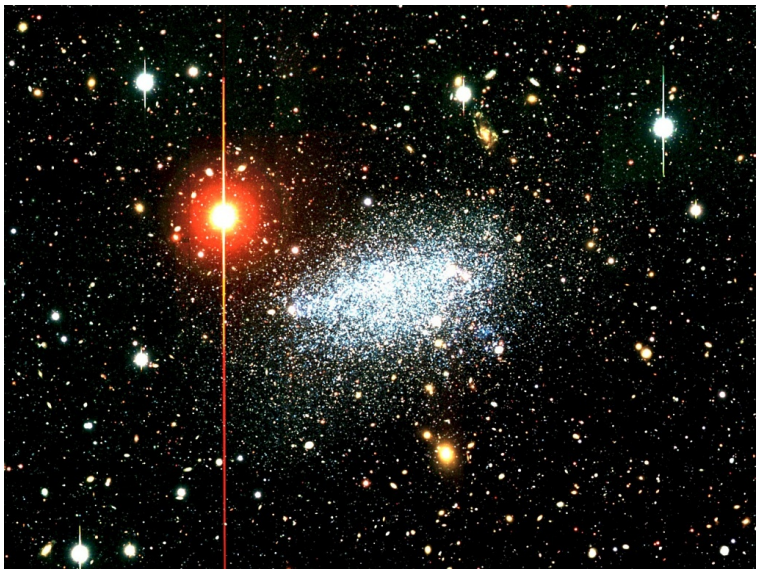

Figure 1.3: Colour image, taken with the Suprime-Cam camera on the 8.2 m Subaru telescope shows the Leo A dwarf irregular galaxy. Image credit: National Atronomical Observatory of Japan.

-2.5). Moreover they found for five galaxies that the majority ($> 75\%$) of the stars formed prior to $z \sim 10$ when the epoch of reionization began (13.3 Gyr ago).
This result classifies these galaxies as *true pre-reionization fossils*, as defined in Ricotti & Gnedin (2005). Finally, an interesting question is if the ancestors of uFds could have played a decisive role in reionizing the early Universe as discussed in (Weisz & Boylan-Kolchin 2017).

1.2.5 Dwarf Elliptical Galaxies

For completeness it is deserved a brief overview on dEs class. Generally, low luminosity elliptical galaxies are distinguished from late-type galaxies (spirals and irregulars) by their smooth surface brightness profiles. Below luminosities of $M_B \sim -18$ the smooth-profile galaxies divide into two classes: compact galaxies with high central surface brightnesses (exemplified by M32), and diffuse galaxies with low central surface brightnesses (exemplified by the LG dwarf spheroidals, see Section 1.2.2). The terms *dwarf elliptical* and *dwarf spheroidal* have been used most often to describe smooth, low surface brightness galaxies. However, the lack of a universally accepted definition has led to some confusion over whether these terms refer to the same thing, and in particular whether the dE class includes galaxies like M32.

Actually the class named dEs (compact dEs) refers to objects like NGC205 (shown in Fig. 1.4), NGC147, NGC185 and M32, which are all close to Andromeda. The former three galaxies have fundamental plane properties that indicate similarity to galaxies in the dSph class by contrast, galaxies such as M32 have properties that indicate similarity to (giant) elliptical galaxies. This likely indicates a difference in formation history, as discussed in Kormendy et al. (2009). The prototype of the dE galaxy class is NGC205 which is in very close projection to Andromeda (40 arcmin $\sim$ 8 kpc). Both photometric and kinematic evidence suggests that NGC205 is tidally interacting with M31 (Geha et al. 2006), and may in fact be on its first orbital approach (Howley et al. 2008). In contrast, NGC147 and NGC185 lie at a projected distance of 7 degrees (150 kpc) from Andromeda. These two galaxies are physically separated by over 60 kpc and they share several similar fundamental properties, such as absolute luminosity ($M_V \sim -15.5$), half-light radius ($r_{eff} \sim 2$) arcmin or 3 kpc, and central velocity dispersion. However, they differ in many other aspects: NGC185 contains some gas, dust and evidence for recent star formation confined to its center (Martínez-Delgado et al. 1999), while NGC147 is devoid of gas or dust and shows no sign of recent star formation activity (Sage et al. 1998). An average metallicity of $[Fe/H] = -1.4$ is inferred for NGC185 (Martínez-Delgado

et al. 1999), while a more metal rich population of $[Fe/H] = -1.0$ is inferred for NGC147 (Gonçalves et al. 2007). HST/WFPC2 imaging of both galaxies also implies the presence of intermediate-age stars, with NGC147 having a more significant contribution than NGC185 (Butler & Martínez-Delgado 2005). While both dEs are dominated by old to intermediate-age stars, the metallicity and age mixture of these components are different in each galaxy. Geha et al. (2010) found for the first time for NGC147 and NGC185 a significant internal rotation but this manifests only at several times the effective radius. Geha et al. (2010) suggest a formation mechanisms in which dEs are transformed or stripped versions of gas-rich rotating progenitor galaxies.

1.3 Small but Important for the Study of Galaxy Formation

Dwarf galaxies although being 'small' systems give great impulse to the improvement of cosmological theories. One of the main cosmological interest is related to the possibility that today's dwarfs are the survivors of the *building blocks* of massive galaxies. CDM cosmology predicts that dwarf systems are the first ones to form after Big Bang, since only dark matter halos of mass smaller than $10^8 M_\odot$ are able to condense from primordial density perturbations. So, more massive systems derived from the merging of these protogalactic fragments (White & Rees 1978; Frenk et al. 1988). Satellites have therefore a major role and are predicted to continuously interfere with galaxy evolution. Observations show that effectively small galaxies are located all around bigger galaxies, being the closest laboratory the LG, see Figure 1.5. In the case of the MW is remarkable the accretion of the Magellanic Stream and Sagittarius.

Furthermore, the study of dwarf galaxies permits to investigate other physical phenomena that shape the SFHs at different mass scales, like the ultraviolet (UV) background during the epoch of reionization (Bullock et al. 2000; Gnedin & Kravtsov 2006), the supernova feedback (Governato et al. 2010; Sawala et al. 2010) as well as local UV heating and winds from young stars.

In the following sections are discussed the two most relevant theories of galaxy formation of the last decades, the *monolithic collapse*, the already anticipated *hierarchical-merging scenario* and a recall to the *downsizing* phenomenon. Finally, we will discuss in detail the physical phenomena that can shape the SFHs of dwarfs galaxies and can provide clues on their past evolution.

1.3.1 Monolithic Collapse Scenario

Prior to CDM, the classic model of galaxy formation was the so called monolithic collapse published by Eggen, Lynden-Bell and Sandage in 1962 (Eggen

Figure 1.4: Color composite of CCD images of NGG205 from the 0.9 m telescope of the Kitt Peak National Observatory Image credit: NOAO/AURA/NSF

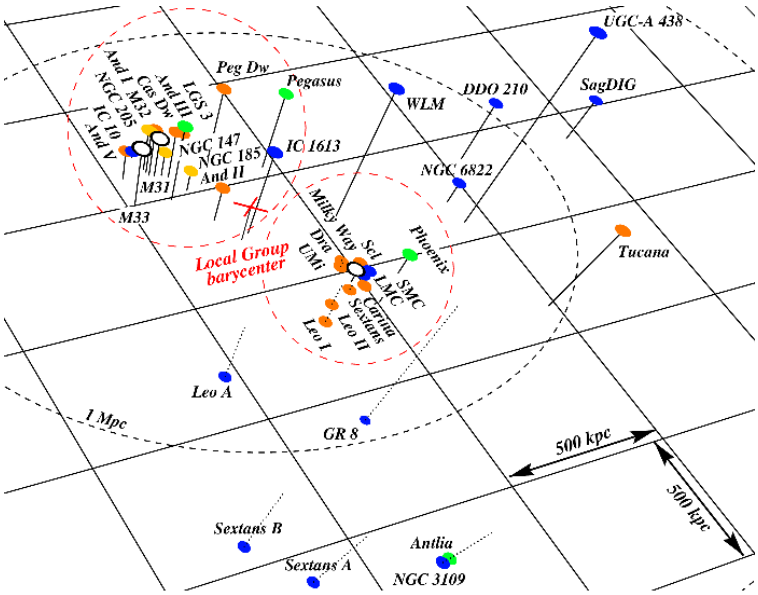

Figure 1.5: Scaled 3D representation of the Local Group (LG) taken from Grebel (1999). The dashed ellipsoid marks a radius of 1 Mpc around the LG barycenter (cross). The underlying grid is parallel to the plane of the MW. Galaxies above the plane are indicated by solid lines and below with dotted lines. The dashed circles enclose the presumed M31/M33 and the MW subsystem. Morphological segregation is evident: The dEs and gas-deficient dSphs (light symbols) are closely concentrated around the large spirals (open symbols). DSph/dIrr transition types (e.g., Pegasus, LGS 3, Phoenix) tend to be somewhat more distant. Most dIrrs (dark symbols) are isolated and located at larger distance

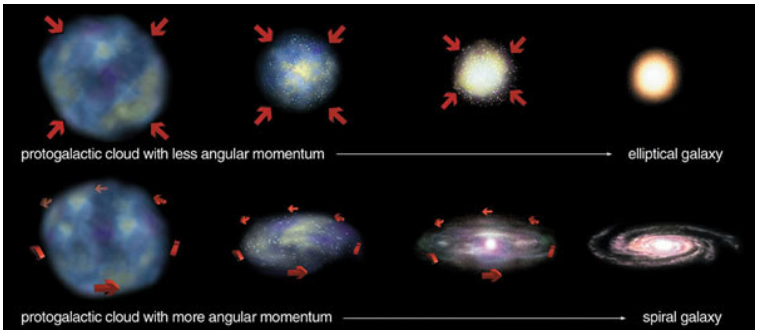

Figure 1.6: Difference in angular momentum content may account for the differences between spiral and elliptical galaxies. Protogalactic gas clouds born with more angular momentum may have formed a pancake-like disk first before most of stars were formed. Copyrights Pearson Education, publishing as Eddison-Wesley.

et al. 1962) who studied the motions of a sample of high-velocity stars. They found a correlation between metallicity and orbital eccentricities and angular momentum and inferred that the Galaxy formed quickly, through the collapse of a uniform, isolated protogalactic cloud. In other words, the gravitational collapse of a cloud of primordial gas very early in the lifetime of the Universe formed all parts of each galaxy at the same time. The morphology of the forming galaxy is determined by the angular momentum of the protogalactic cloud. If the gas is turned into stars on timescales longer than the dynamical timescale of the cloud, with high angular momentum, this led to the formation of a disk galaxy. Subsequently, dissipational processes stabilize the gas in a disk where star formation continues and deplete the remaining enriched gas to form subsequent stellar populations. If the galaxy forms with low angular momentum on timescales considerably shorter than the the dynamical timescale of the parent gas cloud, then the collapse preferentially leads to the formation of a spheroidal galaxy through violent relaxation processes (Lynden-Bell 1967), see Figure 1.6. In this scenario, the majority of stars in early-type galaxies is expected to form early, at redshifts $z \gtrsim 2$, with the most massive structures forming first (top-down scenario).

1.3.2 Hierarchical Scenario

Hierarchical structure formation is a generic feature of CDM models. Theoretical work relies on the hypothesis that dark matter and galaxies are linked, because gravitating concentrations of dark matter originating soon after the Big Bang are responsible for the formation of galaxies. In this picture (see Figure 1.7), small concentrations of dark matter grow slowly at first, being gradually compressed by self-gravity. However, when the concentrations reach a critical density (about 200 times the mean background density of the Universe), they undergo a catastrophic non-linear collapse, which results in the formation of an extended "halo" of dark matter. Over time these halos clump together under their mutual gravitational attraction, merging to form a hierarchy of larger halos. The rate of cooling of hydrogen gas drawn into these large halos governs the assembly of normal galaxies, and ultimately their morphology. The fact that galaxies form hierarchically means that low-mass DM halos collapse earlier and merge to form increasingly larger systems over time, from ultrafaint dwarfs to clusters of galaxies (Blumenthal et al. 1985). Ordinary matter in the Universe follows the dynamics dictated by the dark matter until radiative, hydrodynamic, and star-formation processes take over (White & Rees 1978).

Thus a galaxy like our Milky Way was formed by accreting a large number of small galaxies. Depending on the masses of the accreted dark matter haloes they either merge quickly with the main galaxy or they spend a long time orbiting around it (Boylan-Kolchin et al. 2008). This model provides a successful framework to describe the formation and evolution of dark matter haloes, which are the hosts of galaxies. For Milky Way mass haloes and above, the predictions are in good agreement with observations, while for dwarf galaxies the theory nominally predicts too many luminous field and sub-haloes, thus generating the so called *missing satelling problem* (Klypin et al. 1999).

Furthermore, the apparent excess of substructures in ΛCDM is not just limited to the lowest mass scales: simulations also predict the presence of subhaloes so massive that they should not be affected by re-ionization and hence considered, the so called *too big to fail* problem (Boylan-Kolchin et al. 2011), but whose internal structure seems incompatible with that of the brightest observed satellite. High resolution hydro-dynamical simulations of the LG such as APOSTLE (Sawala et al. 2016) demonstrated that the ram pressure and tidal stripping of the haloes orbiting their host galaxy, together with the reduction of their mass due to UV-background heating and stellar feedback, strongly reduce the faint tail of the luminosity function.

Another interesting argument, whose reality is still debated, is the *core-cusp problem* (Pineda et al. 2017), that may be solved by a very bursty star

formation history induced by a strong feedback (SN explosions may be able to dynamically heat the central cusp, expanding the orbits of DM particles), tranforming the central cusp into a large density core (Pontzen & Governato 2014). This is because, on one hand, DM haloes assembled in cosmological simulations exhibit *cuspy* radial density profiles which steeply increase towards the center, being well represented by the Navarro-Frenk-White (NFW) fitting formula with an asymptotic behaviour of $\rho_{inner} \propto r^{-1}$ (Navarro et al. 1996). On the other hand, kinematic observations of dwarf spheroidals (via stellar velocity dispersions) seem to be more compatible with core-like DM haloes ranging from $\rho_{inner} \propto r^{0}$ to $\rho_{inner} \propto r^{-0.3}$ (Flores & Primack 1994).

An interesting case to be recalled here is the one of Sculptor, for which has been found hints of the presence of a core profile (Battaglia et al. 2008a;Walker & Peñarrubia 2011; Amorisco et al. 2014) and according to other studies a NFW profile is consistent with the observations (Strigari et al. 2014;Richardson & Fairbairn 2014). Very recently Strigari et al. (2018) stated that is not possible to distinguish between cored and cusped potentials with the proper motion data at disposal. The problem is still open.

At the light of all these argumentations, it is important the investigation of the star formation history of dSphs and how the various physical phenomena have contributed to the shaping of dwarf galaxies as seen nowadays.

1.3.3 Downsizing

One of the most intriguing aspects of galaxy formation is the so called downsizing of galaxies. While in a hierarchical galaxy formation scenario the first haloes to form are the smallest ones, there is observational evidence in favor of more massive, early-type galaxies being in place before smaller galaxies. Moreover, it has been shown that stars in most massive galaxies tend to have formed earlier and on a shorter time span (Thomas et al. 2010). However, as discussed in Cattaneo et al. (2008), the downsizing of elliptical galaxies is not in conflict with the standard hierarchical clustering scenario. This is motivated as a natural outcome of the shutdown of star formation in haloes above a critical mass of $\sim 10^{12}\, M_{\odot}$.

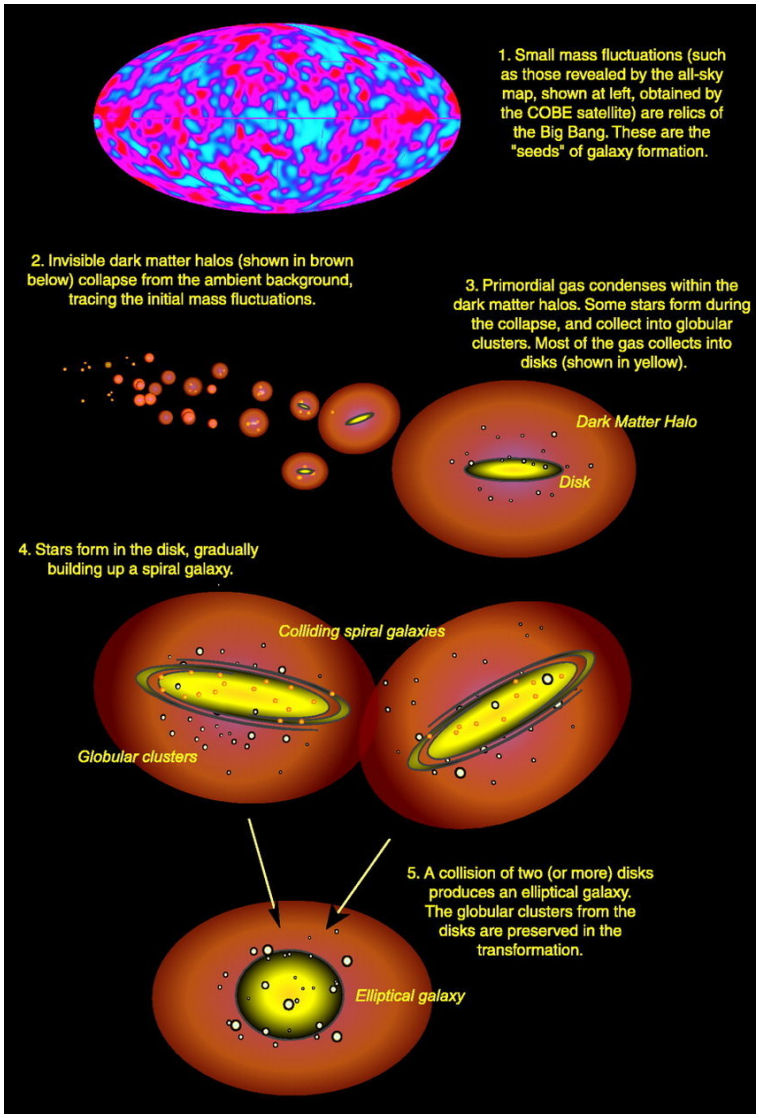

Figure 1.7: Schematic view of the hierarchical galaxy formation process from Abraham & van den Bergh (2001).

1.4 The Physical Phenomena that can shape the SFHs of Dwarfs Galaxies

1.4.1 The Influence of Cosmic Reionization on the Early Evolution of Dwarf Galaxies

Ultraviolet (UV) background radiation coming from Reionization of the Universe is thought to shape the early evolution of low mass galaxies, as it has been investigated extensively through the years. With time, the expected imprint of the UV radiation on the SFHs of dwarf galaxies has evolved.

Early studies predicted that UV background could be capable to completely quench star formation in sufficiently low mass galaxies. Efstathiou (1992) and Babul & Rees (1992) discussed analytically the possibility that a photoionizing background might significantly affect the formation of dwarf galaxies and may be the mechanism preventing the collapse of most of the baryonic material into subgalactic objects at high redshifts. According to the scenario outlined in Ferrara & Tolstoy (2000) the first stars in observed dwarf galaxies formed prior to reionization. Star formation at later epochs originates from new gas infall as the metagalactic UV background radiation field decreases. In this way, it would be straightforward to motivate the lack of current star formation in dSph galaxies as a consequence of reionization effects.

However, identifying and interpreting signatures of reionization in the LG has been proven to be complicated, as also studied in this thesis work. Most LG dSphs have extended SFHs or large metallicity spreads that are incompatible with reionization's early truncation of star formation. Grebel & Gallagher (2004) pointed out that the observed SFHs of the LG dwarfs did not support this simple picture: reionization could have affected at some degree the evolution of small galaxies but it is not sufficiently strong to produce coherent pattern of star formation, because there are also other physical phenomena that intervene, such as SNe feedback, gas stripping, time dependence of gas infall, etc. (Somerville 2002).

Latter models have been revised, allowing for some more star formation following reionization, because gas can be preserved via self-shielding (Barkana & Loeb 1999; Tassis et al. 2003; Okamoto & Frenk 2009) or reaccreted at later times. In this way it is reduced the discrepancy between model predictions and the observations of LG dwarfs. (e.g. Ricotti & Gnedin 2005; Bovill & Ricotti 2009; Sawala et al. 2010) *True fossils* of reionization, as defined in Ricotti & Gnedin (2005), are currently viewed as galaxies that formed the bulk of their stars prior to having star formation suppressed or quenched by reionization. But the true identification of such class of object is complicated

by other factors, such as the environment in which these dwarfs are located. An example for all refers to ultra-faint dwarf galaxies that are almost all located within the virial radius of the MW. Such close proximity to a massive host may enable mechanisms other than reionization, such as tidal stripping, tidal stirring and ram pressure, to quench early star formation in low mass galaxies. Moreover, it has been observed that some fraction of the faintest dwarfs shows clear signs of tidal interaction (Kirby et al. 2013a), making it challenging to unambiguously identify them as fossils (Bovill & Ricotti 2011).

In particular, Sawala et al. (2010) through high-resolution hydrodynamical simulation found that a combination of feedback and the cosmic UV background results in the formation of galaxies with properties similar to the LG dwarf spheroidals, and that their effect is strongly moderated by the depth of the gravitational potential.

More recently, always by means of high-resolution hydrodynamical simulations, it has been found that the impact of reionization can be more subtle than originally prospected. According to Oñorbe et al. (2015), the UV background and star formation feedback, plays a fundamental role in regulating star formation in low-mass systems. UV background can suppress infall of fresh gas, but is not likely to boil away cold gas already present.

In this regard, it is interesting to report here the results of the cosmological hydrodynamical simulations of the LG performed by Benítez-Llambay et al. (2016), according to which, the presence of metallicity/age gradients in dwarf spheroidals can be explained as a consequence of subsequent mergers of low mass halos. The authors model the resulting dSph as the result of a merger between two distinct low mass systems, able to form some stars separately before reionization. Star formation is predicted to decline briefly because of their weak potential wells and due to the combined effects of reionization and feedback from the formed stars. However, all these phenomena do not remove gas completely. A tenuous halo of gas remains around each dwarfs, unable to cool and to form stars. This gas serves as fuel for the second episode of star formation, triggered by a subsequent merger between two of such systems. The merger pumps energy into the old/metal-poor stellar component of the galaxy, which expands to lower densities and is at late times seen to surround the younger, more metal-rich population, which largely forms in situ. This process leads to the outside-in formation of two spatially-segregated stellar systems with distinct kinematics and metallicities. Sculptor, as also presented in this thesis work, presents multiple components and different time scales of star formation, in particular a longer star formation event in the innermost region of the galaxy. This is shown also in the model results of Benítez-Llambay et al. (2016) in their Figure 1.8, where the younger and more metal-rich population

appear centrally concentrated. This merger mechanism is able to reproduce also less produce gradients, such as the one by Sextans. From our study of Sextans we have not detected any metallicity gradient, because this galaxy has one of the largest core radius ($\sim$ 28 arcim). But from the results on the SFH we have constrained the duration of the main star formation event to 0.6 Gyr, thus indicating undoubtly a fast evolution of the system. Other works in literature, have shown, by inspecting larger samples, that effectively there are multiple stellar components also in Sextans and that the galaxy is surrounded by a very metal poor stellar halo (Battaglia et al. 2011).

A systematic study of isolated dwarfs has been conducted in the context of the LCID project by obtaining color-magnitude diagrams (CMDs) reaching the oldest main-sequence turnoffs for a sample of isolated dwarf galaxies (e.g. Cole et al. 2007; Bernard et al. 2008; Monelli et al. 2010a ; Hidalgo et al. 2011; Hidalgo et al. 2013), using the ACS camera on board of the Hubble Space Telescope. For the first time this kind of data has been obtained for dwarf galaxies beyond the Milky Way satellite system. The evolution of isolated dwarf galaxies is free from environmental effects due to the strong interaction with the parent galaxy, and thus, offer the possibility to probe global phenomena such as the effects of reionization in the early star formation of dwarf galaxies or the ability of SNe feedback to remove gas in small halos.

1.4.2 SNe Feedback

Radiative and stellar feedback have long been recognized as essential ingredients in galaxy formation, and they are thought to play an important role in determining the properties of dwarf galaxies. However, the early formation in such low-mass objects may significantly affect the evolution of their baryon content because of supernova (SN) explosions, driving a significant fraction of the gas away from the gravitational potential of the host. Stellar feedback was first discussed in the context of primordial globular cluster formation by Peebles & Dicke (1968). In the context of hierarchical structure formation, the possibility that SNe may remove a significant fraction of the gas present in dwarf galaxies was discussed by Dekel & Silk (1986) and Couchman & Rees (1986). Further, analytical treatment of such SN-driven winds was presented by Babul & Rees (1992) and Efstathiou (1992). Star formation and feedback have also been studied in the context of cosmological structure formation simulations. However, the efficiency of SN energy feedback in driving the gas out of the dark matter potentials was found to depend on the details of the feedback prescription: Katz (1992) found that the properties of their simulated galaxies were insensitive to the inclusion of star formation and feedback to the

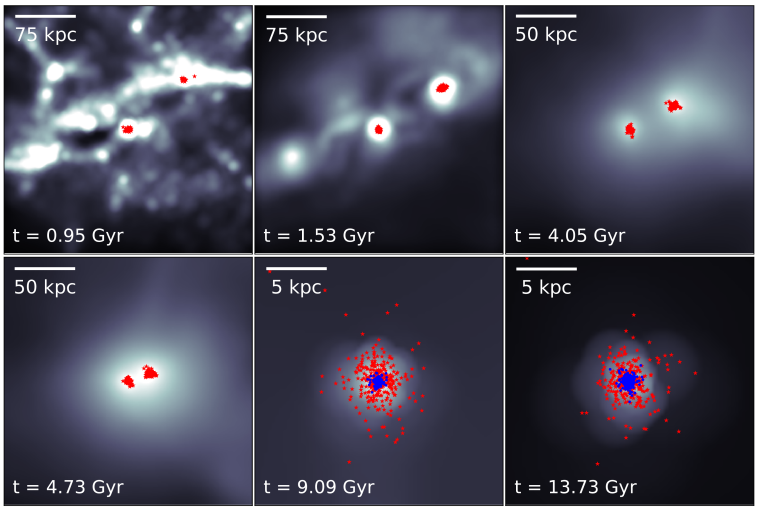

Figure 1.8: Several stages of the evolution of the a simulated dwarf from the study of Benítez-Llambay et al. (2016). Each panel is centred on the most massive progenitor and the grey scale is used to indicate local gas density. Red starred symbols are used to indicate the location of stellar particles that belong at $z = 0$ to the 'old' population (i.e., $t_{\rm form} \leq 2.5$ Gyr) and that have formed by the current time. Blue dots show the location of stars belonging to the 'young' stellar population.

simulations.

Navarro & Steinmetz (1997) found that the effect of SN feedback depends on whether the energy returned to the ISM is in the form of thermal or kinetic energy. In the former case, the energy is quickly radiated away and the effect of feedback is minimal, while in the latter case feedback is efficient in driving gas away from the dark matter potentials and suppressing star formation. Moreover, Mac Low & Ferrara (1999) found that the effect of feedback depends on the total mass of the system under consideration, with the low-mass systems being affected much more than the higher mass systems.

Energy feedback from SNe is also believed to have a significant effect on the metallicities of dwarf galaxies. The idea of metals being driven away from galaxies is supported by observations of the chemical enrichment of the intergalactic medium , as well as observations of dwarf galaxies in the Local Group. The ability of SN-driven winds to remove metals from galaxies has been studied extensively by Mac Low & Ferrara (1999). Prada & Burkert (2002) have summarized a correlation between mass-to-light ratio and metallicity of dwarf spheroidals, which they attribute to metal loss being more efficient for objects with shallower potential wells. They modeled the effects of repeated SN explosions from starbursts in dwarf galaxies with hydrodynamic simulations performed in a predetermined dark matter gravitational potential and with an initial baryon-to-gas mass ratio extrapolated from observations of higher mass systems. Their results suggest that galactic winds are very efficient in removing metals from dwarf galaxies, with the effect being more pronounced for the least massive objects.

1.5 Thesis Work

In this thesis are presented the SFHs and their analysis of two dSphs galaxies: Sextans and Sculptor. The methodology followed is the same in both cases and it has led to remarkable scientific results that have been published on refereed scientific journals. Both studies start from the ground-based photometry of these galaxies; in particular I firstly performed the data reduction of raw images with the objective to obtain deep stacked images of a good portion of the object under study, compatibly with a mean good seeing quality. It has been performed Point-Spread Function (PSF) photometry, thus obtaining two catalogues: for Sextans in the Johnson photometric system (B, V and I magnitudes), while for Sculptor in the DECam photometric system (g and r magnitudes). Thanks to the deep CMDs that reach the oldest MS TO, in both cases, it has been possible to analyze the star formation till the remotest epochs and trough targeted calculations to give estimates on how physical phenomena,

such as SNe feedback, could have influenced the final fate of these dSphs.

In Chapter 2 is presented the study devoloped for the dSph galaxy Sextans. Starting from deep stacked images taken with the 8 m Subaru telescope, it has been possible to derive a deep CMD reaching the oldest MS turn-off. Finally, it has been derived the complete SFH and constrained the first and unique event of star formation. The results have been published in the scientific journal Monthly Notices of the Royal Astronomical Society (MNRAS) (Bettinelli et al. 2018). In Chapter 3 the same approach has been applied to the dSph galaxy Sculptor. In this case the photometry has been taken with the 4 m Blanco telescope, but due to the 'proximity' of this object ($\sim$ 86 Kpc, which is the same for Sextans), it has been possible to reach the oldest MS turn-off and to derive the complete SFH. Also for this galaxy it has been measured a unique event of star formation, more diluted in respect to Sextans, but most importantly, its duration varies radially. This research work has been recently submitted to MNRAS.

An additional research that has been pursued during this thesis is the discovery and subsequent confirmation of an extended optical Einstein ring. Of course, this field of investigation is quite far from the main theme of the present work. But it has been decided to devote some time of investigation to this discovery because the object has been found on the deep images of Sculptor. In this sense, these optical images have revealed a great potentiality in different kind of studies. In Chapter 4 is reported the discovery of the so called Canarias Einstein ring. The nature of this Einstein ring has been confirmed thanks to spectroscopic observations at the Gran Telescopio Canarias (GTC), a 10 m class telescope. This discovery has been published in the scientific journal MNRAS as a letter (Bettinelli et al. 2016). Finally, in Chapter 7 a summary and conclusions are presented.

2

The Star Formation History of the Sextans Dwarf Spheroidal Galaxy: a True Fossil of the pre-Reionization Era

2.1 Abstract

We present the star formation history (SFH) of the Sextans dwarf spheroidal galaxy based on deep archive B,I photometry taken with Suprime-Cam at Subaru telescope focusing our analysis on the inner region of the galaxy, fully located within the core radius. Within the errors of our SFH we have not detected any metallicity gradient along the considered radial distance interval. As a main result of this work we can state that the Sextans dwarf spheroidal stopped forming stars less than ~ 1.3 Gyr after Big Bang in correspondance to the end of the reionization epoch. We have been able to constrain the duration of the main burst of star formation to ~ 0.6 Gyr. From the calculation of the mechanical luminosity released from supernovae (SNe) during the brief episode of star formation, there are strong indications that SNe could have played an important role in the fate of Sextans, by removing almost completely the gas component, so preventing a prolonged star formation.

2.2 Introduction

The Sextans dwarf spheroidal was discovered relatively recently by Irwin et al. (1990) during a quasars survey. It has not been possible to detect it simply by visual inspection, as it was done for the other seven classic Sculptor-like dwarfs, due to its very low central surface brightness, estimated to be 18.2 ± 0.5 mag/arcmin^2 (Irwin & Hatzidimitriou 1995). Since its discovery many photometric surveys have been performed in order to investigate the stellar populations properties of the system. In the first data available of Irwin et al. (1990) a red horizontal branch and a well defined asymptotic giant branch were already clearly present. Mateo et al. (1991) data showed the MS turn-off, a defined red giant branch and the presence of blue stragglers (BS). In the the analysis performed by Bellazzini et al. (2001) (see also Pancino et al. (2002)) the authors discovered the bimodal distribution in color of the red giant branch (RGB) stars and a double RGB-bump, unequivocally sign of two distict stellar components, a main one with $[Fe/H] \sim -1.8$ and a minor one with $[Fe/H] \sim -2.5$. Lee et al. (2003) presented deep wide-field BVI photometry obtained at the 3.6 m Canada-France-Hawaii Telescope (CFHT); later, Lee et al. (2009) derived the star formation history (SFH) making use of VI photometry. Interestingly they found, as Pancino et al. (2002), that in the central regions the metallicity increases up to $[Fe/H] \sim -1.6$, while in the more external part of the investigated field metallicity decreases down to $[Fe/H] \sim -1.8$. The spectroscopic determinations presented in literature are systematically more metal poor: Kirby et al. (2011a) measured a median $[Fe/H] = -2.00$. Lee et al. (2003) measured a similar value making use of the $(V - I)$ colour relation defined in Lee (1993), finding a mean metallicity of the RGB of $[Fe/H] \sim -2.1 \pm 0.1$, which would agree with the correlation between $[Fe/H]$ vs. M_V followed by other dwarf galaxies (e.g. Grebel et al. (2003), McConnachie (2012)).

From the structural point of view, Roderick et al. (2016) published an extensive photometric study up to 83 arcmin from Sextans' centre. The authors do not find any trace of tidal disruption but have been able to detect some overdensities equally distributed around the centre. Okamoto et al. (2017) detected the existence of an age gradient with younger stars more centrally concetrated than older ones, thus suggesting that it is unlikely that the inner region of Sextans could have been perturbed by strong tidal disruption.

The most relevant physical parameters of Sextans are summarized in Table 3.1.

In this paper we present the analysis of the SFH of the Sextans dwarf spheroidal based on deep wide-field, ground-based photometry. This study is organized as follows: in § 2.3, the observations, data reduction, the derivation

Table 2.1: Sextans parameters

Quantity	Value	References[a]
RA, α (J2000.0)	$10^{\rm h}13^{\rm m}03^{\rm s}.0$	(1)
Dec, δ (J2000.0)	-1° 36′ 52.0″	(1)
Galactic longitude, l (°)	243.5	(1)
Galactic latitude, b (°)	42.3	(1)
Galactocentric distance (kpc)	86±5	(2)
Heliocentric velocity (km s^{-1})	224.4±1.6	(3)
Ellipticity, e	0.29 ± 0.03	(4)
Position angle (°)	56.7±2.8	(4)
Core radius (′)	26.8±1.2	(4)
Tidal radius (′)	83.2±7.1	(4)
Luminosity, L_V ($L_\odot$)	$(4.1 \pm 1.9)\times10^5$	(5)
Absolute magnitude, M_V	-9.2 ± 0.5	(5)
Total mass, ($M_\odot$)	$(4.0\pm0.6)\times10^7$	(6)
Mass to light ratio, $M_\odot/L_\odot$	91 ± 49	(6)

[a](1) Irwin et al. (1990); (2) Mateo (1998); (3) Hargreaves et al. (1994); (4) Roderick et al. (2016); (5) Irwin & Hatzidimitriou (1995); (6) Łokas (2009).

of the photometry and the photometric calibration are presented. In § 2.4 the colour-magnitude diagram (CMD) of Sextans is presented. In § 2.5 presents the procedure of the SFH derivation; in § 2.6 it is confined the first event of star formation. In § 2.6.1 we performed a radial study of the SFH. In § 2.7 presents a discussion about the achieved results. Finally, in § 2.8 there are the summary and conclusions.

2.3 Observations and Data Reduction

The deep wide-field photometry we present in this work is a stack of many archive observations in B and I filters, (see Table 3.2 for details), covering approximately an area of 34×27 arcmin centered on the galaxy, taken with the Subaru Prime Focus Camera, Suprime-Cam (Miyazaki et al. 2002) in years 2003 and 2005. We have selected the data making use of the Subaru-Mitaka-Okayama-Kiso Archive System (SMOKA) (Baba et al. 2002). Reduction, that means overscan, bias substraction, flat fielding, distortion and atmospheric dispersion corrections (see Miyazaki et al. (2002)) and sky substraction, was performed using the SDFRED1 software (Yagi et al. 2002; Ouchi et al. 2004). The total exposure time is 2800 s in B filter and 8936 s in I filter. The pixel

Table 2.2: Observations

Filter	UT	PI	Exposure(s)	FWHM (")
B	2005/05/04	Kleyna J.T.	500×5	$0.6''$
B	2005/05/04	Kleyna J.T.	60×5	$0.7''$
I	2005/02/07	Arimoto N.	270×7	$1.0''$
I	2003/04/01	Yasuda N.	30×5	$1.0''$
I	2003/04/03	Ikuta C.	240×5	$0.6''$
I	2005/05/04	Kleyna J.T.	200×15	$0.6''$
I	2005/05/04	Kleyna J.T.	60×5	$0.6''$
I	2005/12/31	Arimoto N.	235×10	$0.9''$
I	2005/12/31	Arimoto N.	30×3	$0.9''$

scale is equal to $0.2''/px$.

The photometry on stacked images was performed making use of the DAOPHOT/ALLSTAR suite of programs (Stetson et al. 1990). We used a Moffatian of parameter $\beta = 1.5$ and radius of $R_{PSF} = 15$ pixels as point-spread function (PSF). From the output of ALLSTAR, only objects with $\sigma \leqslant 0.2$ and $-0.5 \leqslant$SHARP$\leqslant 0.5$, were taken into consideration, in order to clean up bad measured stars and galaxies. Once obtained the two catalogues in B and I filters, we performed the match using the package DAOMASTER (Stetson 1993). From this match, the final total catalogue in B and I filters counts ~ 86000 stars. The data have been calibrated making use of Stetson photometric standard field for Sextans (Stetson 2000; Stetson 2005), centered on the galaxy, with an extension of 36.1×36.0 arcmin. We calibrated the entire photometric catalogue derived from the stacked images, applying the following system of two equations:

$$\begin{aligned} B - b &= c_b \times (B - I) + z_b \\ I - i &= c_i \times (B - I) + z_i \end{aligned} \tag{2.1}$$

where B, I are the standard magnitudes, b, i the instrumental magnitudes ,c_b, c_i the colour therms and z_b, z_i, the photometric zero points. All the coefficients relative to the two derived photometric transformations, with the corresponding errors, are listed in Table 3.3.

2.4 The Colour-Magnitude Diagram

The CMD derived from our photometry is extended well below the oldest MS turn-off, for about 3 magnitudes. This means that we are able to extract in-

Table 2.3: Parameters used for calibrating the photometry with the associated errors

Parameter	Values
z_b	27.023 ± 0.005
c_b	0.064 ± 0.002
z_i	26.865 ± 0.014
c_i	0.056 ± 0.007

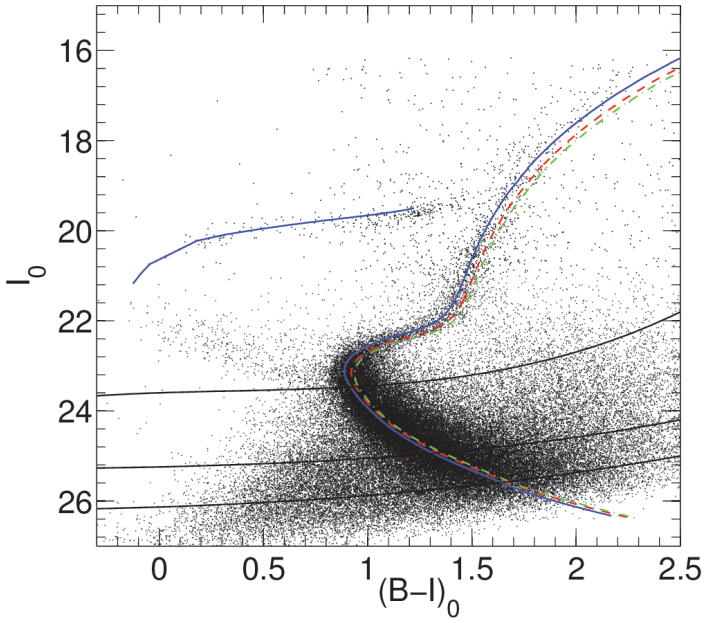

Figure 2.1: Observed CMD of Sextans dSph. Three isochrones from the BaSTI stellar evolutionary library have been superimposed on the CMD: $Z = 0.0003$, 13.5 Gyr (solid blue line in the electronic version), $Z = 0.0006$, 13.5 Gyr (dash-dotted green line in the electronic version), $Z = 0.0005$, 13.5 Gyr (dashed red line in the electronic version). Red dashed line corresponds to the mean recovered metallicity for the system $[Fe/H] = -1.6$. The core helium-burning locus is given only for the $Z = 0.0003$, 13.5 Gyr isochrone (solid blue line in the electronic version). Completeness levels are over plotted as black lines: in order of increasing I_0 magnitude these are 90%, 75% and 50%

formation till the very early epochs of Sextans and to constrain its first star formation episode. Fig. 3.3 shows the obtained CMD, corrected by reddening ($A_B = 0.171$, $A_I = 0.071$ (Schlegel et al. 1998; Schlafly & Finkbeiner 2011)), where we over plotted three isochrones from the BaSTI stellar evolution library (Pietrinferni et al. 2004) using a distance modulus of $(m-M)_0 = 19.67$ (Mateo et al. 1995). The blue and green isochrones, which correspond respectively to a metallicity of $[Fe/H] = -1.8$, $[Fe/H] = -1.5$ and an age of 13.5 Gyr, fit well the MS, the subgiant branch (SGB) and the red-giant branch (RGB). Nevertheless, from the broadening of the RGB locus (Harbeck et al. 2001) there is some hint that there could exist a metallicity spread between $[Fe/H] = -1.8$ and -1.5. Although, one should note that this color broadening of the RGB could be also compatible with an age spread at fixed metallicity as suggested by Okamoto et al. (2017). It is also present in the derived CMD a clear and extended blue and red horizontal branch (HB) and a quite populous region occupied by genuine blue stragglers (Okamoto et al. 2017), that means primordial binary stars that evolved in mass-transfer BS (Momany et al. 2007). The field contamination level in the central region is quite low and it has been estimated to be $\sim 2\%$ by Okamoto et al. (2017), so it does not significantly affect our results. Errors and completeness of the photometry are discussed in § **??**.

2.5 Derivation of the SFH

For solving the SFH of Sextans we have followed the prescription outlined in Hidalgo et al. (2009) and Hidalgo et al. (2011). This method allows to derive the star formation rate as a function of time and the age-metallicity relation. The three main codes used are: (1) IAC-Star (Aparicio & Gallart 2004), that computes synthetic CMDs (sCMDs); (2) IAC-pop (Aparicio & Hidalgo 2009), the core algorithm for the calculation of the SFH solutions; (3) MinnIAC (Hidalgo et al. 2011), a suite of routines that manages the process of sampling the parameter space, creating input data and averaging solutions. We define the SFH as a distribution function $\psi(t, z)dtdz$ which is the usual SFR but with the dependence both on time and metallicity.

2.5.1 The Case of Sextans

Firstly, making use of the code IAC-star (Aparicio & Gallart 2004) and the BaSTI (Pietrinferni et al. 2004) stellar evolutionary library, we computed a sCMD to be used for the analysis of the Sextans stellar properties, with 5×10^6 stars, characterized by a constant star formation rate (SFR) between 0 and 13.5 Gyr and an uniform distribution of metallicity of $0.0001 \leqslant Z \leqslant 0.002$ for all ages.

This metallicity range has been fixed acordingly to the metallicity distribution function (MDF) by Kirby et al. (2011b). As bolometric corrections we adopted Castelli & Kurucz (2004). We used as initial mass function (IMF) the one by Kroupa (2002). For the binary star distribution $\beta(f, q_{min})$ we adopted a fraction of binary stars of $f = 0.3$ and a flat distribution of the secondary to primary stellar mass ratio, q, with minimum $q_{min} = 0.5$.

As explained in deep details in (Aparicio & Gallart 1995), the simulation of observational effects is a key step for the interpretation of real data. In particular, to obtain a realistic model CMD to be compared with the real one, we need to simulate the observational effects that affect the real data. In order to estimate the completeness and uncertainties of our photometry we followed the standard technique of injecting a list of artificial stars in each stacked image and then re-deriving the photometry in the same way as done for real stars (see Hidalgo et al. (2011)). We injected 5×10^6 stars in each image along an uniform grid, with a separation of at least $2 \times R_{PSF} + 1$ pixels between the centroids of the artificial stars. The stars have been chosen in order to cover the full range of luminosity and colour of the oCMD, $0 \leqslant (B - I) \leqslant 2.5$ and a magnitude range of $16 \leqslant I \leqslant 26$; in particular we populated more the MS region $21.5 \leqslant I \leqslant 26$, with 3.5×10^6 stars, since it is the more relevant region for the derivation of the SFH, then the red-giant-branch (RGB) region $18 \leqslant I \leqslant 21.5$, with 1×10^6 stars, and finally, the upper part of the colour-magnitude diagram in the magnitude range of $16 \leqslant I \leqslant 18$, with 0.5×10^6 stars. In Fig. 3.3, we have over-plotted on the CMD of Sextans the completeness levels at 50%, 75% and 90%. The completeness has been calculated as the ratio of the number of artificial stars recovered to the number of all injected stars in each colour and magnitude interval. For each artificial star we have recorded the injected magnitude m_{inj}, the recovered magnitude m_{rec} and the position on the frame. We use the difference between the injected and recovered magnitudes $(m_{inj} - m_{rec})$ and the position of the synthetic star in the image to simulate the observational effects on the observed CMD. See Hidalgo et al. (2011) for a full description of the procedure.

In Fig. 2.2 we show as black dots the recovered stars with observational effects simulation and overplotted on them as red dots the observed stars. After the observational effects simulation, the distribution of stars in the oCMD is compared with the distribution of stars of each simple stellar population (SSPs) in the sCMD. The SSPs are selected by defining age and metallicity bins for the synthetic stars. For the age we have chosen intervals of 2 Gyr for the first 8 Gyr and a finer one, of 0.5 Gyr, for the last interval between 8 Gyr and 13.5 Gyr, since it is necessary higher resolution for well characterize the first event of SFH. The metallicity bins used are: $(0.01,\ 0.1,\ 0.3,\ 0.5,\ 1,\ 2) \times 10^{-3}$. The

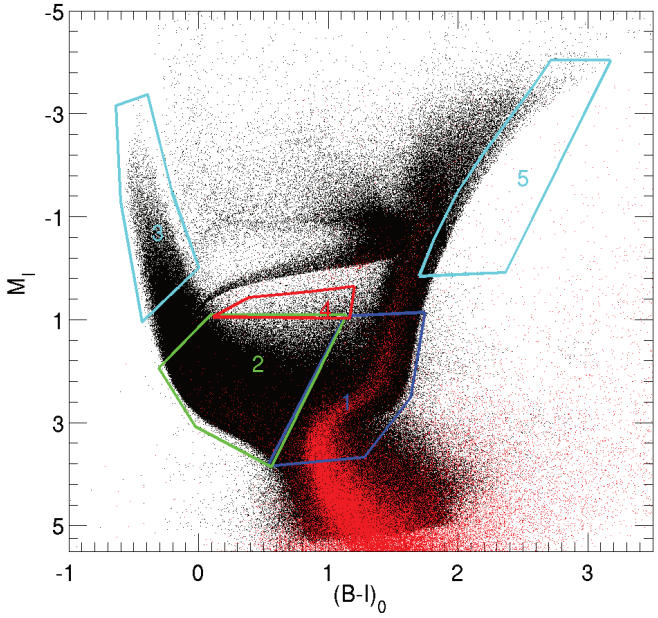

Figure 2.2: Synthetic CMD with the simulated observational effects (black) with overplotted the observed CMD (red). *Bundles* are the regions numbered from 1 to 5, see text for details.

higher the metallicities, the wider the intervals. Both CMDs are sampled by using *bundles*, macroregions which sample main features of the CMDs. Each of these bundles has a weight on the solution, given by the number of boxes defined in them. The larger the number of boxes, the larger the weight in the SFH.

We have defined five bundles, subdivided in boxes with varying size according to the region sampled, (see Table 3.4 and Fig. 2.2). In bundle 1 a finer grid has been used than in the other bundles, for a total of circa 700 boxes, since it is the region of the CMD of higher interest for the derivation of the SFH. This bundle, in fact, is the more important one for the SFH derivation because it samples the region of the CMD that is more affected by the age diffences, in

the sense that it corresponds to the more reliable 'clock' provided by the CMD of any stellar populations, that is the MS turn-off. Moreover, for the region of the MS stellar evolution models are accurate and well established. Bundle 2 samples the young MS, even though in the case of Sextans these stars are recognized to be genuine blue-stragglers stars (Okamoto et al. 2017). The grid has a larger binning since the density of stars is lower; in this case the boxes are about 150. Bundle 3 refers to the region of the MS occupied by the youngest stars, the so called blue plume; in our observed CMD there are no stars in this region, but we sample it in order to constrain the resulting SFH; the boxes in this case are 20. Bundle 4 contains a portion of SGB stars (about 70 boxes) and finally, bundle 5 is an almost empty bundle with the largest box size; it constrains the maximum allowed metallicity.

In order to minimize the dependence of the solution on the CMDs sampling parameters, we obtained 24 solutions varying the CMD binning within each bundle and the SSPs sampling. To do so, we have shifted by a 30% the age and metallicity in a total of 12 combinations of SSPs, each one sampled with two slightly different combinations of boxes distribution in the bundles.

To limit the effects on the solution due to uncertainties related to the distance modulus, photometric calibration and reddening we have shifted the oCMD 25 times along a regular grid with nodes in colour
$\Delta(B-I) = [-0.1, -0.05,\ 0,\ 0.05,\ 0.1]$ and magnitude
$\Delta I = [-0.2, -0.1,\ 0,\ 0.1,\ 0.2]$.
For each node we have calculated the 24 solutions described above, obtaining a total of 600 solutions. For each node a mean solution $\overline{\psi}$ and its $\overline{\chi^2_\nu}$ is calculated. In this way we have obtained 25 different $\overline{\chi^2_\nu}$, the one with the minimum value indicates the best solution. The best solution we have found is the one with a shift of +0.1 mag in I filter and no shift in colour. So that we are able to minimize the effects of the aforementioned external parameters. In Fig. 2.3 are plotted the obtained results. In the upper panel it is shown the star formation rate as a function of time, $\psi(t)$, in the middle panel the age-metallicity relation $Z(t)$ and in the lower panel the cumulative mass function. The resolution of our results shows that Sextans has experienced a single event of star formation limited to the first ~ 2 Gyrs after Big Bang. For clarity we have tabulated the percentage of stellar mass produced in Table 5.1; it is evident that Sextans has finalized the bulk of its star formation before ~ 11.9 Gyr ago with the peak reached at ~ 13 Gyr ago. In Fig. 2.4 the Hess diagrams of the oCMD (left panel), the best solution CMD (middle panel) and the residuals (right panel) are plotted. Note here, that we have excluded foreground contamination points in the right part of the CMD. From the residuals Hess diagram, with the values expressed in units of Poisson error, the good agreement between the observed

Table 2.4: Box sizes in each bundle that sample the observed CMD

Bundle #	Δcol	Δmag
1	0.025	0.125
2	0.1	0.205
3	0.1	0.23
4	0.1	0.23
5	1.5	0.67

Table 2.5: Mass percentiles formed in Sextans as a function of redshift and look-back time.

Mass %	$Look-back\,Time(Gyr)$	$Redshift$
10	13.26	10.1
20	13.11	8.3
30	12.95	7
40	12.80	6.1
50	12.64	5.4
60	12.43	4.7
70	12.22	4.15
80	11.92	3.55
90	11.45	2.9

and simulated CMD in almost all the evolutionary phases is noticeable. We note that the numerical code used for computing the synthetic CMD does not account for a dispersion of stellar masses along the core He-burning sequence as due to the occurrence of stochastic mass loss efficiency in the previous RGB stage. This prevents the possibility to properly reproduce the color distribution of stars along the HB in the observed CMD. Nevertheless, we wish to note that this evolutionary sequence is not accounted for in the analysis of the SFH and, hence this limitation has no impact at all on the results presented in this paper. It is interesting to note that objects at faint magnitudes to the blue side of the MS in the observed CMD are largely absent in 'best solution' CMD; these are probably unresolved faint galaxies.

2.6 Confining the First Event of Star Formation

Uncertainties deriving from observational data and from the SFH computational procedure affect the shape of the final SFH, in the sense that there is a loss of age resolution (Aparicio & Hidalgo 2009, Hidalgo et al. 2011, Aparicio et al. 2016). This effect translates into an amplification of the duration of the

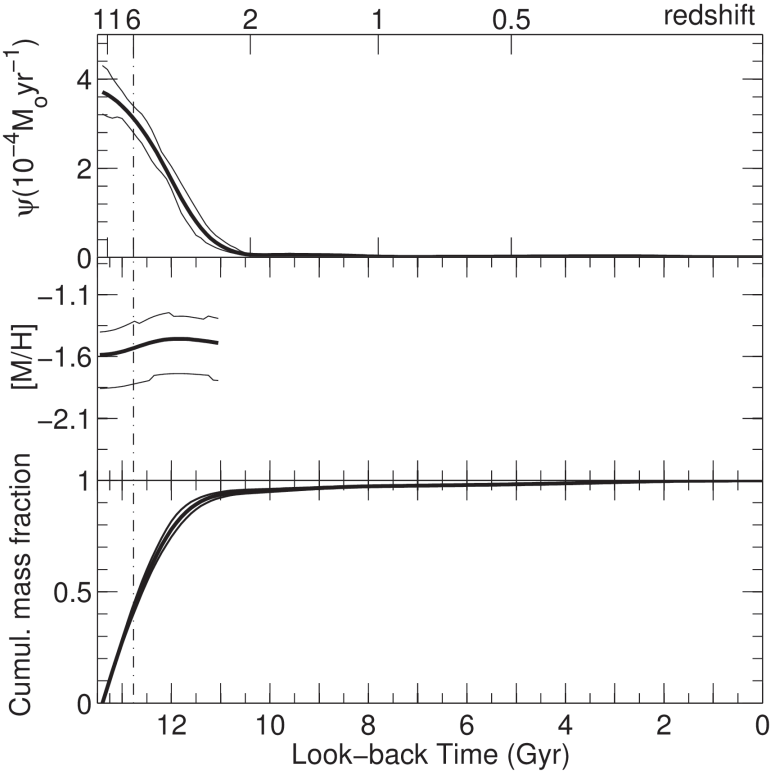

Figure 2.3: Results of the Sextans SFH. Top panel: SFH as a function of time ($\psi(t)$). Middle panel: metallicity of the system as a function of the time. Lower panel: cumulative mass fraction as a function of the time. Uncertainties have been drawn as this lines.

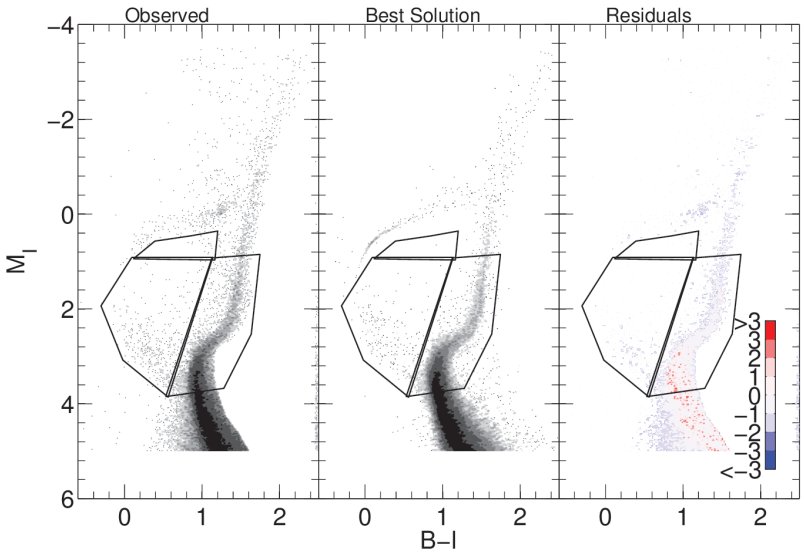

Figure 2.4: Hess diagrams relative to the observed CMD (left panel), best solution CMD (middle panel) and residuals CMD (right panel). The residuals are in units of Poisson uncertainties. Residuals from $\sigma = 0$ to $\sigma = 3$ refer to the case in which the model predicts more stars in respect to the oCMD. Residuals from $\sigma = 0$ to $\sigma = -3$ refer to the case in which the model predicts less stars in respect to the oCMD. Gray levels show the density of stars. A factor of 2 in density exists between each two successive gray levels. The single dots are shown where the density is less than 2 stars per $(0.02)^2$ mag. The boxes show the areas of the CMD used for the derivation of the SFH.

main event of SFH. In order to confine the duration of the first stellar burst in Sextans we have calculated the SFH of a number of mock stellar populations with an increasing age width all starting 13.5 Gyr ago. The duration of each burst, in terms of Full Width at Half Maximum ($FWHM_{in}$), has been chosen to be: 0.25, 0.5, 0.75, 1, 1.5, 2 Gyr. Metallicity has been fixed to $[Fe/H] = -1.6$, which is the mean metallicity recovered for the total SFH of Sextans.

Observational effects on these mock bursts have been simulated using the completeness tests results described in § 2.5.1. Then, the SFH of each mock population has been derived with the same procedure used for real data (i.e. the same *bundles* and parameters). In order to quantify the uncertainties on the recovered $FWHM_{rec}$ we have repeated five times the simulation for each synthetic burst using different random number seeds in the IAC-star input parameters. The mean recovered $FWHM_{rec}$ of each mock burst are: 2.5, 2.6, 2.8, 2.9, 3.2, 3.3 Gyr. In Fig. 2.7 are plotted both input mock bursts and the recovered SFHs associated to them. Since we have simulated an input constant star formation rate in a fixed time interval, input mock bursts have a rectangular shape, while, due to simulated photometric errors, the recovered SFHs result smoothed and broadened over a larger time interval. Fitting a Gaussian profile to the Sextans observed $\psi(t)$ in the age range $9.5 - 13.5$ Gyr we estimate $\sigma = 1.2$ Gyr, which corresponds to a $FWHM_{obs} = 2.8$ Gyr.

In Fig. 2.8 we plotted the $FWHM_{in}$ of the mock bursts and their associated mean recovered $FWHM_{rec}$. Fitting the resulting data with a quadratic polynomial we are able to constrain the first star formation event to an hypothetical mock burst having a $FWHM_{in} = 0.64 \pm 0.03$ Gyr. The obtained result is consistent with the estimate of about 0.8 Gyr obtained by Kirby et al. (2011a) via chemical evolution models, see Fig. 3.22.

Seen in this light, the star formation ended close to 12.9 Gyr ago, while the end of the epoch of the reionization is fixed at ~ 12.77 Gyr (Becker et al. 2001). This means that the star formation in Sextans was completed together to the end of the epoch of reionization. An analogous result has been derived recently by Revaz & Jablonka (2018) by means of high resolution chemo-dynamical simulations of dwarf galaxies in a ΛCDM cosmology. They classified the SFH of Sextans as *quenched*, in the sense that the potential well of this galaxy is so shallow that the gas heated by the UV photons escape the system, so the star formation is rapidly quenched after 2 or at maximum 3 Gyr.

2.6.1 Radial SFH

In passing we made the attempt to investigate the radial variation of the SFH. In order to do this we divided the area into 3 elliptical regions, with delimiting

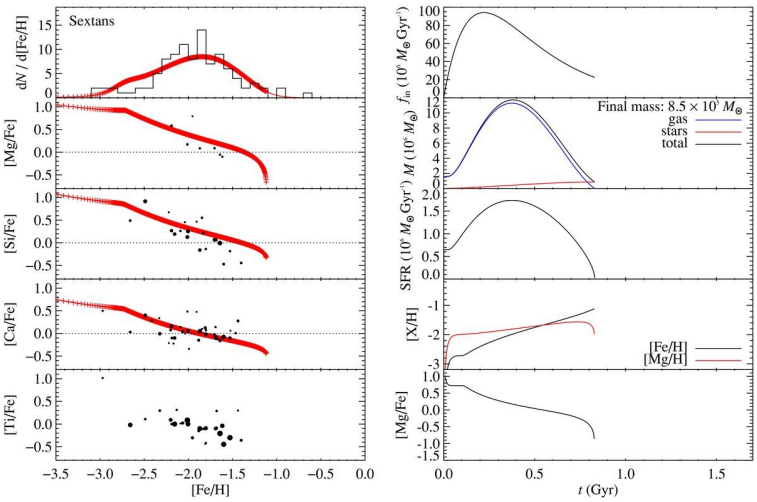

Figure 2.5: Left: the top panel shows the observed MDF as the black histogram and the modeled MDF in red. The model is convolved with an uncertainty function to mimic the broadening of the histogram induced by observational error. A cross marks each 1 Myr time step, but these are too closely spaced to discern for most of the metallicity range. Very few stars are expected to have formed at the low metallicities where the crosses are distinguishable. The other panels show the observed [Mg/Fe], [Si/Fe], [Ca/Fe], and [Ti/Fe] ratios as black points whose sizes are inversely proportional to measurement uncertainties. Only points with uncertainties less than 0.3 dex are shown. The red lines show the abundance ratios of the stars and gas at each time step. We do not show the model results for [Ti/Fe] because the SN yields are inaccurate. Right: the gas flow and SFH for the best-fit model. From top to bottom, the panels show the gas inflow rate; the stellar, gas-phase, and total baryonic mass; the SFR; the iron and magnesium abundances; and the [Mg/Fe] ratio, all as a function of time. The second panel also gives the final stellar mass in the model.

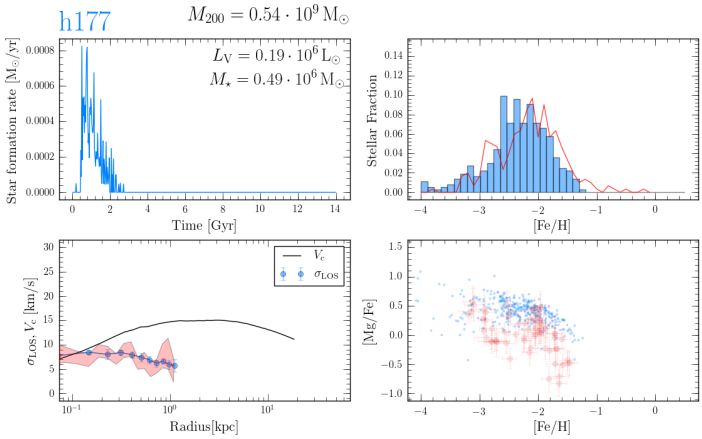

Figure 2.6: The model id, the model galaxy total mass (M_{200}), total luminosity (L_V), and total stellar mass ($M_\star$), which are calculated inside the virial radius R_{200} are indicated on the upper left hand side of each series of 4 panels. For each galaxy, the upper left panel displays the model star formation history. The lower left panel shows the line of sight velocity dispersion of the model galaxy in blue, as compared to the observations (red shaded area). The black line corresponds to the total circular velocity. The upper right panel displays the model galaxy metallicity distribution. The lower right panel gives the galaxy [Mg/Fe] vs [Fe/H] distribution. In both quadrants, the model is seen in blue and the observations in red.

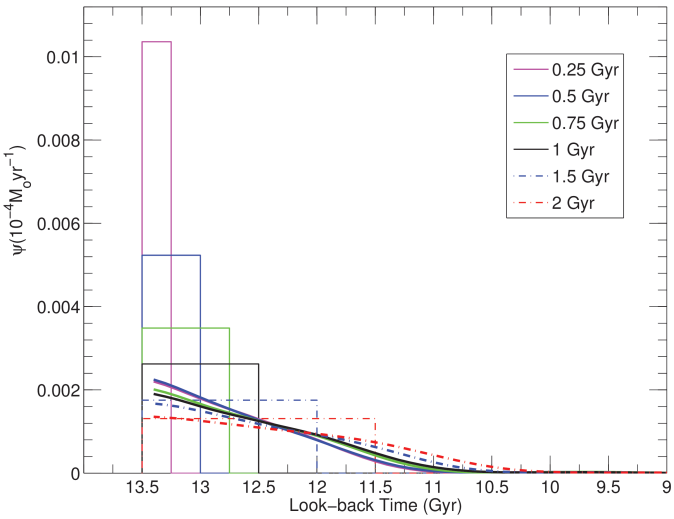

Figure 2.7: Recovering of an input simulated star formation burst. Input mock bursts with constant star formation rate and fixed time duration are shown (rectangular shape) with the recovered solution for each of them (smoothed curves).

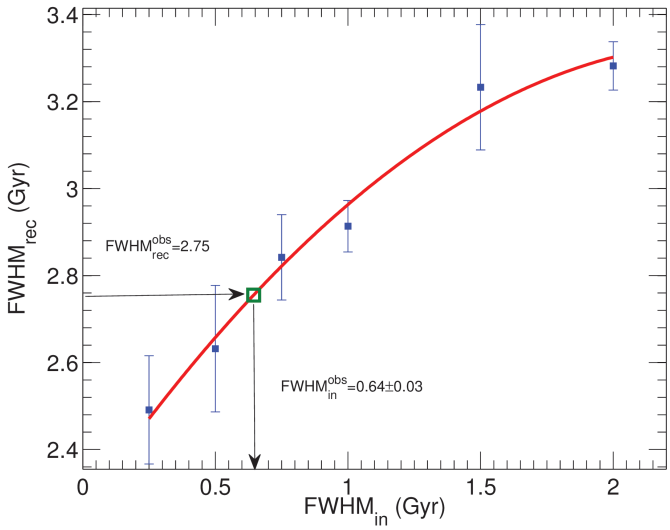

Figure 2.8: $FWHM_{in}$ is the Full Width at Half Maximum of the input mock bursts, $FWHM_{rec}$, the recuperated FWHM relative to the SFH of each mock bursts. Points have been fitted with a quadratic polynomial. Knowing the FWHM of the best SFH solution, making use of the intercept on the fitting red line (see green box) we have been able to confine the first star formation burst to a value of $FWHM_{in}^{obs} \sim 0.64$ Gyr

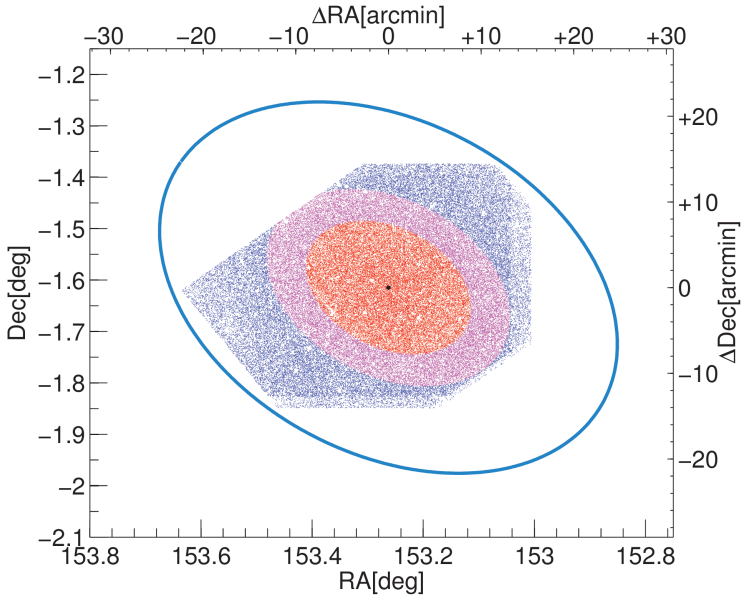

Figure 2.9: Stars spatial distribution, the ellipse major axis are in the intervals $a \leq 9.65$ arcmin for red points; $9.65 < a \leq 14.24$ arcmin for magenta points; and $14.24 < a \leq 25.86$ arcmin for blue points. The ellipse delimiting the core radius is plotted in light blue.

major axis of 9.65, 14.24 and 25.86 arcmin, see Fig. 2.9. The center assumed for the analysis is coincident with the one tabulated by Irwin et al. (1990) in J2000.0 coordinates (153.2623,-1.6146). The position angle adopted is $\theta = 56.7$ (Roderick et al. 2016). The major axes have been fixed in order to have ~ 29000 stars in each elliptical region for statistical consistency. For each region it has been derived the SFH using in each case the corresponding oCMD and as model CMD the one adopted for the total SFH. In Fig. 2.10 is shown the resulting metallicity as a function of time for all the 3 regions. Within errors it is not detectable any metallicity gradient. The same can be visualized from the comparison of the cumulative mass fractions, thus indicating the absence of a radial variation of SFH. (lower panel Fig. 2.10).

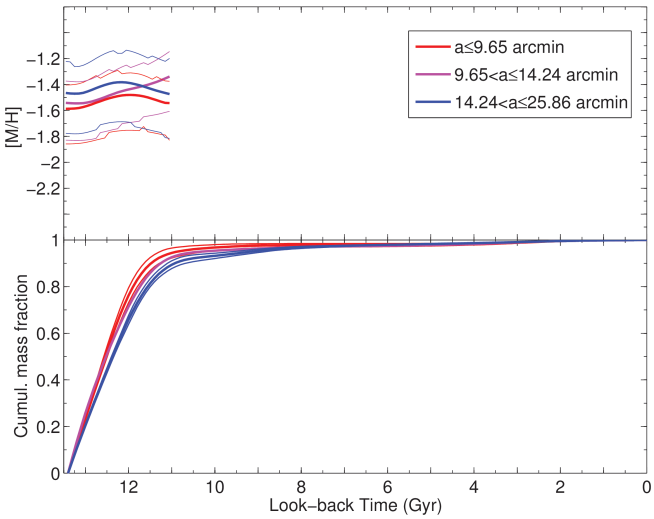

Figure 2.10: Upper panel: metallicity of the system as a function of the time for the three regions selected in Fig. 2.9. Lower panel: cumulative mass fraction as a function of the time. The same colour code as in Fig. 2.9 has been used. For clarity only the error bands relative to innermost and outermost regions have been shown.

2.7 Discussion

The resulting SFH is globally in agreement with the findings by Lee et al. (2009) who derived the SFH from the photometry presented in Lee et al. (2003). This is also confirmed by the mean metallicity we derived, equal to $[Fe/H] = -1.60 \pm 0.25$, which is in good agreement with the one estimated by Lee et al. (2009) in the central region of their field. Lee et al. (2009) measured that the metallicity of the stars is $[Fe/H] = -1.6$ in the central region, decreasing down to $[Fe/H] = -1.8$ in the outer region within the first Gyr. From our analysis, instead, emerges that metallicity in the inner core radius of Sextans does not present a radial gradient, as shown in Fig. 2.10, though our data span more or less the same radius of Lee et al. (2009). Moreover, the metallicity gradient measured between the innermost and the more external region in Lee et al. (2009) is of the order of ~ 0.2 dex, a value close to the error in determination of our metallicity. This difference in the detection of the gradient could be related to a poor statistics in the number of stars used by Lee et al. (2009) for the calculation of the SFH in each region, of the order of ~ 5000 stars, while we adopted ~ 30000 stars for each of our three regions. This could be also related to photometric data not deep enough, so that, the SFH is affected by large errors. In fact, in that work, the completeness for magnitude $I \sim 23.5$ is at $\sim 55\%$, while in the present work, the completness at these magnitudes is more than 95%. This strongly influence the result and the associated error. Another important aspect is that Lee et al. (2009) assumed that Sextans started forming stars 15 Gyr ago, while we constrained the age of the oldest acceptable population to 13.5 Gyr.

Our results on metallicity are supported by the fact that Sextans presents almost a flat $[Fe/H]$ radial distribution from the spectroscopic measurements conducted by Kirby et al. (2011b) over an area very similar to the one sampled in this work. The authors concluded that the lack of gradients, also seen in Canes Venatici I and Ursa Minor, indicates a star formation event significantly shorter than 1 Gyr. By means of chemical evolution models, they find also for Sextans, a duration of the star formation of just 0.8 Gyr, hence in striking agreement with what we found in our analysis.

But the metallicity distribution found by Kirby et al. (2011b) peaks at ~ -1.8, 0.2 dex lower than our mean metallicity determination. This difference is consistent with the metallicity bin we used in the derivation of the SFH, which is ~ 0.0002. As a further test, to see if the SFH is affected by this metallicity difference, we rederive it imposing an input model whose stars follow the MDF by Kirby et al. (2011b). In Fig. 2.11 are shown the original SFH, obtained without assuming any a priori MDF (in black) and the SFH derived imposing

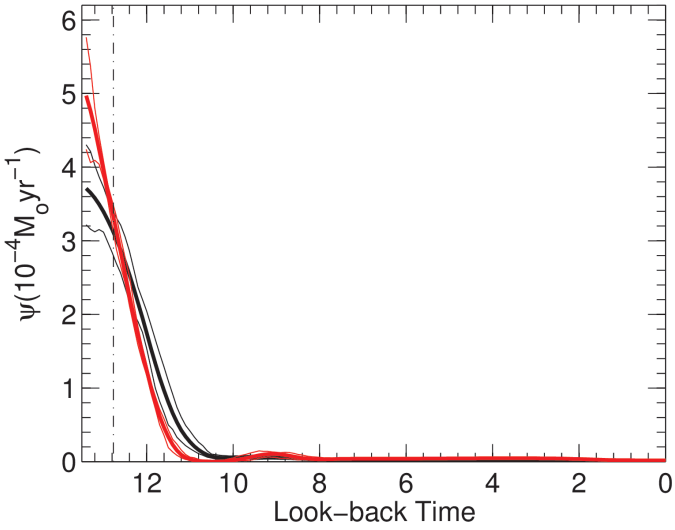

Figure 2.11: Original SFH, obtained without assuming any a priori MDF (in black) and the SFH derived imposing the MDF by Kirby et al. (2011b) (in red).

the MDF by Kirby et al. (2011b) (in red). In Fig. 2.12 the cumulative mass fraction as a function of the lookback time are also shown, color coded as in Fig. 2.11. The SFH in both cases is very similar in shape, demonstrating that assuming a MDF as in Kirby et al. (2011b) does not change the results of the present work. Moreover, assuming this MDF the star formation appears even steeper than the original one, thus confirming the trend already found without assuming any MDF for the input model. It is worth noting that even a mean metallicity of -1.6 for Sextans would be consistent with the trend in the metallicity-luminosity plane for galactic dSph (see Grebel et al. (2003) and McConnachie (2012)).

The question arising now is why, as detected with larger surveys, does Sextans present clear signs of the presence of a younger (and more metal rich) stellar population toward its center, that translates in an age and metallicity gradient. (see Harbeck et al. 2001, Bellazzini et al. 2001, Pancino et al. 2002, Lee et al. 2003, Rizzi et al. 2004, Okamoto et al. 2017)

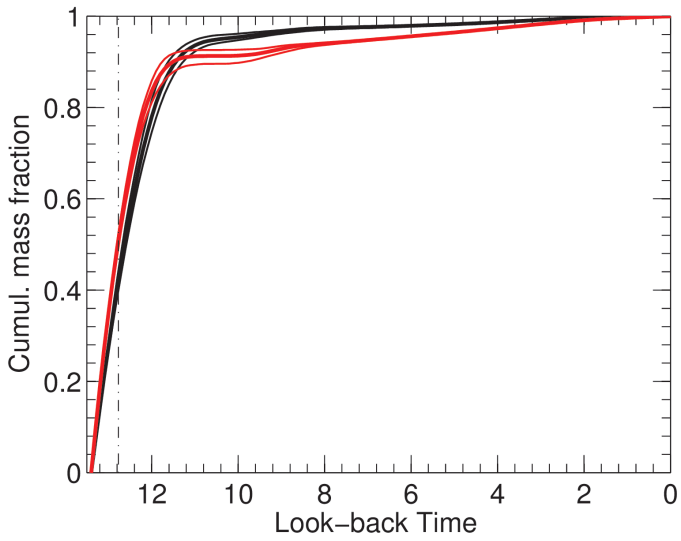

Figure 2.12: Cumulative mass fraction as a function of the lookback time, color coded as in Fig. 2.11.

Okamoto et al. (2017) through the analysis of the various evolutionary phases along a radius more extended than the tidal radius, have been able to detect an age gradient. Relatively younger stars (~ 10 Gyrs) are more centrally concentrated than old stars (~ 13 Gyrs). Through our detailed analysis, limited to the core radius, we have not detected any stellar populations gradient, so we conclude that the gradient found by Okamoto et al. (2017) has its origin after the core radius.

This point has been discussed also for the case of the isolated dSph Tucana (Monelli et al. 2010b), that resemble for some aspects the case of Sextans. Tucana SFH is characterized by a unique and pronounced event of star formation and a steep rising of metallicity in correspondance of the burst followed by almost no evolution. But hints of the presence of two generations of stars have been found in the complex morphology of the HB in Tucana (Monelli et al. 2010b). It is reasonable that the second generation formed towards the center, since newly processed gas would concentrate there.

This idea is supported by the evidences found in the MDF by Kirby et al. (2011b). This presents, in fact, a small bump at $[Fe/H] \sim -3$, so at extremely low metallicities. This bump is interpreted by the authors as the sign of a rapid burst happened at early times followed by an epoch of minimal star formation, maybe due to SNe type II strong ejecta.

Battaglia et al. (2011) found that within $0°.8$ from the center of Sextans, there is an high metalicity spread, with $-3.8 < [Fe/H] < -1.4$ and an average $[Fe/H] \sim -1.9$, so partially in agreement with our results, even though our mean metallicity is ~ 0.3 dex higher. In the outer region, ($R > 0°.8$), the metal poor population is predominant. Evidently, these stars underwent a very quick formation, while the stars in the inner part a more prolonged one.

This picture would suggest a first brief event of star formation which produced the diffuse large scale metal poor population and a more extended star formation that generated the centrally concentred metal rich population. From the study performed by Hidalgo et al. (2013) on the radial variation of SFH of dwarf galaxies emerges that Sextans matches the case of a typical dSph characterized by an extended old stellar population of ~ 13 Gyr at all galactocentric radii and a very small age gradient towards the center.

In the works by Ricotti & Gnedin (2005) and Bovill & Ricotti (2011) it is resumed a very stimulating aspect: the early and single star formation burst of Sextans could be an array of short bursts that we are not able to resolve with the actual techniques. The authors conclude that the metal spread and abundances, typical of dSph of the MW, are not necessarily produced by a prolonged and continous star formation of more than $2-4$ Gyrs (see e.g. Grebel & Gallagher (2004)); similar values can be obtained in the regime of bursty and

multiple events of star formation with timescales down to 50 Myrs (Matteucci & Recchi 2001). This is strictly connected to the iron enrichment by SNe Ia that is uncertain and dependant on the mode of star formation. Matteucci & Recchi (2001) estimated that this timescale varies from 40 to 50 Myr for an instantaneous starburst to 0.3 Gyr for a typical elliptical galaxy, thus far from our time resolution.

Sextans stopped early to form stars and it is of great interest to investigate if this phenomenon is linked in any way to the ultraviolet (UV) cosmic reionization, or if it is mainly due to local causes, such as intense galactic winds and SNe feedback (Hidalgo et al. 2011, Aparicio et al. 2016, Lanfranchi & Matteucci 2004).

When considering the results of the retrieved SFH as well as data in literature, the question arising is whether Sextans is 'true fossil' of the pre-reionization era in the sense introduced in Ricotti & Gnedin (2005): a dwarf that has experienced more than the 70% of its star formation before the end of the reionization and that has a luminosity $L_V < 10^6\,L_\odot$. Sextans satisfies the second condition, since it has a luminosity $L_V = (4.1 \pm 1.9) \times 10^5\,L_\odot$ (Irwin & Hatzidimitriou 1995). Regarding the first condition, the galaxy formed 70% of its stellar mass $\sim$ 12 Gyr ago as derived from the SFH, but, as discussed in § 2.6, we have been able to confine the initial event of star formation to $\sim$ 0.6 Gyr, so, the above mass fraction would be completed surely within the reionization epoch.

From these two facts Sextans can really be classified a *true fossil* of the pre-reionization era. Moreover, the work by Ricotti & Gnedin (2005) corroborates the hypothesis according to which internal feedback, such as photoheating by the stars inside the galaxy and SNe explosions, have been the principal causes of suppression of star formation, since true fossils are the result of feedback processes in action prior to reionization. So that, they are expected to evolve passively after the end of the reionization era because of the exaustion of gas; this is what the results of our analysis of Sextans are suggesting.

In order to investigate this hypothesis we have calculated, as outlined in Hidalgo et al. (2011), the mechanical luminosity of the SNe released during the main star formation episode. This quantity together with the value of the mass of gas of the galaxy can be compared with the results presented in Mac Low & Ferrara (1999) to discern the modality according to which Sextans had lost mass in the past. Using the results from the SFH, we have calculated that a total of $9.2 \times 10^5\,M_\odot$ of gas were converted into stars. We have derived this value by scaling the SFH obtained from our observations to the whole galaxy using the King profile as obtained in Roderick et al. (2016). We obtained a total of 1.6×10^4 SNe assuming a minimum progenitor mass for core collapse

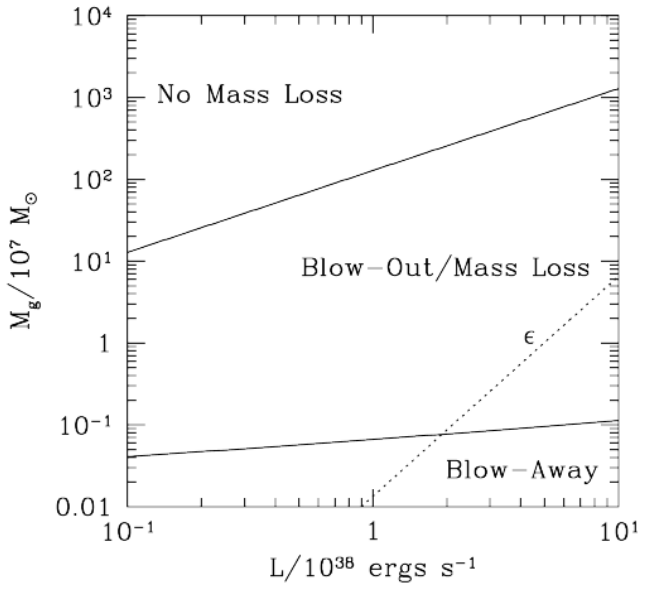

Figure 2.13: Regions of the gas mass (M_g) - mechanical luminosity of the starburst (L) plane in which blowout or blow-away can occur (Mac Low & Ferrara 1999).

SNe of $6.5\,M_\odot$ (Salaris & Cassisi 2005), and 8.7×10^3 SNe in the case of a progenitor of $10\,M_\odot$. Assuming an energy release per SN of 10^{51}erg (Leitherer et al. 1999) and a duration of the episode of 0.6 Gyr, we have calculated a total mechanical luminosity released during the old episode of $L_w = 8.2 \times 10^{38}$ erg/s and $L_w = 4.6 \times 10^{38}$ erg/s, respectively for 6.5 and $10\,M_\odot$. From the comparison of the above values with the model results of Mac Low & Ferrara (1999) shown in their Figure 1 (reported here in Fig. 2.13), it is clear that Sextans places in the region of blow-away regime in concomitance to the blow-out/mass loss regime. This result indicates that effectively SNe could have played an important role in the fate of Sextans by removing almost completely the gas component, so preventing a star formation extended over time (Dekel & Silk 1986,Kawata 2001, Chiosi & Carraro 2002). From our analysis we can not quantify how much reionization has influenced the SFH of Sextans dSph, even though it has persisted during all the early evolution of the galaxy. From the simulations of Sawala et al. (2010) it is not expected that Sextans could be able to form stars after the epoch of reionization due to its relatively low mass. Moreover, there are also external effects such as the ram pressure stripping (Gatto et al. 2013) that have to be taken into account. Concerning the fact that Sextans' SFH could have been influenced by tidal interactions, from structural studies such as the one by Roderick et al. (2016) there are no clear signs of an undergoing tidal disruption from the MW.

2.8 Summary and Conclusions

We derived the star formation history (SFH) of the Sextans dwarf spheroidal galaxy based on deep archive B,I photometry taken with Suprime-Cam at Subaru telescope. The data are limited to the core radius of the galaxy. We have not detected any metallicity gradient along the considered radial distance interval within the errors of our SFH. We have been able to constrain the duration of the main burst of star formation to ~ 0.6 Gyr, thus indicating that the Sextans dwarf spheroidal stopped forming stars ~ 12.9 Gyr ago before the end of the reionization epoch. From our analysis based on the model results by Mac Low & Ferrara (1999) and the calculation of the mechanical luminosity released from SNe during the brief episode of star formation, we can advance the hypothesis that Sextans run out most of its gas reservoirs before the end of the reionization due to gas outflows induced by SNe of type II, capable to throw out of the dwarf potential well the newly produced enriched elements and the remaining gas.

3

The Star Formation History of the Sculptor Dwarf Spheroidal Galaxy

3.1 Abstract

We present the star formation history (SFH) of the Sculptor dwarf spheroidal galaxy based on deep g,r photometry taken with DECam at the Blanco telescope, focusing our analysis on the central region of the galaxy extended up to ~ 3 core radii. We have investigated how the SFH changes radially, subdividing the sampled area into four regions, and have detected a clear trend of star formation. All the SFHs show a single episode of star formation, with the innermost region presenting a longer period of star formation of ~ 1.5 Gyr and for the outermost region the main period of star formation is confined to ~ 0.5 Gyr. We observe a gradient in the mean age which is found to increase going towards the outer regions. These results suggest that Sculptor continued forming stars after the reionization epoch in its central part, while in the peripheral region the majority of stars probably formed during the reionization epoch and soon after its end. From our analysis Sculptor can not be considered strictly as a fossil of the reionization epoch.

3.2 Introduction

The first dwarf spheroidal (dSph) galaxy to be discovered early in the last century by Shapley (1938) is Sculptor. Since then, many other dwarf galaxies satellites of the MW have been discovered. Historically, Sculptor, with For-

nax, Leo I, Leo II, Draco, Ursa Minor, Carina, Sextans, is considered as the prototypical dwarf spheroidal galaxy (McConnachie 2012); these galaxies are defined *early-type dwarf galaxies* (van den Bergh 1999;Tolstoy et al. 2009) thus systems with a total luminosity of $M_B > -14$, characterized by low optical surface brightness ($V \sim 22-26$ mag/arcsec^2), no nucleus and poor gas content (Gallagher & Wyse 1994). Despite these similarities, almost all dwarfs disclose their own peculiarities in the properties of their stellar populations such as in the SFH, chemical patterns, stellar variable populations and dark matter content.

Sculptor has been studied in depth since its discovery, photometrically, spectroscopically and in the radio wavelengths, in order to detect the presence of neutral hydrogen (HI). Sculptor was found to be embedded in two HI clouds symmetrically distributed respect to the optical center, see Figure 3.1 (Carignan et al. 1998;Bouchard et al. 2003;Piatek et al. 2006). This finding is very important since Sculptor is the only dwarf spheroidal galaxy known to have retained this gas. The major parameters relative to this system are listed in Table 3.1.

Even though, at a first sight, the morphology of its CMD appears quite simple, the analysis of its stellar populations and SFH is not trivial, as will be shown in the present analysis. The published CMDs do not show a strong intermediate-age population, while the large RGB spread suggests the presence of internal age or abundances variations (Da Costa 1984).

Monkiewicz et al. (1999) observed a small region of ~ 2 arcmin^2 located 14.1 arcmin from the center of Sculptor, using the Wide-Field Planetary Camera 2 (WFPC2) aboard the HST. The resulting CMD reaches 3 magnitudes below the oldest MS turn-off and it resembles the stellar population of the earliest globular clusters. In the same year, Hurley-Keller et al. (1999) published a wide field deep CMD based on data taken with Big Throughput Camera (BTC) at the CTIO 4 m telescope. The quality of this CMD, in terms of its combination of depth and area, is unprecedented.

By means of a study of the chemical, kinematic and spatial distribution of its stellar populations on a region extended 40 arcmin from the center of Sculptor, Tolstoy et al. (2004) discovered the presence of two distinct ancient stellar components (both ≥ 10 Gyr). These two stellar components are characterized by different metallicities (one metal-rich $-0.9 > [Fe/H] > -1,7$, one metal-poor $-1.7 > [Fe/H] > -2.8$), distributions (the metal-rich is more centrally concentrated, while the metal-poor is spatially extended) and velocity dispersions ($\sigma_{metal-rich} = 7 \pm 1$ km s^{-1} and $\sigma_{metal-poor} = 11 \pm 1$ km s^{-1}). Battaglia et al. (2008a) confirmed the above results (on a radial distance of ~ 1 degree centered on the galaxy), moreover they measured a velocity gradient of

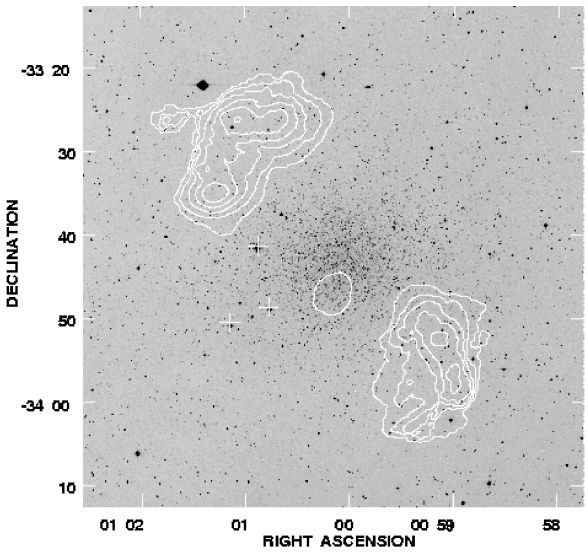

Figure 3.1: HI surface densities superposed on the STScI Digitized Sky Survey optical image. The contours are 0.2, 0.6, 1.0, 1.4, 1.8, and 2.2 $\times 10^{19} cm^2$ (Carignan et al. 1998).

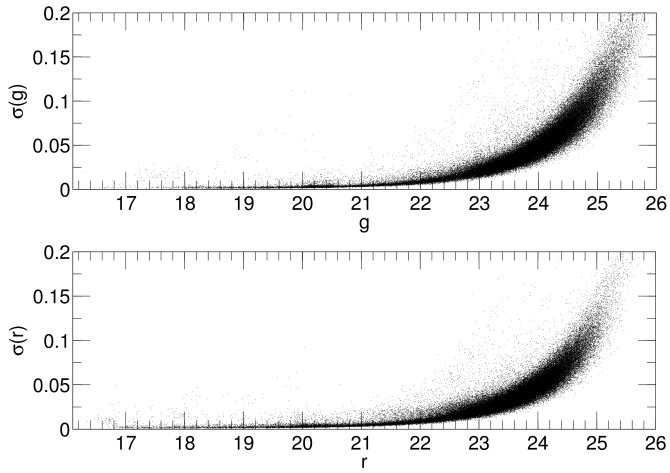

Figure 3.2: Calibrated magnitudes plotted against the corresponding photometric errors.

$\sim$ 8 km s^{-1} deg^{-1} along the projected major axis of Sculptor, likely due to intrinsic rotation. Also Coleman et al. (2005) and Westfall et al. (2006) by means of wide-field medium resolution Ca II triplet spectroscopy of RGB stars independently confirmed the presence of two distinct components. Martínez-Vázquez et al. (2016) detected the presence of a significant metallicity spread ($\sim$ 2 dex) within the RR Lyrae population, which is a population older than 10 Gyr. This suggests that Sculptor underwent an efficient early chemical enrichment fast enough to be recorded by the RR Lyrae. de Boer et al. (2012b) presented the SFH of Sculptor based on deep wide-field B, V, I photometry taken with Mosaic II camera at the CTIO 4 m Blanco telescope on an area of 1 deg^2 centered on Sculptor (de Boer et al. 2011). de Boer et al. (2012b) found that Sculptor is dominated by an old ($>$ 10 Gyr) metal poor stars, but that younger, more metal-rich populations are also present.

In this paper we present the analysis of the SFH of the Sculptor dwarf spheroidal based on deep wide-field, ground-based photometry. This study is organized as follows: in § 3.3, the observations, data reduction, the derivation of the photometry, the photometric calibration and the colour-magnitude diagram (CMD) of Sculptor are presented. In § 3.4 we discuss completeness tests, error simulations and the procedure of the SFH derivation. In § 3.5 we present a

Table 3.1: The main properties of the Sculptor dSph

Quantity	Value	References[a]
RA, α (J2000.0)	$1^h00^m09^s.4$	(1)
Dec, δ (J2000.0)	-33° 42′ 33.0″	(1)
Galactic longitude, l (°)	287.53	(1)
Galactic latitude, b (°)	-83.16	(1)
Galactocentric distance (kpc)	86±5	(2)
Heliocentric velocity (km s^{-1})	109.9±1.4	(3)
Ellipticity, e	0.32 ± 0.03	(4)
Position angle (°)	99±1	(4)
Core radius (′)	5.8±1.6	(4)
Tidal radius (′)	76.5±5.0	(4)
Luminosity, L_V ($L_\odot$)	$(2.03 \pm 0.79)\times10^6$	(5)
Absolute magnitude,M_V	-10.94 ± 0.58	(5)
Total mass, ($M_\odot$)	$(3.1 \pm 0.2)\times10^7$	(5)
Mass to light ratio, $M_\odot/L_\odot$	15.4 ± 6.9	(5)

[a](1) de Vaucouleurs et al. (1991); (2) Pietrzyński et al. (2008); (3) Queloz et al. (1995); (4) Irwin & Hatzidimitriou (1995); (5) Łokas (2009).

discussion about the achieved results. Finally, in § 3.6 we provide a summary and conclusions.

3.3 Observations and Data Reduction

The deep wide-field photometry we present in this work is a stack of many observations in g and r filters, (see Table 3.2 for details), taken with DECam (Flaugher et al. 2015) at the Blanco 4m telescope at the Cerro Tololo Inter-American Observatory (CTIO), reduced with the NOAO Community Pipeline (Valdes et al. 2014) and obtained from the NOAO Science Archive (Seaman et al. 2002). We obtained a stacked image for each filter as an average of all the scientific observations listed in Table 3.2 and we concentrated our analysis on the central CCDs centered on the galaxy, with a corresponding radial extension of $\sim$ 20 arcmin from the center of Sculpor. The total exposure time is 4800 s in the g filter and 4500 s in the r filter.

The photometry on stacked images and on calibration images has been performed making use of DAOPHOT/ALLSTAR suite of programs (Stetson et al. 1990). We used as point-spread function (PSF) a Moffat function with parameter $\beta = 2.5$ and radius of $R_{PSF} = 15$ pixels. A linearly varying PSF with the

Table 3.2: A summary of the available observational datasets

Calibration Images					
Filter	UT	Exposure(s)	Seeing(")	Program	PI
g	2013/08/19	300×1	$1.2'' - 1.4''$	2013B-0325[Scl]	Vivas
g	2013/08/19	120×9	$1.2'' - 1.4''$	2013B-0325[$Stripe82$]	Vivas
r	2013/08/19	300×1	$0.9'' - 1.1''$	2013B-0325[Scl]	Vivas
r	2013/08/19	120×7	$0.9'' - 1.1''$	2013B-0325[$Stripe82$]	Vivas
Scientific Images					
Filter	UT	Exposure(s)	Seeing(")	Program	PI
g	2013/08/19	300×16	$1.2'' - 1.4''$	2013B-0325	Vivas
r	2013/08/19	300×15	$0.9'' - 1.1''$	2013B-0325	Vivas

position of the stars has been derived for each stacked image by fitting 129 stars in the g filter and 60 stars in the r filter. In order to reduce to 1% the impact of the so called "brighter-fatter" effect (Antilogus et al. 2014) we have chosen only stars with $5 - 10$ K adu peak, excluding in this way the brightest stars. From the output of ALLSTAR, only objects with $\sigma \leqslant 0.2$ and $-0.5 \leqslant$SHARP$\leqslant 0.5$, were taken into consideration, in order to remove poorly measured stars, and galaxies. In Fig. 3.2 are plotted the magnitudes and the corresponding photometric errors for each filter with the restrictions above applied.

With the two catalogues in the g and r filters in hand, we performed the match using the packages DAOMATCH and DAOMASTER (Stetson 1993). From this match, the final total catalogue in g and r filters contains $\sim$ 96000 stars. We performed the aperture corrections for each filter, from the comparison between aperture and PSF magnitudes, finding for the g filter 0.0121 mag and for the r filter 0.0351 mag. Then we corrected for the exposure time, in g filter applying $+2.5 \times \log(300)$, while in r filter, $+2.5 \times \log(300)$. The quantities into the parenthesis have been calculated as the average of each exposure time in each filter.

In order to calibrate the photometry derived from the stacked images for each filter we have performed a two step calibration. The final scientific stacked images are composed among the others by a set of observations performed by Vivas (see last four rows in Table 3.2). Thus, we firstly performed PSF photometry on the stacked images of Sculptor by Vivas, obtaining the catalog in g and r filters. Then, we retrieved the PSF photometry of the single images of the standard stars observed the same night, see Stripe 82 observations in Table 3.2. We indentified the standard stars by using the SDSS Stripe 82 Standard Stars Catalog (Ivezić et al. 2007). The magnitudes of photometric standard stars has been compared to the SDSS Stripe 82 catalog in order to obtain the extinction coefficients for that night for both filters. Knowing the

Table 3.3: Parameters used for calibrating the photometry with the associated errors

Parameter	Values
k_g	-0.1514 ± 0.0064
c_{g1}	0.1157 ± 0.0029
g_0	25.4106 ± 0.0083
k_r	-0.1264 ± 0.0082
c_{r1}	0.0918 ± 0.0037
r_0	25.5771 ± 0.0106
z_g	25.3062 ± 0.0008
c_{g2}	0.1113 ± 0.0014
z_r	25.4677 ± 0.0007
c_{r2}	0.0902 ± 0.0012

extinction coeffiecients and the photometry of standard stars, we derived the equations for the standard calibration:

$$\begin{aligned} g' - g &= k_g \times X_g + c_{g1} \times (g' - r') + g_0 \\ r' - r &= k_r \times X_r + c_{r1} \times (g' - r') + r_0 \end{aligned} \tag{3.1}$$

where g', r' are the calibrated magnitudes, g, r, the observed magnitudes, k_g, k_r the airmass coeffiecients, X_g, X_r the effective airmasses, c_g, c_r, the colour therms and g_0, r_0, the photometric zero points. We derived the photometric solution using a polynomial regression model for the three independent variables. The root mean square error associated to this transformation are 0.0158 mag in g filter and 0.0201 mag in r filter, hence indicating a good match with the standard system.

Using the system of equations above we applied the calibration to the Vivas' catalog. In this way these stars can serve as local standards. Then, from the comparison between the magnitudes of the local standards with the full catalog, we obtained the equations to calibrate the full catalog:

$$\begin{aligned} g' - g &= c_{g2} \times (g' - r') + z_g \\ r' - r &= c_{r2} \times (g' - r') + z_r \end{aligned} \tag{3.2}$$

where c_{g2}, c_{r2} are the colour therms and z_g, z_r, the photometric zero points. In Table 3.3 are listed all the coeffiecients relative to the two obtained photometric tranformations, with the corresponding errors.

3.3.1 The Colour-Magnitude Diagram

The CMD we derived for Sculptor from our photometry extends ~ 2 mag below the MS turn-off (see Figure 3.3), thus allowing us to extract the information relative to star formation also for the earliest epochs. Figure 3.3 shows the obtained CMD, corrected by reddening ($A_g = 0.06$, $A_r = 0.042$ (Schlegel et al. 1998; Schlafly & Finkbeiner 2011)), where we have over plotted four isochrones from the BaSTI stellar evolutionary library (Pietrinferni et al. 2004) using a distance modulus of $(m - M)_0 = 19.57$ (Menzies et al. 2011). The main-sequence (MS) is well matched by isochrones of $[Fe/H] = -1.7$ and $[Fe/H] = -1.5$ and an age of about 13 Gyr. The RGB locus is very broad showing a metallicity spread between $[Fe/H] = -2.2$ and -1.3. Actually, an exhaustive spectroscopic analysis of the RGB has shown that this dwarf seems to have a significant spread that varies with position on the RGB (de Boer et al. 2011). In the obtained CMD there is a region ($-0.3 \lesssim (g-r)_0 \lesssim 0.08$, $21.5 \lesssim r_0 \lesssim 23.2$) that appears to be populated by Blue Straggler stars (BSS) (Mapelli et al. 2009; Monelli et al. 2012).

3.4 Derivation of the SFH

In order to retrieve the SFH of Sculptor we have followed the prescription outlined in Aparicio & Hidalgo (2009) and Hidalgo et al. (2011). This method allows to derive the star formation rate as a function of time and the age-metallicity relation. The three main used codes are: (1) IAC-Star (Aparicio & Gallart 2004), that computes synthetic CMDs (sCMDs); (2) IAC-pop (Aparicio & Hidalgo 2009), the core algorithm for the calculation of the SFH solutions; (3) MinnIAC (Hidalgo et al. 2011), a suite of routines that manages the process of sampling the parameter space, creating input data and averaging solutions.

Firstly, making use of the code IAC-star (Aparicio & Gallart 2004) and the BaSTI (Pietrinferni et al. 2004) stellar evolutionary library, we computed a synthetic CMD (sCMD) to be used for the analysis of the Sculptor stellar properties, with 5×10^6 stars, characterized by a constant star formation rate (SFR) between 0 and 13.5 Gyr and an uniform distribution of metallicity of $0.0001 \leqslant Z \leqslant 0.002$ for all ages. This metallicity range has been fixed accordingly to the metallicity distribution function (MDF) by Kirby et al. (2011b). We adopted the bolometric corrections for the SLOAN photometric systems provided by Pietrinferni et al. (2004), based on the model atmospheres by Castelli & Kurucz (1993). We used as initial mass function (IMF) the one by Kroupa (2002). For the binary star distribution $\beta(f, q_{min})$ we adopted a fraction of binary stars $f = 0.3$ with a flat distribution of the secondary to primary stellar mass ratio,

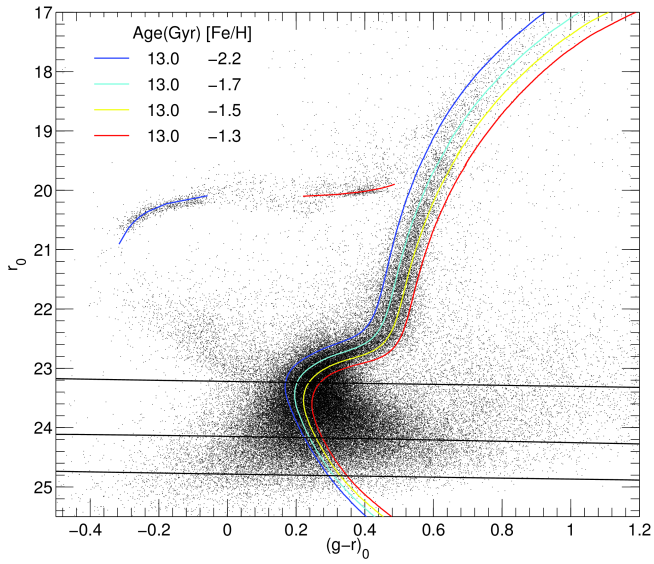

Figure 3.3: Observed CMD of Sculptor dSph. Four isochrones from the BaSTI stellar evolutionary library have been superimposed on the CMD, see the labels for details. The Blue Horizontal Branch (BHB) and Red Horizontal Branch (RHB) are fitted with a Zero Age Horizontal Branch (ZAHB) of $[Fe/H] = -2.2$ and $[Fe/H] = -1.3$ respectively (solid blue and red lines in the electronic version). Completeness levels are over plotted as black lines for values corresponding to 90%, 75% and 50%

q, with minimum $q_{min} = 0.5$.

As detailed in Aparicio & Gallart (1995), the simulation of observational effects is a key step for the interpretation of real data. In particular, to obtain a realistic model CMD to be compared with the real one, we need to simulate the observational effects that affect the real data. In order to estimate the completeness and uncertainties of our photometry we followed the standard technique of injecting a list of artificial stars in each stacked image and then re-deriving the photometry in the same way as done for real stars (see Hidalgo et al. (2011)). We injected 5×10^6 stars in each image along an uniform grid, with a separation of at least $2 \times R_{PSF} + 1$ pixels between the centroids of the artificial stars. The stars have been chosen in order to cover the whole range of luminosity and colour of the observed CMD (oCMD), in a colour range of $-1.25 \leqslant (g - r) \leqslant 2$ and a magnitude range of $16.75 \leqslant g, r \leqslant 26$; in particular we populated more the turn-off (TO) region $22 \leqslant g, r \leqslant 26$ with 3.5×10^6 stars, since it is the region of highest interest for the derivation of the SFH, then the red-giant-branch (RGB) region $19 \leqslant g, r \leqslant 22$ with 1×10^6 stars, and finally, the upper part of the colour-magnitude diagram in the magnitude range of $16.75 \leqslant g, r \leqslant 19$ with 0.5×10^6 stars.

In Fig. 3.3, we have over-plotted on the CMD of Sculptor the 50%, 75% and 90% completeness levels. The completeness has been calculated as the ratio of the number of artificial stars recovered to the number of all injected stars in each colour and magnitude interval. For each artificial star we have recorded the injected magnitude m_{inj}, the recovered magnitude m_{rec} and the position on the frame. We use the difference between the injected and recovered magnitudes ($m_{inj} - m_{rec}$) and the position of the synthetic star in the image to simulate the observational effects on the observed CMD. See Hidalgo et al. (2011) for a full description of the procedure.

Figure 3.4 shows the sCMD accounting for the observational effects simulation.

To obtain the SFH, the distribution of stars in the oCMD is compared with the distribution of stars of each simple stellar population (SSPs) in the sCMD. The SSPs are selected by defining age and metallicity bins for the synthetic stars. For the age we have chosen intervals of 2 Gyr for the first 8 Gyr and a smaller one, of 0.5 Gyr, for the last interval between 8 Gyr and 13.5 Gyr, since higher resolution is necessary to well characterize the earliest SFH phase. The metallicity bins adopted: $(0.01,\ 0.1,\ 0.3,\ 0.5,\ 1,\ 2) \times 10^{-3}$. The higher the metallicities, the wider the intervals. Both CMDs are sampled by using *bundles*, i.e. macroregions which sample main features of the CMDs, as shown in Fig. 3.4. Each of these bundles has a weight on the solution, given by the number of boxes of a fixed size in color and in magnitude defined in them. The

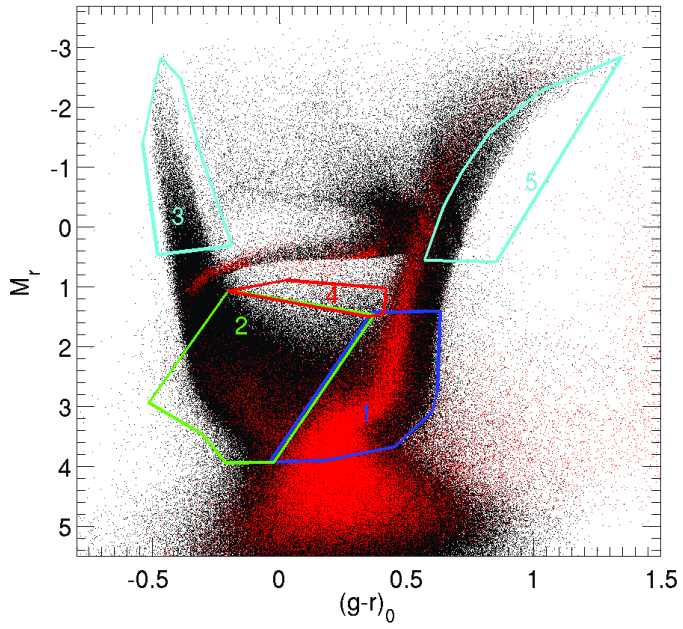

Figure 3.4: Synthetic CMD with the simulated observational effects (black) with overplotted the observed CMD (red). Bundles are the regions numbered from 1 to 5, see text for details.

Table 3.4: Box sizes in each bundle that sample the observed CMD

Bundle #	Δcol	Δmag	*Boxes*
1	0.025	0.125	1020
2	0.1	0.205	150
3	0.1	0.23	30
4	0.1	0.23	3
5	1.5	0.67	1

larger the number of boxes, the larger the weight in the SFH. Figure 3.4 shows the selected bundles. Table 3.4 shows the weight of each bundle in the solution.

In order to minimize the dependence of the solution on the CMDs sampling parameters, we obtained 24 solutions varying the CMD binning within each bundle and the SSPs sampling. We have shifted by a 30% the age and metallicity in a total of 12 combinations of SSPs, each one sampled with two slightly different combinations of boxes distribution in the bundles. To limit the effects on the solution due to uncertainties related to the distance modulus, photometric calibration and reddening we have shifted the oCMD 25 times along a regular grid with nodes in colour $\Delta(g-r) = [-0.1, -0.05,\ 0,\ 0.05,\ 0.1]$ and magnitude $\Delta r = [-0.2, -0.1,\ 0,\ 0.1,\ 0.2]$. For each node we have calculated the 24 solutions described above, obtaining a total of 600 solutions. For each node a mean solution $\overline{\psi}$ and its $\overline{\chi^2_\nu}$ is calculated. In this way we have obtained 25 different $\overline{\chi^2_\nu}$, the one with the minimum value indicates the best solution. The best solution we have found is the one with a shift of -0.05 mag in colour and no shift in r magnitude.

For an extensive description of the five bundles adopted and how we performed the minimization of the solution on the CMDs sampling parameters we refer to Hidalgo et al. (2011) (see also Bettinelli et al. (2018)).

3.4.1 The Global SFH of Sculptor

Fig. 3.5 shows the star formation rate as a function of time, $\psi(t)$, the age-metallicity relation, $Z(t)$, and the cumulative mass function for Sculptor. The age resolution of our derived SFH indicates that Sculptor has experienced a single event of star formation limited to the first $\sim$ 2 Gyrs after Big Bang, producing $\sim$ 70% of its mass about 12 Gyr ago. The mean metallicity retrieved is $[Fe/H] \sim -1.8$. In Fig. 3.6 the Hess diagrams of the oCMD (left panel), the best solution CMD (middle panel) and the residuals (right panel) are shown. From the residuals diagram, with the values expressed in units of Poisson error, there is a good agreement between the observed and simulated CMD especially

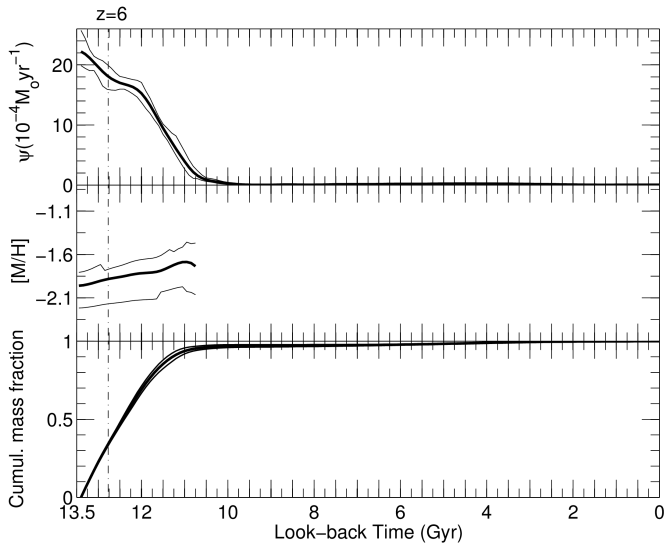

Figure 3.5: Results of the Sculptor SFH. Top panel: SFH as a function of time ($\psi(t)$). Middle panel: metallicity of the system as a function of the time. Lower panel: cumulative mass fraction as a function of the time. 1σ uncertainties have been drawn as thin lines.

in the MS and SGB locus.

3.4.2 The Radial SFH of Sculptor

To investigate whether a radial gradient of stellar populations exists in Sculptor, we derived the SFH by dividing the sampled area into four elliptical regions with delimiting major axis of 8.59, 13.41, 19.35 and 39.46 arcmin, see Fig. 3.7. The center assumed for the analysis is coincident with the one tabulated by Shapley (1938) in J2000.0 coordinates $(15.03898, -33.70903)$. The position angle adopted is $\theta = 99$ and ellipticity 0.32 (Irwin & Hatzidimitriou 1995). The major axes have been fixed in order to have 24000 stars in each elliptical region for statistical consistency. Figure 3.8 shows the CMDs for each elliptical region in which the galaxy has been divided.

For each region the SFH has been derived in the same ways for the global

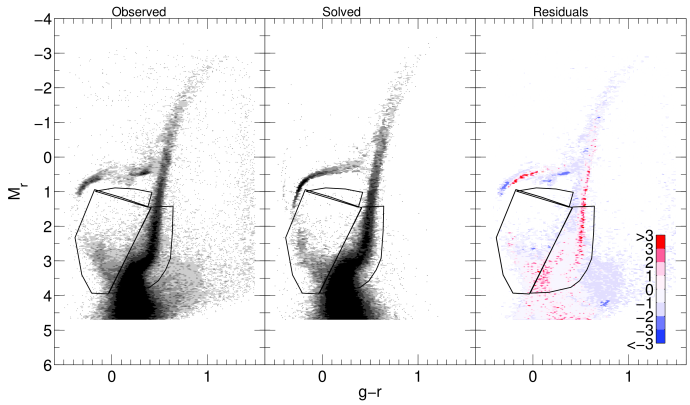

Figure 3.6: Hess diagrams relative to the observed CMD (left panel), best solution CMD (middle panel) and residuals CMD (right panel). The residuals are in units of Poisson uncertainties. Residuals from $\sigma = 0$ to $\sigma = 3$ refer to the case in which the model predicts more stars in respect to the oCMD. Residuals from $\sigma = 0$ to $\sigma = -3$ refer to the case in which the model predicts less stars in respect to the oCMD. Gray levels show the density of stars. A factor of 2 in density exists between each two successive gray levels. The single dots are shown where the density is less than 2 stars per $(0.02)^2$ mag. The boxes show the areas of the CMD used for the derivation of the SFH.

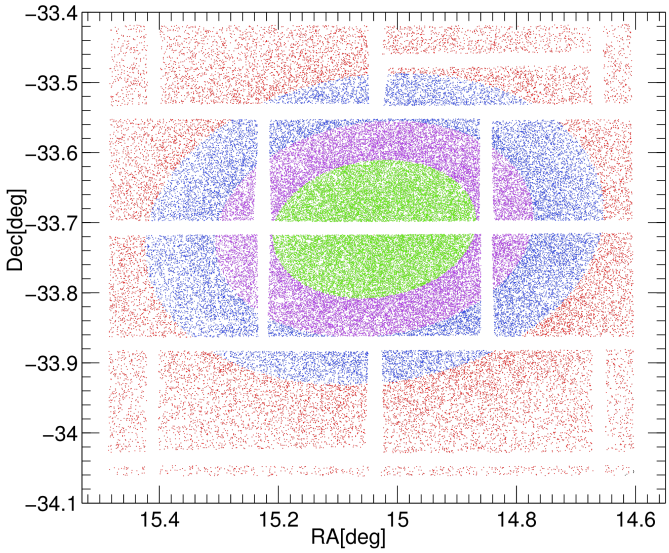

Figure 3.7: Stellar spatial distribution, the ellipse major axis are in the intervals $a \leq 8.59$ arcmin for green points; $8.59 < a \leq 13.41$ arcmin for magenta points; $13.41 < a \leq 19.35$ arcmin for blue points; and $a \geq 19.35$ for red points. The region of the core radius is well represented by the innermost elliptical region (green points).

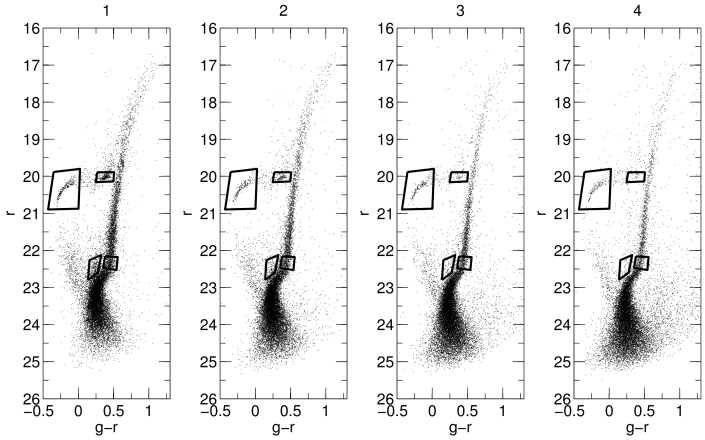

Figure 3.8: From left to right CMDs of Sculptor from the innermost elliptical region to the outer. Region 1 refers to the elliptical area within the major axis $a \leq 8.60$ arcmin, region 2 to the major axis $8.60 \leq a \leq 13.42$ arcmin, region 3 to the major axis $13.42 \leq a \leq 19.35$ arcmin and region 4 to the major axis $19.35 \leq a \leq 39.46$ arcmin. On the CMDs are drawn boxes indicating the region of the BHB, RHB and the spur region, near the MS. A box is indicated at the base of the RGB, see text for details.

Table 3.5: Ratios between the number of stars in the RHB, BHB and the spur region in respect to the RGB

Region	RHB/RGB	BHB/RGB	$spur/RGB$
1	0.51	0.50	0.55
2	0.32	0.47	0.38
3	0.16	0.56	0.27
4	0.11	0.52	0.25

one but using in each case the corresponding oCMD (see Fig. 3.8).

Regarding the morphological changes connected to stellar populations variations, it is remarkable how the horizontal branch (HB) changes with distance: a populated red HB (RHB) is present in the center but it seems to be less populated moving outwards, while blue HB (BHB) stars seem constant along all the radial distance. This suggests the presence of an extended old metal poor stellar population and a more centrally concentrated old more metal rich stellar population.

In order to obtain a deeper insight on this effect, we calculated the ratios between the number of stars in the RHB, BHB and the so called *spur* (Hurley-Keller et al. 1999) region in respect to the RGB region indicated in Fig. 3.8. In Table 3.5 we report these ratios. They indicate that effectively RHB stars are more centrally concentrated while BHB stars more extended. This fact has been already shown in Tolstoy et al. (2004). The RGB seems to narrow when moving from region 1 to region 4, indicating a clear change in stellar populations. In Figure 3.8, we also indicate a box that extends from the MS TO region and is located between the canonical blue stragglers (BS) region and the SGB, which englobes the *spur*, a feature firstly identified in (Hurley-Keller et al. 1999), see Figure 3.9. The same feature is visible in the data presented in this work and it is interesting to note that this feature becomes weaker with the distance from the center of the galaxy. In particular, from the calculated ratios it appears that also the *spur* is more centrally concentrated, but at a lower extent, when compared to the RHB.

In Fig. 3.11 we show the resulting SFHs, the metallicity (see Fig. 2.10) and the cumulative mass fraction (see Fig. 3.12) as a function of time for all the four regions and in Figures 3.13 – 3.16 the corresponding Hess diagrams of the oCMD (left panel), the best solution CMD (middle panel) and the residuals (right panel) are plotted. In each region the star formation is consistent, within our age resolution, with a single burst of star formation. From Fig. 3.11 it is appreciable that the duration of star formation is shorter going outwards and we will constrain it for each case subsequently. Within errors we have not detected any metallicity gradient. Also the mean ages, within 1σ are consistent for the

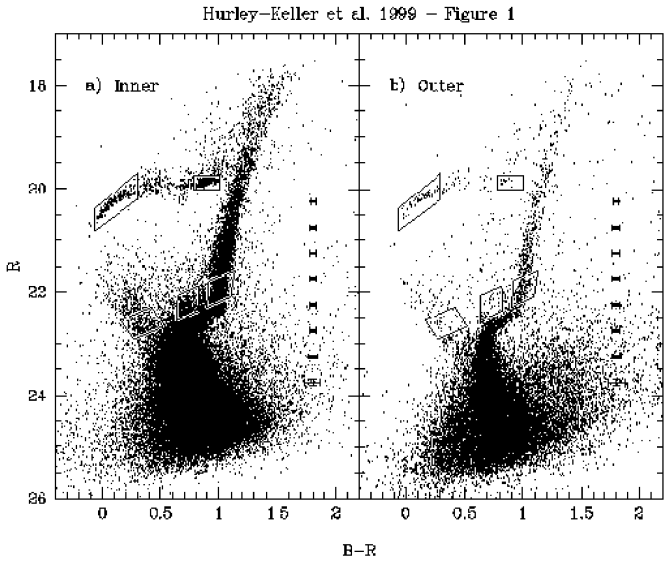

Figure 3.9: CMDs of the inner and outer regions of Sculptor with boxes for reference (see text). (a) CMD of the inner region of Sculptor with more than 70000 stars. (b) CMD of the outer region of Scultpor containing about 30000 stars (Hurley-Keller et al. 1999).

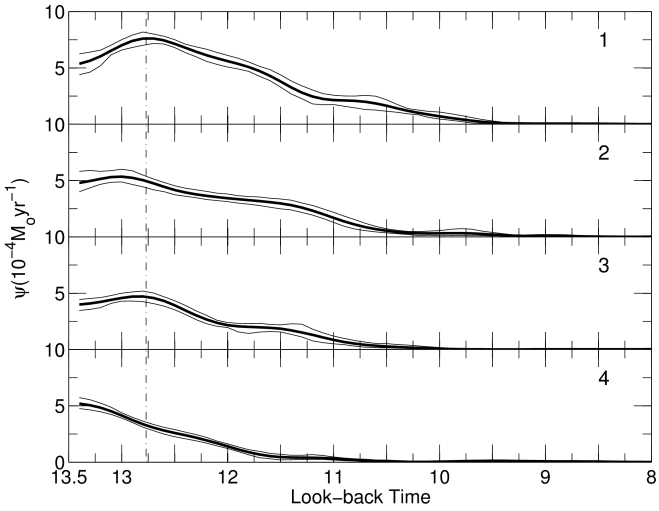

Figure 3.10: Results of the radial SFH for the four regions defined as in Figure 3.7. Uncertainties have been drawn as thin lines. In the panels each region has been indicated with the corresponding number from 1 to 4.

inner 3 regions except region 4 since the measured values are: 12.05 ± 0.13, 12.07 ± 0.13, 12.23 ± 0.13 and 12.45 ± 0.14 Gyr. By inspecting Fig. 3.11 it can be noted that there is a trend of the SFH with distance that involves also the 3 innermost regions. This suggests that a population gradient is present in Sculptor.

3.4.3 Constraining the duration of the main SFH burst

It is known that observational effects tend to broaden the main features of the SFH, mostly those reflecting the oldest episodes of star formation (Aparicio et al. 2016). To investigate this effect in the radial SFH, we have followed the procedure outlined in Hidalgo et al. (2011), to see if hints of different time scales of star formation are detectable. For this test we derived the SFHs for a number of mock stellar populations in the same way as for observational data adopting for each radial region the corresponding model which accounts for the

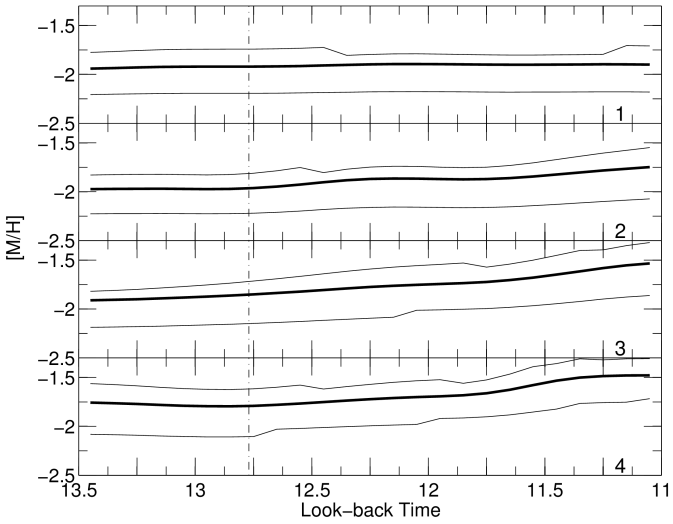

Figure 3.11: Metallicity as a function of look-back time for the four regions defined as in Figure 3.7. Uncertainties have been drawn as thin lines. In the panels each region has been indicated with the corresponding number from 1 to 4.

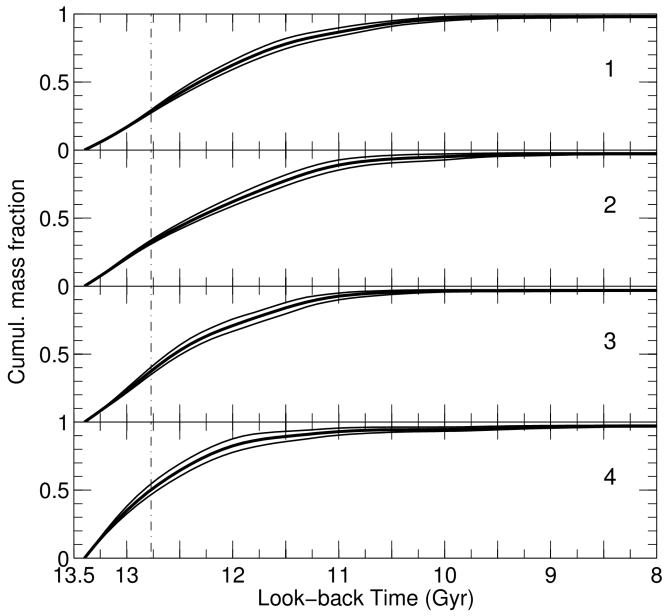

Figure 3.12: Results of the radial cumulative mass fraction for the four regions defined as in Figure 3.7. Uncertainties have been drawn as thin lines. In the panels each region has been indicated with the corresponding number from 1 to 4.

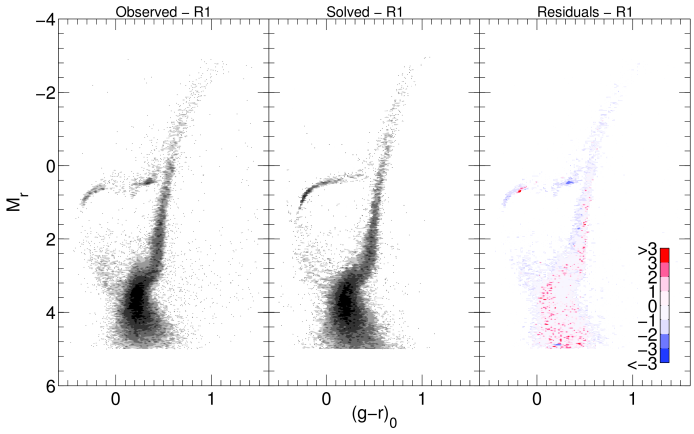

Figure 3.13: Hess diagrams relative to the CMD of the stars within $a \leq 8.59$ arcmin, see green points in Figure 3.7 (left panel), best solution CMD (middle panel) and residuals CMD (right panel). The residuals are in units of Poisson uncertainties.

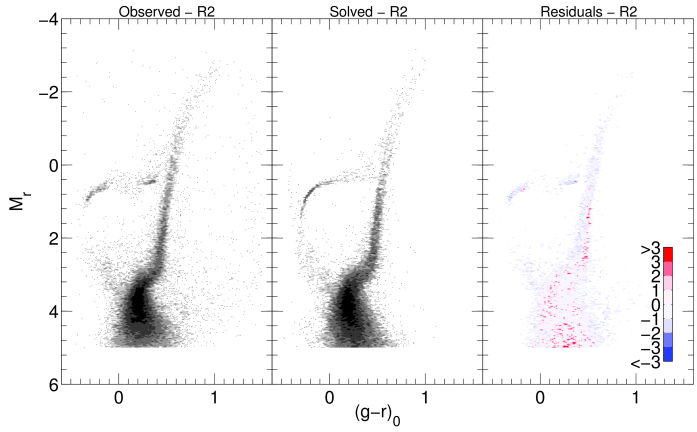

Figure 3.14: Same as in Figure 3.13 but for stars within $8.59 < a \leq 13.41$, see magenta points in Figure 3.7

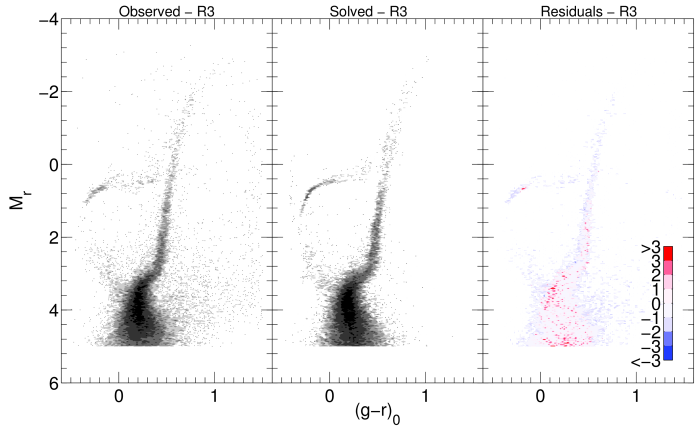

Figure 3.15: Same as in Figure 3.13 but for stars within $13.41 < a \leq 19.35$, see blue points in Figure 3.7.

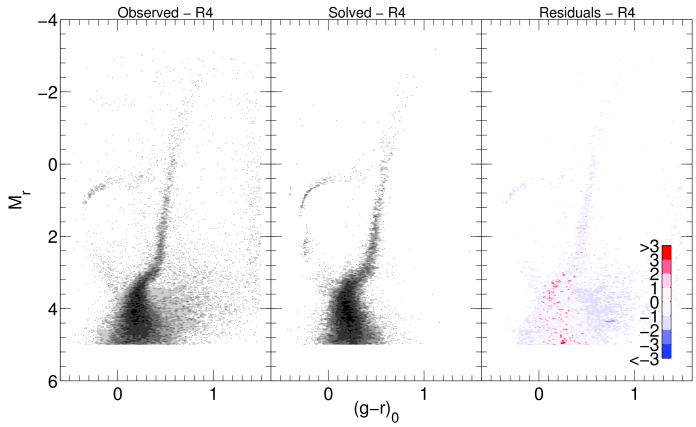

Figure 3.16: Same as in Figure 3.13 but for stars within $a \geq 19.35$, see red points in Figure 3.7

local photometric errors of the region under consideration. The mock stellar populations are characterized by an increasing age width all starting 13.5 Gyr ago. Even though the peak is situated at $\sim$ 12.8 Gyr in three of the four regions, we use the oldest age so that the duration of the SFH obtained is a limit since it is expected a lower difference between the size of the injected and recovered SFH at younger ages. The duration of each burst, in terms of Full Width at Half Maximum ($FWHM_{in}$), has been chosen to be: 0.25, 0.5, 0.75, 1, 1.5, 2 Gyr. Metallicity has been fixed to $[Fe/H] = -1.86$, which is the mean metallicity recovered for Sculptor.

In Table 3.6 we summarize for all the regions the mean recovered $FWHM_{rec}$ of each mock burst.

Fitting a single Gaussian profile to each SFH of Sculptor in the four regions we estimate the following typical width for the observed $\psi(t)$ in the age range $10 - 13.5$ Gyr: $\sigma_{1-4} = 1.54, 1.28, 1.23, 1.02$ Gyr, which corresponds to a $FWHM_{obs} = 3.63, 3.01, 2.88, 2.39$ Gyr. In Figures 3.17 – 3.20 we have plotted, for each region, the $FWHM_{in}$ Gyr of the mock bursts and their associated mean recovered $FWHM_{rec}$. Fitting the resulting data with a quadratic polynomial we are able to constrain the period of star formation for each region. Table 3.7 summarizes the results, while Figure 3.21 shows the constrained du-

Table 3.6: List of the recuperated FWHM relative to the SFH of each mock bursts for each elliptical region.

$FWHM_{in}$	$FWHM_{rec-1}$	$FWHM_{rec-2}$	$FWHM_{rec-3}$	$FWHM_{rec-4}$
0.25	2.98	2.88	2.57	2.28
0.5	3.02	2.92	2.69	2.35
0.75	3.13	2.98	2.87	2.50
1	3.37	3.02	2.92	2.55
1.5	3.63	3.09	3.28	2.83
2	4.00	3.52	3.35	2.96

Table 3.7: Constrainment of the period of star formation for each elliptical region. $FWHM_{rec}$ refers to the real measured $FWHM$ for each SFH, while $FWHM_{in}$ is the associated constrained burst found by means of the quadratic fit. We also provide the errors associated to $FWHM_{in}$ in the last column.

Region	$FWHM_{rec}$	$FWHM_{in}$	$\sigma FWHM_{in}$
1	3.63	1.50	0.07
2	3.01	1.04	0.07
3	2.88	0.80	0.07
4	2.39	0.54	0.05

ration of the bulk of the star formation as a function of radius.

The main star formation episode in each region decreases from the center outwards. The star formation in region 1 lasted $\sim 1.5 \pm 0.1$ Gyr, with its peak at ~ 12.8 Gyr ago. Its completion is well after the end of the epoch of reionization, which is fixed at ~ 12.77 Gyr (Becker et al. 2001). The star formation episode in region 4 has been confined to ~ 0.5 Gyr. Since the peak of star formation is at ~ 13.5 Gyr ago, in this region star formation terminated before the end of the epoch of reionization. This suggest that Sculptor, unlike Sextans, has continued forming stars in its inner regions, because enriched gas probably concentrated there and permitted a prolonged period of star formation.

However, the peculiarity of Sculptor is the fact that it is embedded in two symmetrical HI clouds, see Figure 3.1 (Carignan et al. 1998;Bouchard et al. 2003;Piatek et al. 2006). It is thus interesting to investigate if this neutral gas could have been ejected by SN winds (Carignan et al. 1998). To this aim we calculated, as outlined in Hidalgo et al. (2011), the mechanical luminosity of the SNe released during the main star formation episode. This quantity, together with the value of the mass of gas of the galaxy can be compared with the results presented in Mac Low & Ferrara (1999) to discern if Sculptor had lost mass in the past and in the case the modality according to which it happened.

Using the results from the SFH, we have calculated that a total of $2.24 \times 10^6\,M_\odot$ of gas was converted into stars. We have derived this value by scaling

the SFH obtained from our observations to the whole galaxy using the King profile as obtained in Westfall et al. (2006). We obtained a total of 3.79×10^4 SNe assuming a minimum progenitor mass for core collapse SNe of $6.5\,M_\odot$ (Salaris & Cassisi 2005), and 2.12×10^4 SNe in the case of a minimum mass of $10\,M_\odot$. Assuming an energy release per SN of 10^{51}erg (Leitherer et al. 1999) and a duration of the star formation episode of 1.5 Gyr, we have calculated a total mechanical luminosity released during this episode of $L_w = 8.01 \times 10^{38}$ erg/s and $L_w = 4.48 \times 10^{38}$ erg/s, for the two assumed minimum mass values for type II SNe, respectively. These values would place Sculptor in the region of blow-out/mass loss regime, from the comparison with the model results of Mac Low & Ferrara (1999) shown in their Figure 1. In a "blowout" the central SN explosions blow a hole through the intergalactic medium, accelerating some fraction of gas and releasing the energy of subsequent explosions without major effects on the remaining gas.

In other words, the star formation began with an initial strong burst slowed by gas loss due to supernovae explosions. Later the remaining gas concentrated again in the innermost region permitting a second or more episodes of star formation. The confinement obtained for the star formation episode of region 4 is likely the record of the primordial large scale star formation of Sculptor, which corresponds to the BHB stars that are present in each partial CMD in Figure 3.8.

Knowing the radial SFHs and following the prescription in Hidalgo et al. (2013) we are able to provide some predictions about the structural properties of this dwarf, such as the core radius and the total stellar mass. We fit our results with an exponential profile, $\psi(r) = M_0 e^{-r/\alpha_\psi}$, where M_0 is the central mass density and α_ψ is the scale length[1]. For Sculptor we derived $\alpha_\psi = 198 \pm 6$ pc and a core radius $CR_\psi = 320 \pm 6$ pc. Under the assumptions that the observed field provides a good representation of the whole galaxy and the radial profile of the stellar mass density follows the same $\psi(r)$ beyond the observed radius, we integrated the exponential profile, deriving a total stellar mass of $M = (6.3 \pm 0.4) \times 10^6 M_\odot$. These values are very similar to the ones obtained for Cetus in Hidalgo et al. (2013). This fact can indicate that the two galaxies have followed similar evolutionary paths.

3.5 Discussion

It is interesting to compare the results presented above with earlier work, such as the star formation computed by de Boer et al. (2012b), who have found an

[1] radius at which mass drops by e^{-1}

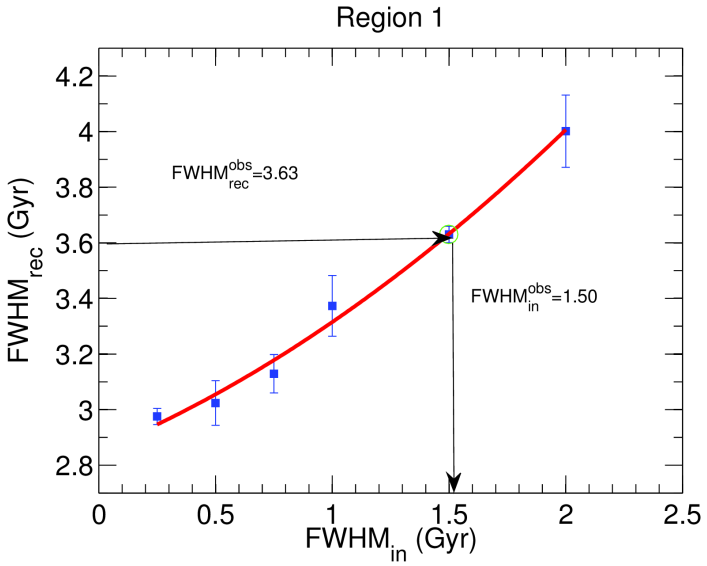

Figure 3.17: $FWHM_{in}$ is the Full Width at Half Maximum of the input mock bursts, $FWHM_{rec}$, the recuperated FWHM relative to the SFH of each mock bursts. Points have been fitted with a quadratic polynomial. Knowing the FWHM of the best SFH solution, making use of the intercept on the fitting red line (see green box) we confine the star formation burst to a value of $FWHM^{obs}_{in} \sim 1.4$ Gyr for region 1.

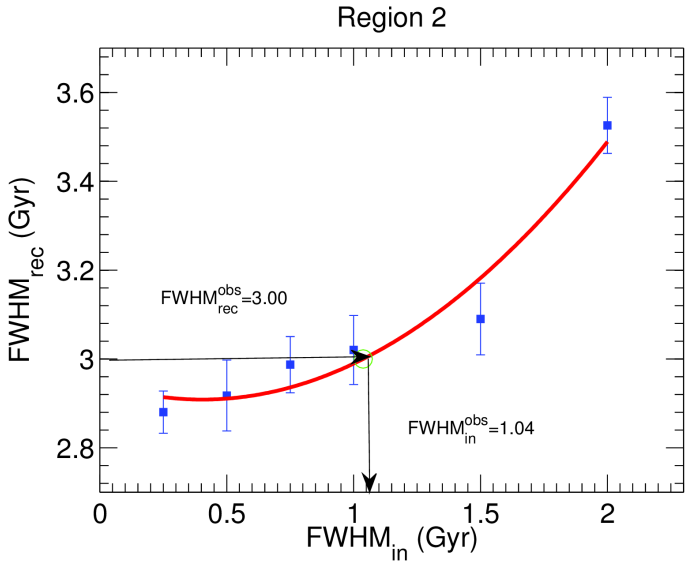

Figure 3.18: Same as Figure 3.17 but for region 2; we confine the star formation event to a value of $FWHM_{in}^{obs} \sim 1$ Gyr

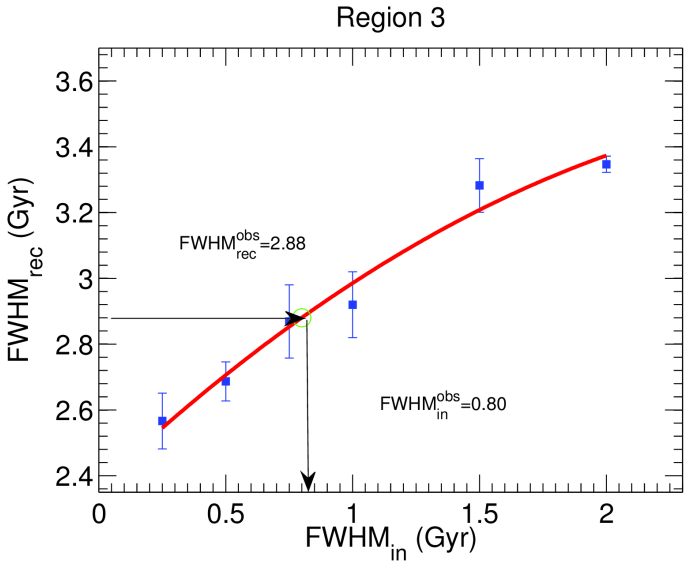

Figure 3.19: Same as Figure 3.17 but for region 3; we confine the star formation event to a value of $FWHM_{in}^{obs} \sim 0.8$

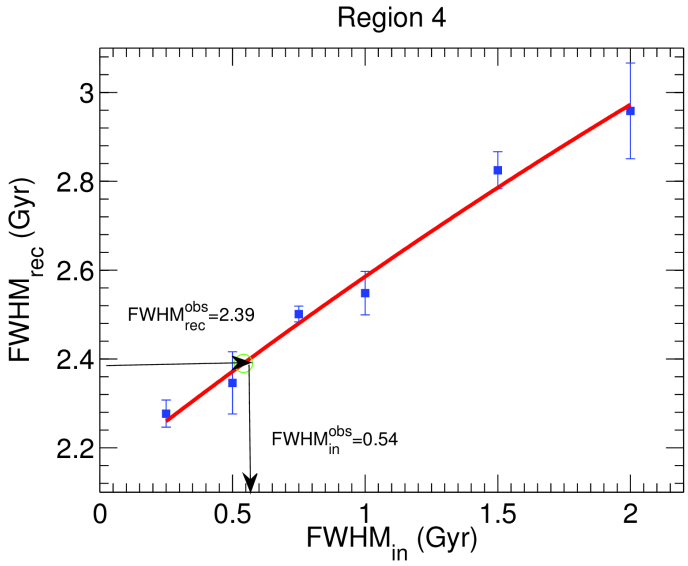

Figure 3.20: Same as Figure 3.17 but for region 4; we confine the star formation event to a value of $FWHM_{in}^{obs} \sim 0.5$ Gyr.

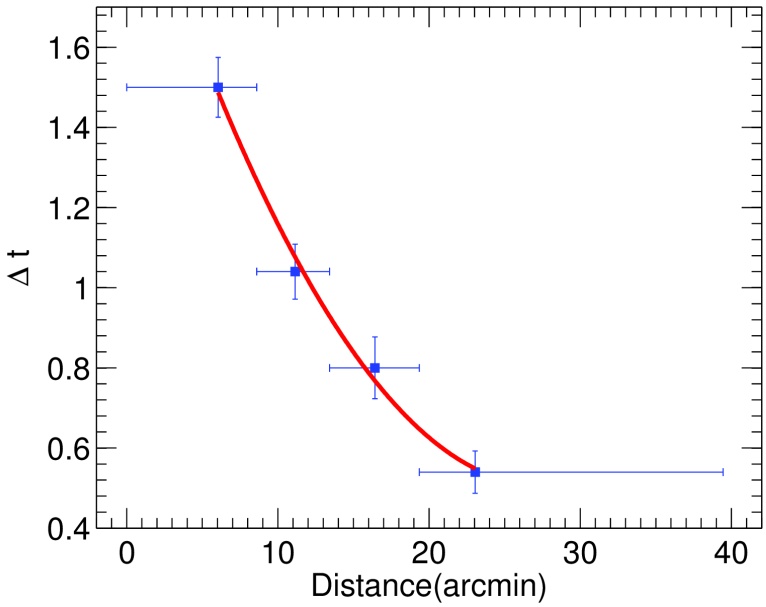

Figure 3.21: This figure summarizes the results achieved. The points represents the duration of the star formation in each region and a function of the distance from the center of Scultor. The horizontal error bars refer to the radial coverage of each individual region.

extended, continuous star formation of $6-7$ Gyr. Our results show that Sculptor stopped forming stars ~ 11.3 Gyr ago, thus indicating a duration of ~ 2.2 Gyr. The difference could be explained if we consider that our photometry is deeper that the one presented in de Boer et al. (2011) and allows us to better sample the oldest MS TO. From their radial study, de Boer et al. (2012b) found that the innermost annulus (whose extension is quite similar to the one adopted in the present analysis) can not be modeled with a single narrow burst of star formation, while, for the outer annulus of their catalogue, the recovered SFH can be well approximated to a single short burst of star formation. As de Boer et al. (2012b) discussed, it is particularly challenging to properly reproduce the innermost region of Sculptor, in part for crowding effects but mostly for the complex star formation. This fact can be intuited also inspecting Fig. 3.8: all the features of the CMD appear more narrow going outwards. The broadening can be attributed to metallicity/age spread, thus suggesting a longer star formation in the central regions.

From our analysis we derived a mean metallicity for Sculptor of $[Fe/H] = -1.86$. This value is in accordance with the mean value measured by means of spectroscopy of single stars by Helmi et al. (2006) along a radius of 40 arcmin from the center of Sculptor. Tolstoy et al. (2004) identified two distinct stellar components in Sculptor, one metal-rich $-0.9 > [Fe/H] > -1,7$, one metal-poor $-1.7 > [Fe/H] > -2.8$. The peak of the global MDF is centered at $[Fe/H] = -1.8$. Other spectroscopic measurements have been perfomed by Kirby et al. (2009) who measured a mean metallicity of $[Fe/H] = -1.58$ and by Battaglia et al. (2008b) that found a mean of $[Fe/H] = -1.56$, both sampled stars out to about 11 arcmin.

From the constraining of the SFHs radially we derived a period of ~ 0.5 Gyr for the outermost region which is in striking agreement with the single early episode of 0.5 Gyr computed by Amorisco et al. (2014) during which SNe II explosions would be sufficient to build a substantial dark matter core.

The radial gradient found in Sculptor is in agreement with outside-in scenarios of dwarf galaxy evolution, which has been found in other dwarf galaxies of the Local Group (Hidalgo et al. 2013), when these type of galaxies run out of gas on the outskirts but are able to keep forming stars in the center for a longer period.

Finally, we would like an answer to the question if Sculptor is a fossil of the pre-reionization era, as introduced in Ricotti & Gnedin (2005): a dwarf that has experienced more than the 70% of its star formation before the end of the reionization and that has a luminosity $L_V < 10^6\, L_\odot$. Sculptor does not satisfies the second condition, since it has a luminosity $L_V = (2.03 \pm 0.79) \times 10^6\, L_\odot$ (Łokas 2009). According to our results region 1 is characterized by a duration

of the episode of star formation of ~ 1.5 Gyr which indicates a star formation extended also after the end of the epoch of reionization. For the outermost region 4, on the contrary, its star formation has been confined to ~ 0.5 Gyr. There the star formation ended before or contemporaneous with the end of the epoch of reionization. From the considerations listed above, Sculptor can not be classified strictly as a true fossil of the pre-reionization era as opposed to what we found for Sextans (Bettinelli et al. 2018). Our results suggest that Sculptor could have suffered in the past a blowout as described in Mac Low & Ferrara (1999). It is thus tempting to link this to the possible formation of the HI distribution embedding Sculptor (Carignan et al. 1998).

3.6 Summary and Conclusions

We have derived the global and radial SFH for the Sculptor dSph based on deep g,r photometry taken with DECam at the Blanco telescope.

The age resolution of our derived SFH indicates that Sculptor has experienced a single event of star formation limited to the first ~ 2 Gyrs after Big Bang, producing $\sim 70\%$ of its mass about 12 Gyr ago. The mean metallicity retrieved is $[Fe/H] \sim -1.8$. The retrieved metallicities are consistent with the spectroscopic measurements by Helmi et al. (2006) and Tolstoy et al. (2004). We have investigated how the SFH of Sculptor changes radially, subdividing in four regions the sampled area. In each region the star formation is consistent, within our age resolution, with a single burst of star formation of different duration. We find that the duration of the episodes of star formation increases towards the centre and we provide the intrinsic duration of these bursts. The innermost region presents the longer period of star formation of ~ 1.5 Gyr, in agreement with the estimate by Kirby et al. (2009) via chemo-dynamical models (see Figure 3.22), going outwards it decreases to ~ 0.54 Gyrs. These results suggest that Sculptor continued forming stars after the reionization epoch in its central part, while in the peripheral region the majority of stars were formed before or coincident with the end of the reionization epoch. Our results are compatible with an outside-in scenario of dwarf galaxy formation. Finally, from the calculation of the mechanical luminosity produced by SNe we can advance the hypothesis that Sculptor has suffered a 'blow out' in its early epochs that does not completely inhibit star formation. This result, together with the constraints by Ricotti & Gnedin (2005) indicate tha Sculptor can not be strictly considered a fossil of the pre-reionization era.

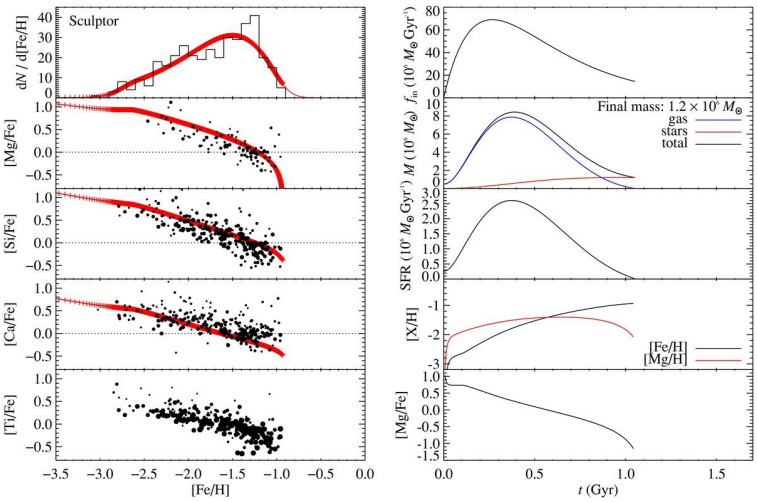

Figure 3.22: Observed abundance ratios and the best-fit gas flow and SFH model for Sculptor from (Kirby et al. 2011a). Left: the top panel shows the observed MDF as the black histogram and the modeled MDF in red. The model is convolved with an uncertainty function to mimic the broadening of the histogram induced by observational error. A cross marks each 1 Myr time step, but these are too closely spaced to discern for most of the metallicity range. Very few stars are expected to have formed at the low metallicities where the crosses are distinguishable. The other panels show the observed [Mg/Fe], [Si/Fe], [Ca/Fe], and [Ti/Fe] ratios as black points whose sizes are inversely proportional to measurement uncertainties. Only points with uncertainties less than 0.3 dex are shown. The red lines show the abundance ratios of the stars and gas at each time step. Right: the gas flow and SFH for the best-fit model. From top to bottom, the panels show the gas inflow rate; the stellar, gas-phase, and total baryonic mass; the SFR; the iron and magnesium abundances; and the [Mg/Fe] ratio, all as a function of time. The second panel also gives the final stellar mass in the model.

4

The Canarias Einstein Ring: a Newly Discovered Optical Einstein Ring

4.1 Abstract

We report the discovery of an optical Einstein Ring in the Sculptor constellation, IAC J010127-334319, in the vicinity of the Sculptor Dwarf Spheroidal Galaxy. It is an almost complete ring ($\sim 300°$) with a diameter of ~ 4.5 arcsec. The discovery was made serendipitously from inspecting Dark Energy Camera (DECam) archive imaging data. Confirmation of the object nature has been obtained by deriving spectroscopic redshifts for both components, lens and source, from observations at the 10.4 m Gran Telescopio CANARIAS (GTC) with the spectrograph OSIRIS. The lens, a massive early-type galaxy, has a redshift of z = 0.581 while the source is a starburst galaxy with redshift of z = 1.165. The total enclosed mass that produces the lensing effect has been estimated to be $M_{tot} = (1.86 \pm 0.23) \cdot 10^{12}\, M_{\odot}$.

4.2 Introduction

Strongly lensed galaxies are very important in the study of galaxy formation and evolution because they permit derivation of important physical parameters such as the total mass of the lensing object, without any assumption on the dynamics. Cases in which the Einstein ring (ER) is almost complete and the central lensing galaxy isolated are rare; these permit constraining with great accuracy the enclosed mass within the projected Einstein radius Θ_E (Kochanek

et al. 2001). Miralda-Escude & Lehar (1992) predicted several 10^6 optical ER to be detectable over the whole sky, down to a magnitude limit of $B = 26$. This notwithstanding, despite extensive surveys (see for example Bolton et al. 2008; Stark et al. 2013) only a few tens of complete or nearly complete optical ERs have been identified so far, and among these objects, only a few show a close similarity to the one we discuss in the present work.

The first ER to be discovered is the radio source MG1131+0456 (Hewitt et al. 1988). Warren et al. (1996) report the discovery of a partial ER ($\sim 170°$) with $\Theta_E \sim 1.35$ arcsec; the background OII emitting galaxy at z = 3.595 is lensed by an elliptical massive galaxy at z = 0.485. This is the first known case in the literature of a ER discovered at optical wavelengths. Cabanac et al. (2005) discovered an almost complete ER ($\sim 260°$) with $\Theta_E \sim 1.48$ arcsec produced by a massive and isolated elliptical galaxy at z = 0.986. The source galaxy is a starburst at z = 3.773. Then, a similar ER to the one we report in this Letter, in morphology, but not in the physics of the source galaxy, a BX galaxy, is the so called "Cosmic Horseshoe" (Belokurov et al. 2007); the ring extension is similar to the one we report here, ($\sim 300°$), but the Einstein radius is double, $\Theta_E \sim 5$ arcsec; the lensing galaxy has a huge mass of $\sim \mathrm{M} = 5.4 \times 10^{12}\,\mathrm{M}_{\odot}$. Other partial ER discovered recently are: the "Cosmic Eye" (Smail et al. 2007), the "8 o'clock arc" (Allam et al. 2007) and the "Clone" (Lin et al. 2009).

Here we report the discovery of IAC J010127-334319, an optical, almost complete ER, that we refer to as the "Canarias Einstein Ring", noticed as a peculiar object in DECam images. No previous reference to the object has been found in the literature. Subsequently we observed it with OSIRIS@GTC for a spectroscopic confirmation of its nature. In this Letter we provide the first physical parameters of this system. In the following discussion we assume a flat cosmology with $\Omega_m = 0.3$, $\Omega_\Lambda = 0.7$ and $H_0 = 70\,\mathrm{km\,s^{-1}\,Mpc^{-1}}$.

4.3 Discovery

The serendipitous discovery of IAC J010127-334319 was made while performing photometry on stacked images, in g and r filters, taken with DECam (Flaugher et al. 2015) at the Blanco 4m telescope at the Cerro Tololo Inter-American Observatory (CTIO), reduced with the NOAO Community Pipeline (Valdes et al. 2014) and obtained from the NOAO Science Archive (Seaman et al. 2002). The total exposure time is 7680 s in the g filter and 5700 s in the r filter. Figure 4.1 shows the resulting color composite image: it is evident that two components with different colors are present. In particular the central one (the lens) appears redder than the second component (the lensed image of the

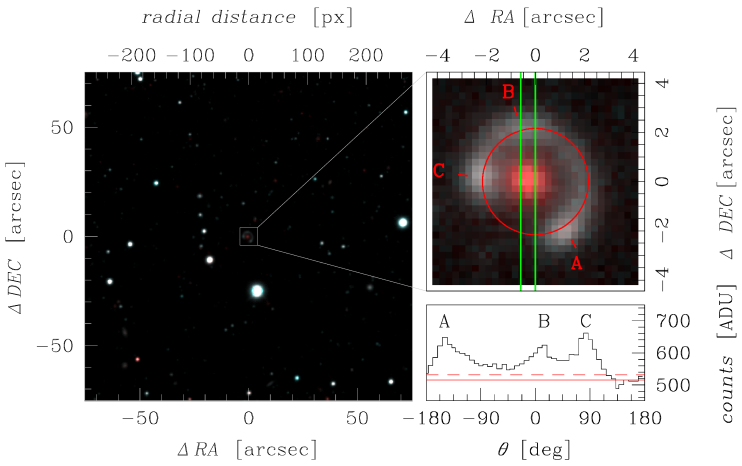

Figure 4.1: Composite g, r field of view of 2.5 arcmin × 2.5 arcmin centered on the object (on the left), North is up, while East points left; a zoom of the object with overplotted the best fitting circle, the slit position and width are also plotted as green lines (right upper panel); counts from photometry along the best fit circle of the ring (lower right panel): the measured sky value is indicated by the red solid line, the 1σ value is indicated by the red dashed one.

Table 4.1: List of parameters

Lens	
Right ascension(J2000):	$01^h01^m27.83^s$
Declination(J2000):	$-33°43'19.68''$
Redshift:	0.581 ± 0.001
Surface brightness Lens (g,r) [mag arcsec^{-2}]:	25.2, 22.2
Apparent magnitude (g,r)	23.61, 21.48
Absolute magnitude (g,r)	−21.05, −23.18

Ring	
Redshift:	1.165 ± 0.001
Einstein radius:	$2.16'' \pm 0.13$
Enclosed mass [10^{12} M$_\odot$]:	1.86 ± 0.23
Surface brightness A (g,r) [mag arcsec^{-2}]:	23.7, 22.9
Surface brightness B (g,r) [mag arcsec^{-2}]:	23.9, 23.2
Surface brightness C (g,r) [mag arcsec^{-2}]:	23.7, 23.0
Apparent magnitude (g,r)	20.94, 20.12

source), which in turn appears as elongated all around the first. The ring is almost perfectly circular with an apparent radius of 8 px which translates to 2.16 arcsec. Three peaks, A, B and C, are clearly visible (bottom right panel of Figure 4.1); they are located respectively at -150 deg, 14 deg and 83 deg from North counterclockwise. In Table 4.1 all the derived parameters for the object are listed. From the DECam photometry we estimated an apparent magnitude for the lens in both g and r bands of $g = 23.61$, $r = 21.40$. The color $(g-r) > 2$ indicates that this galaxy is probably a luminous red galaxy (Eisenstein et al. 2001). All the details about the photometric calibration will be given in a forthcoming paper (Bettinelli et al. in prep.).

4.4 Follow-Up Spectroscopy

In order to confirm the lensing nature of this system we performed a spectroscopic follow-up at the 10.4 m Gran Telescopio CANARIAS (GTC) on Roque de los Muchachos Observatory (La Palma, Spain) using the Optical System for Imaging and low-Intermediate-Resolution Integrated Spectroscopy (OSIRIS) spectrograph (Cepa 1998). OSIRIS has a mosaic of two E2V CCD42-82 (2048×4096 px). All the obtained spectra were registered on the second detector, which is the default for long-slit spectroscopy. We used a binning of 2×2 providing a pixel size of 0.254 arcsec px^{-1}, and the grism R300B, which provides a spectral coverage of $4000 - 9000$ Å and a nominal dispersion of 4.96 Å px^{-1}. The slit width was 0.6 arcsec. Long-slit spectral observations were performed on 2015 December 2 in good seeing conditions of ~ 0.8 arcsec. The slit was placed along the N-S direction, in order to minimize the effects of atmospheric differential refraction at culmination. The total exposure time was 3600 s divided into 6 exposures of 600 s each. In each of the 6 exposures the two components, ring and lensing galaxy, have been detected and in particular their spectra were not overlapping. The position of the slit was such that the spectra obtained for the ring refers to peak B.

For the pre-reduction we have used the OSIRIS Offline Pipeline Software (OOPS); sky subtraction and flux calibration were performed using IRAF[1]. We performed wavelength calibration using standard HgAr+Ne+Xe arc lamps; the resulting error on wavelength determination has been measured to be consistent with the above spectral resolution. We corrected the extracted spectra for instrumental response using observations of the spectrophotometric standard

[1]IRAF is distributed by the National Optical Astronomy Observatory, which is operated by the Association of Universities for Research in Astronomy, Inc., under cooperative agreement with the National Science Foundation

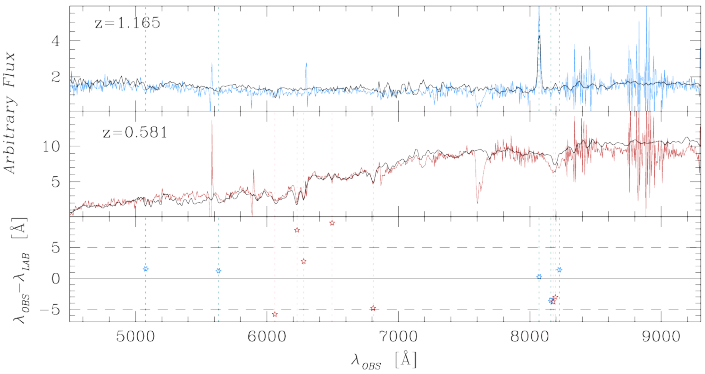

Figure 4.2: Top panel: source galaxy spectrum (in blue) with overplotted a starburst template spectrum by Calzetti et al. (1994). Middle panel: lens galaxy spectrum (in red) with overplotted an early-type galaxy template by Kinney et al. (1996). Bottom panel: measured wavelength displacement between observed and laboratory line position for the selected features (see text for details).

star GD140, a white dwarf, obtained the same night. The fluxes of this standard star are available in Massey et al. (1988).

4.5 Analysis and Discussion

In order to derive the redshifts for the two components we noted the strong emission line in the source spectrum and the 4000 Å Balmer discontinuity in the lens spectrum. This led us to choose template models for a starburst galaxy and a early-type galaxy respectively, as specified below. Following line identification, we determined redshifts.

4.5.1 Lens

Using the template spectra by Kinney et al. (1996) results that the spectrum of the lens galaxy fits well the spectrum of a S0 galaxy (see Figure 4.2), a typical early-type galaxy characterized by a large increase in flux from the UV part of the spectrum to the optical. The 4000 Å Balmer discontinuity at ~ 6330 Å is noticeable. The redshift of the lens galaxy is $z = 0.581 \pm 0.001$ and it has

been determined from the measurements of: Hη λ3835.4, Ca K λ3933.7, Ca H λ3968.5, Hδ λ4141.8, G-band λ4307.7, Mg-b2 λ5172.7, Mg-b1 λ5183.6 (marked red features from left to right in Figure 4.2 middle panel).

4.5.2 Source

For the source galaxy we used the template spectra by Calzetti et al. (1994) and we found that the spectrum best fitting our observed spectrum corresponds to a starburst galaxy in the case of *clumpy scattering slab*, where it is assumed that clumped dust is located close to the source of radiation. In such circumstances, Calzetti et al. (1994) show that scattering into the line of sight dominates over absorption by the dust, providing a significant positive contribution to the emerging radiation. This template spectrum fits well the strong OII λ3727 emission line. We also identified the following lines: FeII λ2344.0, FeII λ2600.0, HI 11 λ3770.6, OII λ3727.3,HI 10 λ3797.9 (marked blue features from left to right in Figure 4.2 upper panel). According to these features, we derived for the source galaxy a redshift of $z = 1.165 \pm 0.001$. We note that the selected slit position enable us to extract only the portion of the spectrum corresponding to peak B (see Figure 4.1); this notwithstanding, the OII emission coming from the opposite side of the ring can be easily noted in our spectra.

4.5.3 Enclosed Mass Derivation

The strong circular symmetry of our object (see Figure 4.1) suggests that it can be approximated to the case of a circularly symmetric lens, with source and lens in the line of sight. Under these assumptions, for an arbitrary mass profile M(Θ), (i.e. without assuming any particular model for the potential), we can apply the following relation (Narayan & Bartelmann 1996) and solve it for the mass.

$$\Theta_{\rm E}^2 = \frac{4{\rm G}}{{\rm c}^2}\,{\rm M}(\Theta)\,\frac{d_{\rm LS}}{d_{\rm L} d_{\rm S}} \tag{4.1}$$

Here $\Theta_{\rm E}$ is the Einstein radius in radians; M(Θ) is the mass enclosed within the Einstein radius; $d_{\rm LS}$, $d_{\rm L}$, $d_{\rm S}$ are the angular diameter distances respectively of source-lens, lens-observer and source-observer. These last quantities are related to the relative comoving distances and, in general, this relation depends on the assumed curvature of the Universe (Hogg 1999). In our case $\Omega_K = 0$ has been assumed and the resulting angular diameter distances are $d_{\rm L} = 951\,{\rm h}^{-1}$Mpc, $d_{\rm S} = 1192\,{\rm h}^{-1}$Mpc and $d_{\rm LS} = 498\,{\rm h}^{-1}$Mpc. We calculated a total mass $M_{\rm tot} = (1.86 \pm 0.23) \cdot 10^{12}\,M_\odot$ where the error on the mass (12%)

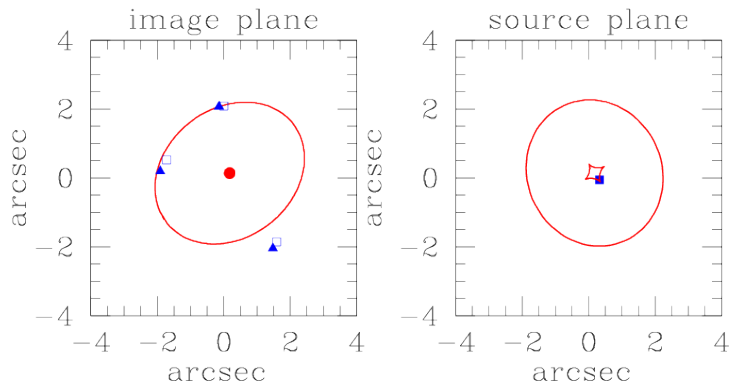

Figure 4.3: Best fitting SIE model obtained with the `gravlens/lensmodel` software. On the left (image plane): the source images positions are plotted as blue triangles, the fitted position recovered by the software as blue squares, the red central dot represents the position of the lensing galaxy and the red curve is the critical curve. On the right (source plane): the blue square represent the calculated position of the source; the caustics are shown in red.

is overwhelmingly due to the measurement error in the determination of the Einstein radius, that we have estimated to be 0.5 px which corresponds to 0.135 arcsec. The error on the redshift derives from the error estimated on the wavelength calibration which is ~ 5 Å. This value is consistent with the spectral resolution (4.96 Å px^{-1}) of the grating R300B that we used.

Under the assumption of a singular isothermal sphere (SIS) it is possible to give an estimate of the magnification of the ring: $\mu = 4\Theta_E/\delta\Theta_s$, where $\delta\Theta_s$ is the source size. From Nagy et al. (2011) the average size of a starburst galaxy in our redshift range is ~ 2 Kpc which corresponds to 0.24 arcsec. The derived magnification is ~ 36.

We determined also the mass-to-light ratio of the lens in the g band; a K-correction of 2.1 has been derived for the lens using the NED calculator (Chilingarian & Zolotukhin 2012). The resulting ratio is $\mathrm{M_{tot}/L} \sim 58\,\mathrm{M_\odot/L_\odot}$.

The former mass estimate can be improved by applying to the system a singular isothermal ellipsoid (SIE) model using the `gravlens/lensmodel` software (Keeton 2001). This software allows to fit a SIE model using only the image positions and fluxes. The obtained best-fit model is plotted in Figure 4.3. The best fit ellipticity is 0.2 calculated as $1 - q$ where q is the axis ratio; the

associated position angle is -57 deg, angle measured from North to East. The best fit χ^2 value is 6.12, calculated setting to 0 the weights relative to image fluxes. The derived Einstein radius is $\Theta_E = 2.38$ arcsec, which translates in an enclosed mass of $\sim 2.26 \cdot 10^{12}\,M_\odot$, hence in excellent agreement with our previous estimate.

4.6 Conclusions

We report the discovery of an almost complete ($\sim 300°$) circular optical Einstein ring in the constellation of Sculptor. The gravitational lens is a massive luminous red galaxy at $z = 0.581$. The source galaxy is a starburst at redshift $z = 1.165$; its spectrum is dominated by a strong OII emission line. Using these redshift determinations and the Einstein radius $\Theta_E = 2.16$ arcsec we calculated the total enclosed mass that produced the lensing effect:
$M_{tot} = (1.86 \pm 0.23) \cdot 10^{12}\,M_\odot$.

All the parameters we determined for IAC J010127-334319 are listed in Table 4.1.

5

Comparison with other Galaxies

5.1 Overview

In this final chapter it is investigated how the two dwarf spheroidal galaxies studied in this thesis, Sextans and Sculptor, place in respect to other dwarfs galaxies. But first of all we will compare the SFH, AMR and cumulative mass fraction between these two galaxies to see if there are similarities or not. Finally, attention will be placed to an important relation such as the absolute visual magnitude (M_V) vs. stellar metallicity measurement ($[Fe/H]$) and the mass-metallicity relation.

5.2 Comparison between Sextans dSph and Sculptor dSph

In this Section we compare and discuss the characteristics of the SFHs, AMRs and cumulative mass fractions of Sextans and Sculptor (Bettinelli et al. 2018; Bettinelli et al., 2019, Submitted), see Figure 5.1. It can be seen that the two galaxies have distinct SFHs especially at early times even though both show a dominant period of star formation between $13.5 - 11.8$ Gyr ago, having formed $\sim$ 50% of their total stellar mass within 12.6 and 12.4 Gyr ago for Sextans and Sculptor respectively. Both galaxies had also formed more than 95% of their total stellar mass by $\sim$ 11 Gyr ago. In Table 5.1 are listed the mass percentiles formed in Sextans and Sculptor as a function of look-back time. Given its higher mass, Sculptor has higher star formation rates at any epoch in respect to Sextans. But from Table 5.1 it can be noted that its star formation is alway more prolonged than the one of Sextans. The mean metallicities,

Table 5.1: Mass percentiles formed in Sextans and Sculptor as a function of look-back time.

Mass %	$Look-back\,Time_{Sextans}(Gyr)$	$Look-back\,Time_{Sculptor}(Gyr)$
10	13.26	13.22
20	13.11	13.05
30	12.95	12.85
40	12.80	12.65
50	12.64	12.43
60	12.43	12.20
70	12.22	12.00
80	11.92	11.70
90	11.45	11.30

though, are different. Sextans presents a mean metallicity $Fe/H \sim -1.6$, while Sculptor one is $Fe/H \sim -1.8$. The AMRs of Sextans and Sculptor present a common flat slope due to a single, major event of star formation which indicates a fast chemical enrichment in a relatively brief time interval. In this sense, Sextans and Sculptor could be classified as quenched galaxies, as defined in Revaz & Jablonka (2018) considering the final luminosity $L_V < 10^6 L_\odot$ of the systems (this is true for Sextans $L_V \sim 4.1 \times 10^5 L_\odot$ but not strictly for Sculptor $L_V \sim 1.4 \times 10^6 L_\odot$ (Irwin & Hatzidimitriou 1995)). The gravitational potential well of these galaxies is expected to be so shallow that the gas heated by the UV photons could escape the systems. Star formation is generally rapidly quenched after 2 or 3 Gyr as can be appreciated from our graphs in Figure 5.1.

5.3 Metallicity-Luminosity Plane

It is well established that dwarf galaxies follow a luminosity-metallicity relation (Grebel & Guhathakurta 1999; Grebel et al. 2003). The more luminous is a dwarf, the higher is its mean metallicity. An higher luminosity reasonably implies higher masses, so a strong enrichment is due to the possibility to retain metals because of the deeper potential wells. In Figure 5.2 we report the Figure 12 of the review by McConnachie (2012) adding the results we have obtained for Sextans and Sculptor. These galaxies present mean metallicities of $[Fe/H] \sim -1.6$ and $[Fe/H] \sim -1.8$ respectively. In Figure 5.2 it can be seen where the two galaxies loci in respect to the other dwarfs in the metallicity-luminosity plane. The higher metallicity retrieved for Sextans places it slightly above what is expected from the metallicity-luminosity relation traced by the other dwarfs. This is even more evident if compared with Sculptor in the same graph. In any case, both galaxies do not place outside the distribution of points

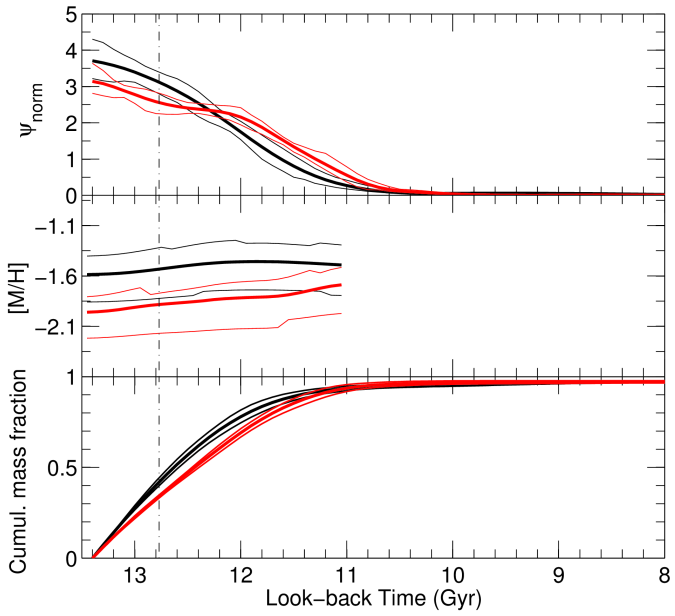

Figure 5.1: Comparison between the SFHs and the AMRs of Sextans (black lines) (Bettinelli et al. 2018) and Sculptor (red lines) (Bettinelli et al., 2019, Submitted). The SFRs have been normalized to their time integral.

traced by the whole sample.

5.4 Mass-Metallicity Relation

Finally, in this section, we will explore how Sextans and Sculptor places in the mass-metallicity plane since it is known that the average metal content of a galaxy correlates with its mass. More massive galaxies are more metal-rich than less massive galaxies, this is because the first ones are capable to retain metals in their gravitational potential wells Dekel & Silk (1986). High-mass galaxies have deep potential wells that can resist some of the expulsion of gas and metals by supernova winds, stellar winds, and galaxy-scale feedback. Low-mass galaxies such as dwarfs lack the gravity to resist these feedback mechanisms. The correlation between metallicity and mass can also be explained by a correlation between star formation efficiency and stellar mass (Matteucci 1994).

In Figure 5.3 it is reported the Figure 3 as in Hidalgo (2017) to visualize the two galaxies under study in respect to a large sample of galaxies. In the upper panel it is shown the mass-metallicity relation from spectroscopy of individual stars. As red dots are plotted also Sextans and Sculptor where the metallicity adopted is the one derived from the SFH presented in this thesis. It is remarkable the good agreement with the relation obtained from spectroscopy of resolved stars in the local environment. The gray line shows the fit obtained by Kirby et al. (2013b). Sculptor, again, match this fit, while Sextans places above what is expected. In the lower panel it is shown the fit obtained by Berg et al. (2012). In this case Sextans perfectly match the fit, while Sculptor seems to depart from the relation.

By analysing the general parameters of Sextans and Sculptor emerge many similarities.

The two dSph galaxies are located at a same distance from the MW (~ 86 Kpc for Sextans and ~ 82 Kpc for Sculptor) and have similar total masses ($\sim 4 \times 10^7\ M_\odot$ for Sextans and $\sim 3 \times 10^7\ M_\odot$ for Sculptor). The stellar mass is different, Sextans has $\sim 0.4 \times 10^6\ M_\odot$, while Sculptor almost six times more, with $\sim 2.3 \times 10^6\ M_\odot$. This fact is reflected also in the M/L_V ratio that is ~ 97 for Sextans and ~ 15 for Sculptor as calculated by Łokas (2009). This means that Sextans is highly dark matter dominated. Moreover, they have almost identical velocities in respect to the Milky Way, 72 km/s and 79 km/s for Sextans and Sculptor respectively (McConnachie 2012). It is interesting to note in this respect that a recent study by Casetti-Dinescu et al. (2018) have determined that Sextans has a low eccentricity orbit, with a moderate inclination to the Galactic plane, and a period of 3 Gyr. Sextans is now some 0.4 Gyr away from its pericenter ($r_{peri} = 75$ kpc), moving toward its apocenter

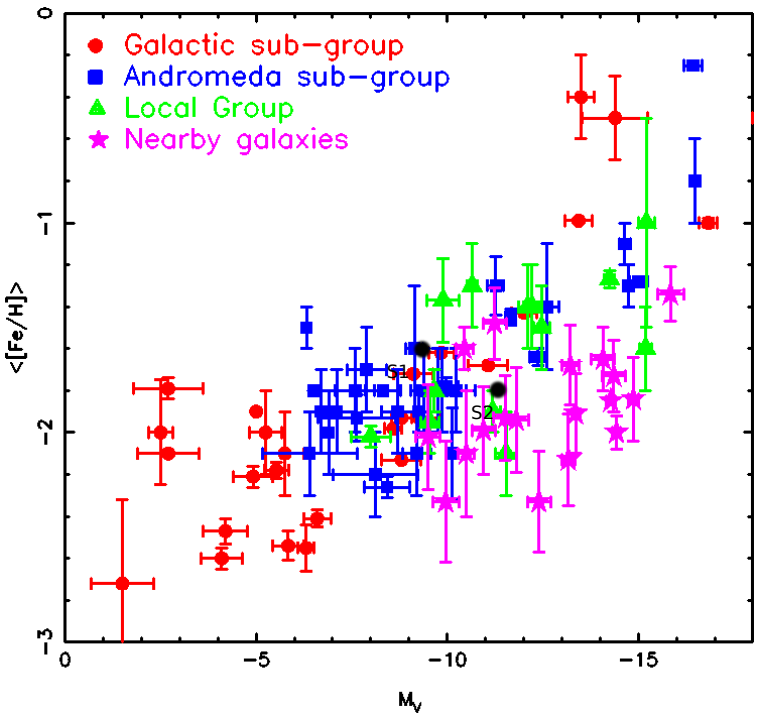

Figure 5.2: Absolute visual magnitude vs. stellar metallicity measurement for a large sample of dwarf galaxies, see Table 5 in McConnachie (2012). The black point labeled as S1 refers to Sextans and S2 to Sculptor.

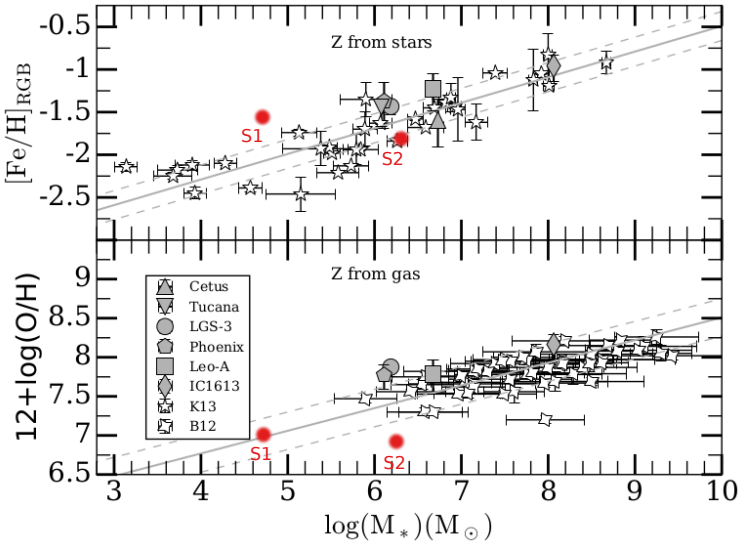

Figure 5.3: Mass-metallicity relation from spectroscopy of individual stars (upper panel) and from gas-phase metallicities (lower panel) compared with the results from the LCID dwarfs. The gray line shows the fit obtained by Kirby et al. (2013b) (upper panel) and Berg et al. (2012) (lower panel) in each case. For the LCID dwarfs, the [Fe/H] values have been converted into $\log(\mathrm{O/H})+12$ using a solar scale. Sextans and Sculptor are indicated as red dots labelled S1 and S2 respectively.

($r_{apo} = 132$ kpc). Similarly, as outlined in Sohn et al. (2017), Sculptor's orbit presents its most recent pericentric approach to the MW being $0.3 - 0.4$ Gyr ago, so very similarly to Sextans. One evident difference is the core radius. Sculptor has a core radius of ~ 6 arcmin, while the Sextans one is ~ 28 arcmin (about a factor 100 less concentrated).

Our detailed analysis of the central region of ~ 30 arcmin of Sextans has not revealed any metallicity/age gradient. As a future work we will investigate the SFHs up to a radius larger than 100 arcmin. In the case of Sculptor we have measured distinct radial time scales of star formation along a distance equal to 3 times the core radius, finding the largest period of star formation in the innermost region and the shortest one in the outermost area of our sample. So, there are strong hints that suggest the presence, in both galaxies, of an extended primordial metal poor stellar population characterized by a quite short event of star formation. In fact, we have been able to constrain it to 0.5 Gyr in Sculptor in the outermost region of our sample, while in Sextans we calculated a global duration of 0.6 Gyr, within its core radius. This indicates a possible common evolutionary path, also known as outside-in scenario, that would be capable to induce also less pronounced age and metallicity radial gradients. The slightly different configurations of the two galaxies would point to relatively different local conditions that, at remote epochs, could have strongly influenced their evolution, such as local strong UV cosmic backgroud radiation or more conceivably radiation coming from the MW.

6

Conclusions

6.1 Summary and Conclusions

In this thesis I present the research performed during this four years at the Instituto de Astrofisica de Canarias and partly at the Università degli Studi di Padova. I have completed two scientific publications strictly connected to the theme of the present thesis, i.e. the star formation of Sextans and Sculptor dwarf spheroidals. It is also presented the discovery and analysis of an Einstein ring, named 'Canarias' that has been found in serendipity on the stacked images adopted for the study of the Sculptor dSph. This last work has been published in a scientific journal too.

In particular, it has been derived the star SFH of the Sextans dwarf spheroidal galaxy based on deep archive B,I photometry taken with Suprime-Cam at Subaru telescope. The data are limited to the core radius of the galaxy. It has not been detected any metallicity gradient along the considered radial distance interval within the errors of our SFH. It has been constrained the duration of the main burst of star formation to $\sim$ 0.6 Gyr, thus indicating that the Sextans dwarf spheroidal stopped forming stars $\sim$ 12.9 Gyr ago before the end of the reionization epoch. From this analysis based on the model results by Mac Low & Ferrara (1999) and the calculation of the mechanical luminosity released from SNe during the brief episode of star formation, we can advance the hypothesis that Sextans run out most of its gas reservoirs before the end of the reionization due to gas outflows induced by SNe of type II, capable to throw out of the dwarf potential well the newly produced enriched elements and the remaining gas.

The same methodology has been applied to Sculptor, for which it has been derived the global and radial SFH based on deep g,r photometry taken with DECam at the Blanco telescope. It has been investigated how the SFH of Sculptor changes radially, subdividing in four regions the sampled area. In each region the star formation is consistent, within our age resolution, with a single burst of star formation of different duration. We find that the intrinsic duration of the episodes of star formation increases towards the centre and we provide the intrinsic duration of these bursts. The innermost region presents the longer period of star formation of ~ 1.5 Gyr, in agreement with the estimate by means of chemo-dynamical models of Kirby et al. (2009), going outwards it decreases to ~ 0.5 Gyrs. The mean metallicity retrieved is $[Fe/H] \sim -1.8$ and it is consistent with the spectroscopic measurements by Helmi et al. (2006) and Tolstoy et al. (2004). These results suggest that Sculptor continued forming stars after the reionization epoch in its central part, while in the peripheral region the majority of stars were formed before or in concomitance to the end of the reionization epoch. Our results are compatible with an outside-in scenario of dwarf galaxy formation. Finally, from the calculation of the mechanical luminosity produced by SNe we can advance the hypothesis that Sculptor has suffered a 'blow out' in its early epochs that does not completely inhibit star formation. This result, together with the constraints by Ricotti & Gnedin (2005) indicate tha Sculptor can not be strictly considered a fossil of the pre-reionization era.

From these results appears that two dSph galaxies at a same distance from the MW (~ 86 Kpc for Sextans and ~ 82 Kpc for Sculptor) and similar total masses ($\sim 4 \times 10^7$ $M_\odot$ for Sextans and $\sim 3 \times 10^7$ $M_\odot$ for Sculptor) are quite different objects. First of all, Sextans is characterized by a very large core radius of ~ 28 arcmin, along which we have not detected a metallicity/age gradient. This is in agreement also with other works in literature based on the same area. Both galaxies present radial gradients of stellar populations but at different radial scales and with different strength. In order to detect stellar population gradients in Sextans, it is necessary to analyze larger datasets, that cover a radius larger than 100 arcmin. Sculptor has a more compact stellar spatial distribution, having a core radius of ~ 6 arcmin. In this case we have measured different radial time scales of star formation along a distance equal to 3 times the core radius, indicating the largest period of star formation in the innermost region and the shortest one in the outermost area of our sample. So, in this sense, unlike the differences, there are strong hints that suggest the presence, in both galaxies, of an extended primordial metal poor stellar population characterized by a quite short event of star formation. We have been able to constrain it to 0.5 Gyr in Sculptor in the outermost region of our sample, while

in Sextans we calculated a global duration of 0.6 Gyr, within its core radius. This indicates a possible common evolutionary path, also known as outside-in scenario, that would be capable to induce also less pronounced gradients. The different configurations of the two galaxies would point to relatively different local conditions that at remote epochs could have strongly influenced their evolution, such as local strong UV cosmic backgroud radiation or more conceivably radiation coming from the MW.

Finally, it is reported the discovery of an almost complete ($\sim 300°$) circular optical Einstein ring in the constellation of Sculptor. The discovery was made serendipitously from inspecting the same stacked images (DECam) for the Sculptor's analysis. The confirmation of the object nature has been obtained by deriving spectroscopic redshifts for both components, lens and source, from observations at the 10.4 m GTC with the spectrograph OSIRIS. It has been found that the gravitational lens is a massive luminous red galaxy at $z = 0.581$, while the source galaxy is a starburst at redshift $z = 1.165$ being its spectrum dominated by a strong OII emission line. Using these redshift determinations and the Einstein radius $\Theta_E = 2.16$ arcsec we calculated the total enclosed mass that produced the lensing effect: $M_{tot} = (1.86 \pm 0.23) \cdot 10^{12} M_{\odot}$.

7

Future Work

7.1 Future Work

In this section it is briefly presented the work planned for the imminent future. It has an high priority the study of peripheral regions, up to the tidal radius, of both Sextans and Scuptor, in order to complete the detailed analysis of the innermost regions. This will be the first time that these galaxies are studied in such detail up to large distances in order to map the star formation and its variations, if present. It is important to underline that the analysis would be pursued in an uniform and consistent way with the tools described in the Appendix A.

This methodology can be applied also to the case of the Milky Way (MW) itself, in fact as a future plan it would be of extreme interest to perform a systematic analysis of the thin and thick disc of the MW at the light of the released Gaia DR2 on April 2018. Thanks to this data, which includes the photometric colour for each star, it would be possible to construct CMDs deep enough to study in detail the SFH of our Galaxy, especially the Solar neighbourhood for which the completeness is at its highest level. In fact, the main-sequence turnoff of the oldest stellar populations corresponds to an apparent magnitude of 20 mag near the outer edge of the disk (Gilmore 1999), thus permitting the full derivation of the SFH for nearly half of the MW. The feasibility of this proposed analysis has already been tested using the IAC method; Figueras et al. (2013) succeed in the attempt to use IAC-pop for the derivation of both star formation rate and age-metallicity relation Z(t) of the solar neighbourhood thin disk. It is also important to remind the fact that one of the main scientific goals

of the Gaia mission is the clarification of the origin and history of our Galaxy (Perryman et al. 2001) from the determination of the SFHs of the bulge, inner disk, Solar neighbourhood and outer halo (Hernandez et al. 2000b).

Thinking to future is impossible to not mention the imminent launch of the James Webb Space Telescope (JWST) whose observations will greatly contribute to the study of the SFHs of the nearby galaxies, including our own, exploiting the large lever arm provided by visible-infrared colours. JWST was not designed to carry out studies of resolved stellar population at visible wavelengths, however, its large aperture (guaranteeing a small core for the PSF) combined with a sampling of 32 mas in NIRCam's short wavelength channel will make JWST an highly capable followup to the HST (Brown et al. 2008, White Paper on Studying Resolved Stellar Population with JWST). Although it is not widely appreciated, the broad filters on its near-infrared camera will provide a more sensitive temperature lever than the most widely-used filters employed for deep HST imaging, thus providing better age diagnostics. In this way there will be the possibility to refine the investigation of the targets of this thesis and to extend the investigation to other objects.

8

Acknowledgements

8.1

I thank my supervisors, Sebastián, Santi and Giampaolo, who have followed me in these years and permitted to develop this research work. I would also like to thank Antonio for all his enlighting comments and discussions. My thanks go to Elena and Manuela who have accepted to be the referee of my thesis.

A special thank goes to the Instituto de Astrofisica de Canarias and to the Universidad de La Laguna that have permitted me to conduct my PhD and to the Università degli Studi di Padova for the cotutelage period.

Finally, my thanks go to my family who has always supported me in these years.

Bibliography

Abazajian, K. N., Adelman-McCarthy, J. K., Agüeros, M. A., et al. 2009, ApJS, 182, 543

Abraham, R. G., & van den Bergh, S. 2001, Science, 293, 1273

Allam, S. S., Tucker, D. L., Lin, H., et al. 2007, ApJ, 662, L51

Amorisco, N. C., Zavala, J., & de Boer, T. J. L. 2014, ApJ, 782, L39

Antilogus, P., Astier, P., Doherty, P., Guyonnet, A., & Regnault, N. 2014, Journal of Instrumentation, 9, C03048

Aparicio, A. 2002, in Astronomical Society of the Pacific Conference Series, Vol. 274, Observed HR Diagrams and Stellar Evolution, ed. T. Lejeune & J. Fernandes, 429

Aparicio, A., Carrera, R., & Martínez-Delgado, D. 2001, AJ, 122, 2524

Aparicio, A., & Gallart, C. 1995, AJ, 110, 2105

—. 2004, AJ, 128, 1465

Aparicio, A., Gallart, C., & Bertelli, G. 1997a, AJ, 114, 669

—. 1997b, AJ, 114, 680

Aparicio, A., Gallart, C., Chiosi, C., & Bertelli, G. 1996, ApJ, 469, L97

Aparicio, A., & Hidalgo, S. L. 2009, AJ, 138, 558

Aparicio, A., & Tikhonov, N. 2000, AJ, 119, 2183

Aparicio, A., Hidalgo, S. L., Skillman, E., et al. 2016, ApJ, 823, 9

Baade, W. 1944a, ApJ, 100, 147

—. 1944b, ApJ, 100, 137

Baba, H., Yasuda, N., Ichikawa, S.-I., et al. 2002, in Astronomical Society of the Pacific Conference Series, Vol. 281, Astronomical Data Analysis Software and Systems XI, ed. D. A. Bohlender, D. Durand, & T. H. Handley, 298

Babul, A., & Rees, M. J. 1992, MNRAS, 255, 346

Barkana, R., & Loeb, A. 1999, ApJ, 523, 54

Battaglia, G., Helmi, A., Tolstoy, E., et al. 2008a, ApJ, 681, L13

Battaglia, G., Irwin, M., Tolstoy, E., et al. 2008b, MNRAS, 383, 183

Battaglia, G., Tolstoy, E., Helmi, A., et al. 2011, MNRAS, 411, 1013

Becker, R. H., Fan, X., White, R. L., et al. 2001, AJ, 122, 2850

Bellazzini, M., Ferraro, F. R., & Pancino, E. 2001, MNRAS, 327, L15

Belokurov, V., Evans, N. W., Moiseev, A., et al. 2007, ApJ, 671, L9

Benítez-Llambay, A., Navarro, J. F., Abadi, M. G., et al. 2016, MNRAS, 456, 1185

Berg, D. A., Skillman, E. D., Marble, A. R., et al. 2012, ApJ, 754, 98

Bernard, E. J., Gallart, C., Monelli, M., et al. 2008, ApJ, 678, L21

Bertelli, G., Bressan, A., Chiosi, C., Fagotto, F., & Nasi, E. 1994, A&AS, 106, 275

Bertelli, G., Mateo, M., Chiosi, C., & Bressan, A. 1992, ApJ, 388, 400

Bertelli, G., & Nasi, E. 2001, AJ, 121, 1013

Bettinelli, M., Hidalgo, S. L., Cassisi, S., Aparicio, A., & Piotto, G. 2018, MNRAS, 476, 71

Bettinelli, M., Simioni, M., Aparicio, A., et al. 2016, MNRAS, 461, L67

Binggeli, B. 1994, in European Southern Observatory Conference and Workshop Proceedings, Vol. 49, European Southern Observatory Conference and Workshop Proceedings, ed. G. Meylan & P. Prugniel, 13

Blumenthal, G. R., Faber, S. M., Primack, J. R., & Rees, M. J. 1985, Nature, 313, 72

Bolton, A. S., Burles, S., Koopmans, L. V. E., et al. 2008, ApJ, 682, 964

Bouchard, A., Carignan, C., & Mashchenko, S. 2003, AJ, 126, 1295

Bouchard, A., Da Costa, G. S., & Jerjen, H. 2009, AJ, 137, 3038

Bovill, M. S., & Ricotti, M. 2009, ApJ, 693, 1859

—. 2011, ApJ, 741, 18

Boylan-Kolchin, M., Bullock, J. S., & Kaplinghat, M. 2011, MNRAS, 415, L40

Boylan-Kolchin, M., Ma, C.-P., & Quataert, E. 2008, MNRAS, 383, 93

Brown, T. M., Tumlinson, J., Geha, M., et al. 2014, ApJ, 796, 91

Bullock, J. S., Kravtsov, A. V., & Weinberg, D. H. 2000, ApJ, 539, 517

Butler, D. J., & Martínez-Delgado, D. 2005, AJ, 129, 2217

Cabanac, R. A., Valls-Gabaud, D., Jaunsen, A. O., Lidman, C., & Jerjen, H. 2005, A&A, 436, L21

Calzetti, D., Kinney, A. L., & Storchi-Bergmann, T. 1994, ApJ, 429, 582

Carignan, C., Beaulieu, S., Côté, S., Demers, S., & Mateo, M. 1998, AJ, 116, 1690

Carrera, R., Aparicio, A., Martínez-Delgado, D., & Alonso-García, J. 2002, AJ, 123, 3199

Casetti-Dinescu, D. I., Girard, T. M., & Schriefer, M. 2018, MNRAS, 473, 4064

Castelli, F., & Kurucz, R. L. 1993, in Astronomical Society of the Pacific Conference Series, Vol. 44, IAU Colloq. 138: Peculiar versus Normal Phenomena in A-type and Related Stars, ed. M. M. Dworetsky, F. Castelli, & R. Faraggiana, 496

Castelli, F., & Kurucz, R. L. 2004, ArXiv Astrophysics e-prints, astro-ph/0405087

Cattaneo, A., Dekel, A., Faber, S. M., & Guiderdoni, B. 2008, MNRAS, 389, 567

Cepa, J. 1998, Ap&SS, 263, 369

Chilingarian, I. V., & Zolotukhin, I. Y. 2012, MNRAS, 419, 1727

Chiosi, C., Bertelli, G., & Bressan, A. 1988, A&A, 196, 84

Chiosi, C., & Carraro, G. 2002, MNRAS, 335, 335

Cole, A. A., Skillman, E. D., Tolstoy, E., et al. 2007, ApJ, 659, L17

Coleman, M. G., Da Costa, G. S., & Bland-Hawthorn, J. 2005, AJ, 130, 1065

Couchman, H. M. P., & Rees, M. J. 1986, MNRAS, 221, 53

Da Costa, G. S. 1984, ApJ, 285, 483

de Boer, T. J. L., Tolstoy, E., Saha, A., et al. 2011, A&A, 528, A119

de Boer, T. J. L., Tolstoy, E., Hill, V., et al. 2012a, A&A, 544, A73

—. 2012b, A&A, 539, A103

de Vaucouleurs, G., de Vaucouleurs, A., Corwin, Jr., H. G., et al. 1991, Third Reference Catalogue of Bright Galaxies. Volume I: Explanations and references. Volume II: Data for galaxies between 0^h and 12^h. Volume III: Data for galaxies between 12^h and 24^h.

Dekel, A., & Silk, J. 1986, ApJ, 303, 39

del Pino, A., Hidalgo, S. L., Aparicio, A., et al. 2013, MNRAS, 433, 1505

Dolphin, A. 1997, New Astronomy, 2, 397

Dolphin, A. E. 2002, MNRAS, 332, 91

Dolphin, A. E., Saha, A., Claver, J., et al. 2002, AJ, 123, 3154

Efstathiou, G. 1992, MNRAS, 256, 43P

Eggen, O. J., Lynden-Bell, D., & Sandage, A. R. 1962, ApJ, 136, 748

Einasto, J., Saar, E., Kaasik, A., & Chernin, A. D. 1974, Nature, 252, 111

Eisenstein, D. J., Annis, J., Gunn, J. E., et al. 2001, AJ, 122, 2267

Ferrara, A., & Tolstoy, E. 2000, MNRAS, 313, 291

Ferraro, F. R., Fusi Pecci, F., Tosi, M., & Buonanno, R. 1989, MNRAS, 241, 433

Figueras, F., Hidalgo, S. L., Czekaj, M., et al. 2013, in Highlights of Spanish Astrophysics VII, ed. J. C. Guirado, L. M. Lara, V. Quilis, & J. Gorgas, 549–554

Flaugher, B., Diehl, H. T., Honscheid, K., et al. 2015, AJ, 150, 150

Flaugher, B. L., Abbott, T. M. C., Angstadt, R., et al. 2012, in Proc. SPIE, Vol. 8446, Ground-based and Airborne Instrumentation for Astronomy IV, 844611

Flores, R. A., & Primack, J. R. 1994, ApJ, 427, L1

Frenk, C. S., White, S. D. M., Davis, M., & Efstathiou, G. 1988, ApJ, 327, 507

Gallagher, III, J. S., Hunter, D. A., & Tutukov, A. V. 1984, ApJ, 284, 544

Gallagher, III, J. S., & Wyse, R. F. G. 1994, PASP, 106, 1225

Gallart, C., Aparicio, A., Bertelli, G., & Chiosi, C. 1996, AJ, 112, 1950

Gallart, C., Freedman, W. L., Aparicio, A., Bertelli, G., & Chiosi, C. 1999, AJ, 118, 2245

Gatto, A., Fraternali, F., Read, J. I., et al. 2013, MNRAS, 433, 2749

Geha, M., Guhathakurta, P., Rich, R. M., & Cooper, M. C. 2006, AJ, 131, 332

Geha, M., van der Marel, R. P., Guhathakurta, P., et al. 2010, ApJ, 711, 361

Gilmore, G. 1999, Baltic Astronomy, 8, 203

Girardi, L., Bressan, A., Bertelli, G., & Chiosi, C. 2000, A&AS, 141, 371

Gnedin, N. Y., & Kravtsov, A. V. 2006, ApJ, 645, 1054

Gonçalves, D. R., Magrini, L., Leisy, P., & Corradi, R. L. M. 2007, MNRAS, 375, 715

Governato, F., Brook, C., Mayer, L., et al. 2010, Nature, 463, 203

Grebel, E. K. 1997, in Reviews in Modern Astronomy, Vol. 10, Reviews in Modern Astronomy, ed. R. E. Schielicke, 29–60

Grebel, E. K. 1999, in IAU Symposium, Vol. 192, The Stellar Content of Local Group Galaxies, ed. P. Whitelock & R. Cannon, 17

Grebel, E. K. 2001, in Dwarf galaxies and their environment, ed. K. S. de Boer, R.-J. Dettmar, & U. Klein, 45

Grebel, E. K., & Gallagher, III, J. S. 2004, ApJ, 610, L89

Grebel, E. K., Gallagher, III, J. S., & Harbeck, D. 2003, AJ, 125, 1926

Grebel, E. K., & Guhathakurta, P. 1999, ApJ, 511, L101

Harbeck, D., Grebel, E. K., Holtzman, J., et al. 2001, AJ, 122, 3092

Hargreaves, J. C., Gilmore, G., Irwin, M. J., & Carter, D. 1994, MNRAS, 269, 957

Helmi, A., Irwin, M. J., Tolstoy, E., et al. 2006, ApJ, 651, L121

Hernandez, X., Gilmore, G., & Valls-Gabaud, D. 2000a, MNRAS, 317, 831

Hernandez, X., Valls-Gabaud, D., & Gilmore, G. 2000b, in Astrophysics and Space Science Library, Vol. 255, Astrophysics and Space Science Library, ed. F. Matteucci & F. Giovannelli, 517

Hewitt, J. N., Turner, E. L., Schneider, D. P., Burke, B. F., & Langston, G. I. 1988, Nature, 333, 537

Hidalgo, S., & Aparicio, A. 2016, Mem. Soc. Astron. Italiana, 87, 350

Hidalgo, S. L. 2017, A&A, 606, A115

Hidalgo, S. L., Aparicio, A., & Gallart, C. 2009, in IAU Symposium, Vol. 258, The Ages of Stars, ed. E. E. Mamajek, D. R. Soderblom, & R. F. G. Wyse, 245–252

Hidalgo, S. L., Aparicio, A., Skillman, E., et al. 2011, ApJ, 730, 14

Hidalgo, S. L., Monelli, M., Aparicio, A., et al. 2013, ApJ, 778, 103

Hodge, P. W. 1971, ARA&A, 9, 35

Hogg, D. W. 1999, ArXiv Astrophysics e-prints, astro-ph/9905116

Howley, K. M., Geha, M., Guhathakurta, P., et al. 2008, ApJ, 683, 722

Hunter, D. A., & Gallagher, III, J. S. 1986, PASP, 98, 5

Hurley-Keller, D., Mateo, M., & Grebel, E. K. 1999, ApJ, 523, L25

Hurley-Keller, D., Mateo, M., & Nemec, J. 1998, AJ, 115, 1840

Irwin, M., & Hatzidimitriou, D. 1995, MNRAS, 277, 1354

Irwin, M. J., Bunclark, P. S., Bridgeland, M. T., & McMahon, R. G. 1990, MNRAS, 244, 16P

Ivezić, Ž., Smith, J. A., Miknaitis, G., et al. 2007, AJ, 134, 973

Kaiser, N., Burgett, W., Chambers, K., et al. 2010, in Proc. SPIE, Vol. 7733, Ground-based and Airborne Telescopes III, 77330E

Katz, N. 1992, ApJ, 391, 502

Kawata, D. 2001, ApJ, 558, 598

Keeton, C. R. 2001, ArXiv Astrophysics e-prints, astro-ph/0102340

Kinney, A. L., Calzetti, D., Bohlin, R. C., et al. 1996, ApJ, 467, 38

Kirby, E. N., Boylan-Kolchin, M., Cohen, J. G., et al. 2013a, ApJ, 770, 16

Kirby, E. N., Cohen, J. G., Guhathakurta, P., et al. 2013b, ApJ, 779, 102

Kirby, E. N., Cohen, J. G., Smith, G. H., et al. 2011a, ApJ, 727, 79

Kirby, E. N., Guhathakurta, P., Bolte, M., Sneden, C., & Geha, M. C. 2009, ApJ, 705, 328

Kirby, E. N., Lanfranchi, G. A., Simon, J. D., Cohen, J. G., & Guhathakurta, P. 2011b, ApJ, 727, 78

Klypin, A., Kravtsov, A. V., Valenzuela, O., & Prada, F. 1999, ApJ, 522, 82

Kochanek, C. S., Keeton, C. R., & McLeod, B. A. 2001, ApJ, 547, 50

Kormendy, J. 1985, ApJ, 295, 73

Kormendy, J., Fisher, D. B., Cornell, M. E., & Bender, R. 2009, ApJS, 182, 216

Kroupa, P. 2002, Science, 295, 82

Lanfranchi, G. A., & Matteucci, F. 2004, MNRAS, 351, 1338

Lee, M. G. 1993, ApJ, 408, 409

Lee, M. G., Yuk, I.-S., Park, H. S., Harris, J., & Zaritsky, D. 2009, ApJ, 703, 692

Lee, M. G., Park, H. S., Park, J.-H., et al. 2003, AJ, 126, 2840

Leitherer, C., Schaerer, D., Goldader, J. D., et al. 1999, ApJS, 123, 3

Lin, H., Buckley-Geer, E., Allam, S. S., et al. 2009, ApJ, 699, 1242

Łokas, E. L. 2009, MNRAS, 394, L102

Lynden-Bell, D. 1967, MNRAS, 136, 101

Mac Low, M.-M., & Ferrara, A. 1999, ApJ, 513, 142

Maeder, A. 1974, A&A, 32, 177

Mapelli, M., Ripamonti, E., Battaglia, G., et al. 2009, MNRAS, 396, 1771

Martínez-Delgado, D., Aparicio, A., & Gallart, C. 1999, AJ, 118, 2229

Martínez-Vázquez, C. E., Monelli, M., Gallart, C., et al. 2016, MNRAS, 461, L41

Massey, P., Strobel, K., Barnes, J. V., & Anderson, E. 1988, ApJ, 328, 315

Mateo, M., Fischer, P., & Krzeminski, W. 1995, AJ, 110, 2166

Mateo, M., Nemec, J., Irwin, M., & McMahon, R. 1991, AJ, 101, 892

Mateo, M. L. 1998, ARA&A, 36, 435

Matteucci, F. 1994, A&A, 288, 57

Matteucci, F., & Recchi, S. 2001, ApJ, 558, 351

McConnachie, A. W. 2012, AJ, 144, 4

Menzies, J. W., Feast, M. W., Whitelock, P. A., & Matsunaga, N. 2011, MNRAS, 414, 3492

Mighell, K. J., & Burke, C. J. 1999, AJ, 118, 366

Mighell, K. J., & Rich, R. M. 1996, AJ, 111, 777

Miralda-Escude, J., & Lehar, J. 1992, MNRAS, 259, 31P

Miyazaki, S., Komiyama, Y., Sekiguchi, M., et al. 2002, PASJ, 54, 833

Momany, Y., Held, E. V., Saviane, I., et al. 2007, A&A, 468, 973

Monelli, M., Hidalgo, S. L., Stetson, P. B., et al. 2010a, ApJ, 720, 1225

Monelli, M., Gallart, C., Hidalgo, S. L., et al. 2010b, ApJ, 722, 1864

Monelli, M., Cassisi, S., Mapelli, M., et al. 2012, ApJ, 744, 157

Monkiewicz, J., Mould, J. R., Gallagher, III, J. S., et al. 1999, PASP, 111, 1392

Muñoz, R. R., Carlin, J. L., Frinchaboy, P. M., et al. 2006, ApJ, 650, L51

Muñoz, R. R., Frinchaboy, P. M., Majewski, S. R., et al. 2005, ApJ, 631, L137

Nagy, S. R., Law, D. R., Shapley, A. E., & Steidel, C. C. 2011, ApJ, 735, L19

Narayan, R., & Bartelmann, M. 1996, ArXiv Astrophysics e-prints, astro-ph/9606001

Navarro, J. F., Eke, V. R., & Frenk, C. S. 1996, MNRAS, 283, L72

Navarro, J. F., Frenk, C. S., & White, S. D. M. 1997, ApJ, 490, 493

Navarro, J. F., & Steinmetz, M. 1997, ApJ, 478, 13

Norris, J. E., Yong, D., Venn, K. A., et al. 2017, ApJS, 230, 27

Oñorbe, J., Boylan-Kolchin, M., Bullock, J. S., et al. 2015, MNRAS, 454, 2092

Okamoto, S., Arimoto, N., Tolstoy, E., et al. 2017, MNRAS, 467, 208

Okamoto, T., & Frenk, C. S. 2009, MNRAS, 399, L174

Ouchi, M., Shimasaku, K., Okamura, S., et al. 2004, ApJ, 611, 660

Pancino, E., Bellazzini, M., & Ferraro, F. R. 2002, in Astronomical Society of the Pacific Conference Series, Vol. 274, Observed HR Diagrams and Stellar Evolution, ed. T. Lejeune & J. Fernandes, 421

Pasetto, S., Grebel, E. K., Chiosi, C., et al. 2018, ArXiv e-prints, arXiv:1805.00486

Peebles, P. J. E., & Dicke, R. H. 1968, ApJ, 154, 891

Perryman, M. A. C., de Boer, K. S., Gilmore, G., et al. 2001, A&A, 369, 339

Piatek, S., Pryor, C., Bristow, P., et al. 2006, AJ, 131, 1445

Pietrinferni, A., Cassisi, S., Salaris, M., & Castelli, F. 2004, ApJ, 612, 168

Pietrzyński, G., Gieren, W., Szewczyk, O., et al. 2008, AJ, 135, 1993

Pineda, J. C. B., Hayward, C. C., Springel, V., & Mendes de Oliveira, C. 2017, MNRAS, 466, 63

Pontzen, A., & Governato, F. 2014, Nature, 506, 171

Prada, F., & Burkert, A. 2002, ApJ, 564, L73

Queloz, D., Dubath, P., & Pasquini, L. 1995, A&A, 300, 31

Renzini, A., & Buzzoni, A. 1986, in Astrophysics and Space Science Library, Vol. 122, Spectral Evolution of Galaxies, ed. C. Chiosi & A. Renzini, 195–231

Revaz, Y., & Jablonka, P. 2018, ArXiv e-prints, arXiv:1801.06222

Revaz, Y., Jablonka, P., Sawala, T., et al. 2009, A&A, 501, 189

Richardson, T., & Fairbairn, M. 2014, MNRAS, 441, 1584

Ricotti, M., & Gnedin, N. Y. 2005, ApJ, 629, 259

Rizzi, L., Held, E. V., Bertelli, G., & Saviane, I. 2004, Mem. Soc. Astron. Italiana, 75, 110

Roderick, T. A., Jerjen, H., Da Costa, G. S., & Mackey, A. D. 2016, MNRAS, 460, 30

Sage, L. J., Welch, G. A., & Mitchell, G. F. 1998, ApJ, 507, 726

Salaris, M., & Cassisi, S. 2005, Evolution of Stars and Stellar Populations, 400

Sawala, T., Scannapieco, C., Maio, U., & White, S. 2010, MNRAS, 402, 1599

Sawala, T., Frenk, C. S., Fattahi, A., et al. 2016, MNRAS, 457, 1931

Schlafly, E. F., & Finkbeiner, D. P. 2011, ApJ, 737, 103

Schlegel, D. J., Finkbeiner, D. P., & Davis, M. 1998, ApJ, 500, 525

Seaman, R. L., De La Pena, M., Zarate, N., & Lauer, T. R. 2002, in Proc. SPIE, Vol. 4846, Virtual Observatories, ed. A. S. Szalay, 182–188

Searle, L., Sargent, W. L. W., & Bagnuolo, W. G. 1973, ApJ, 179, 427

Shapley, H. 1938, Harvard College Observatory Bulletin, 908, 1

Shetrone, M. D., Siegel, M. H., Cook, D. O., & Bosler, T. 2009, AJ, 137, 62

Smail, I., Swinbank, A. M., Richard, J., et al. 2007, ApJ, 654, L33

Smecker-Hane, T. A., Marsteller, B., Cole, A., Bullock, J., & Gallagher, J. S. 2009, in Bulletin of the American Astronomical Society, Vol. 41, American Astronomical Society Meeting Abstracts #213, 235

Smecker-Hane, T. A., Stetson, P. B., Hesser, J. E., & Vandenberg, D. A. 1996, in Astronomical Society of the Pacific Conference Series, Vol. 98, From Stars to Galaxies: the Impact of Stellar Physics on Galaxy Evolution, ed. C. Leitherer, U. Fritze-von-Alvensleben, & J. Huchra, 328

Sohn, S. T., Patel, E., Besla, G., et al. 2017, ApJ, 849, 93

Somerville, R. S. 2002, ApJ, 572, L23

Stark, D. P., Auger, M., Belokurov, V., et al. 2013, MNRAS, 436, 1040

Stetson, P. B. 1993, in IAU Colloq. 136: Stellar Photometry - Current Techniques and Future Developments, ed. C. J. Butler & I. Elliott, Vol. 136, 291

Stetson, P. B. 2000, PASP, 112, 925

—. 2005, PASP, 117, 563

Stetson, P. B., Davis, L. E., & Crabtree, D. R. 1990, in Astronomical Society of the Pacific Conference Series, Vol. 8, CCDs in astronomy, ed. G. H. Jacoby, 289–304

Strigari, L. E., Frenk, C. S., & White, S. D. M. 2014, ArXiv e-prints, arXiv:1406.6079

—. 2018, ArXiv e-prints, arXiv:1801.07343

Tammann, G. A. 1994, in European Southern Observatory Conference and Workshop Proceedings, Vol. 49, European Southern Observatory Conference and Workshop Proceedings, ed. G. Meylan & P. Prugniel, 3

Tassis, K., Abel, T., Bryan, G. L., & Norman, M. L. 2003, ApJ, 587, 13

Thomas, D., Maraston, C., Schawinski, K., Sarzi, M., & Silk, J. 2010, MNRAS, 404, 1775

Tolstoy, E., Hill, V., & Tosi, M. 2009, ARA&A, 47, 371

Tolstoy, E., & Saha, A. 1996, ApJ, 462, 672

Tolstoy, E., Irwin, M. J., Helmi, A., et al. 2004, ApJ, 617, L119

Tosi, M., Greggio, L., Marconi, G., & Focardi, P. 1991, AJ, 102, 951

Valdes, F., Gruendl, R., & DES Project. 2014, in Astronomical Society of the Pacific Conference Series, Vol. 485, Astronomical Data Analysis Software and Systems XXIII, ed. N. Manset & P. Forshay, 379

Vallenari, A., Bertelli, G., & Schmidtobreick, L. 2000, A&A, 361, 73

Vallenari, A., Chiosi, C., Bertelli, G., Aparicio, A., & Ortolani, S. 1996a, A&A, 309, 367

Vallenari, A., Chiosi, C., Bertelli, G., & Ortolani, S. 1996b, A&A, 309, 358

van den Bergh, S. 1999, A&A Rev., 9, 273

Walker, M. G., Mateo, M., Olszewski, E. W., et al. 2006a, AJ, 131, 2114

—. 2007, ApJ, 667, L53

—. 2006b, ApJ, 642, L41

—. 2009, ApJ, 704, 1274

Walker, M. G., & Peñarrubia, J. 2011, ApJ, 742, 20

Warren, S. J., Hewett, P. C., Lewis, G. F., et al. 1996, MNRAS, 278, 139

Weisz, D. R., & Boylan-Kolchin, M. 2017, MNRAS, 469, L83

Westfall, K. B., Majewski, S. R., Ostheimer, J. C., et al. 2006, AJ, 131, 375

White, S. D. M., & Rees, M. J. 1978, MNRAS, 183, 341

Yagi, M., Kashikawa, N., Sekiguchi, M., et al. 2002, AJ, 123, 66

A

Methodology for the Derivation of the Star Formation History from the Colour-Magnitude Diagram of Resolved Stellar Systems

A.1 The History of Star Formation Histories

The importance of the study of the stellar populations in dwarf galaxies was initiated by the pioneering works by Baade who resolved for the first time the stars of dwarf satellite galaxies of M31 (Baade 1944b; Baade 1944a). Since then, and with the improvements in observational facilities, the understanding of how galaxies form has undergone a significant progress. Many approaches have been followed in order to derive the SFH of galaxies.

It is important to recall the earliest work by Searle et al. (1973) who firstly determined quantitatively how the colour of the integrated light of different galaxy types is connected to their SFH. Subsequently, this work has been extended in Gallagher, Hunter and collaborators (Gallagher et al. 1984; Hunter & Gallagher 1986) who used various indicators to estimate the star formation rates at different epochs for large samples of dwarfs.

But only with the resolution of new generation telescopes (HST) and detectors that has been possible to measure individual stars even in the crowdest fields of external galaxies and to construct their CMD. The CMD is one of

the most powerful tool in the study of a stellar system because it encloses all the relevant evolution parameters, such as the ages, mass, initial mass function (IMF) and chemical composition. About thirty years ago stellar age dating was performed through isochrone fitting, which is appropriate for simple stellar populations (SSPs), that means, an assembly of coeval, initially chemically homogeneous, single stars, such as star clusters (Renzini & Buzzoni 1986). This technique is inadequate for composite populations of galaxies, where many subsequent generations of stars with possibly different initial mass function, metallicity, reddening and distances, contribute to the morphology of the observational CMD. In order to derive reliable SFHs for these systems has been developed a new method, the so called synthetic CMD method.

A.1.1 The Synthetic Colour-Magnitude Analysis

The synthetic CMD method is based on the comparison of observed CMDs with theoretical ones, created via Monte Carlo based extractions from isochrones for a variety of star formation laws, IMFs, binary fractions etc.

The first to compute a synthetic CMD using a Monte Carlo technique was Maeder (1974). Chiosi et al. (1988) presented the first application of the Padova synthetic CMD code, called ZVAR Bertelli et al. (1992), that has been extensively used for the derivation of the SFH (Aparicio et al. 1996, Gallart et al. 1996, Vallenari et al. 1996a, Vallenari et al. 1996b, Aparicio et al. 1997b, Aparicio et al. 1997a, Hurley-Keller et al. 1998, Gallart et al. 1999, Aparicio & Tikhonov 2000, Vallenari et al. 2000, Bertelli & Nasi 2001). Ferraro et al. (1989) and Tosi et al. (1991) used for the first time the luminosity functions derived from synthetich CMDs to draw recent SFHs in dIrr galaxies. Bertelli et al. (1992) have been the first deriving the SFH for the LMC through the detailed morphology of the CMDs and through three ratios of star counts in different areas of the synthetic and observed CMD (known also as the R-method).

Dolphin (1997) and Aparicio et al. (1997b) introduced a new method for the derivation of SFH. Rather than adopting traditional methods of creating synthetic CMDs with various SFHs, the approach taken is to create a set of CMDs which can be combined linearly to reproduce almost any SFH, and use a numerical fit to solve the problem. All the above mentioned works use luminosity functions, colour distributions and the general CMD morphology to constrain the underlying SFH. The ratio of star counts in the various areas of the CMD have been used to determine both SFR and IMF (Bertelli et al. 1992). Synthetic and observational CMDs are parametrized; the best solution for the SFH corresponds to an extreme in a merit function involving these parameters (Aparicio 2002). This kind of approach takes into consideration all

the properties and uncertainties of stellar evolution models but it lacks a statistical criterion for the evaluation of the best solution and the corresponding uncertainties.
Other authors, in fact, proposed a purely statistical method, using a form of likelihood analysis to compare the simulated and observed CMDs; this method does not provide a unique solution for the SFH but it can limit the range of possible scenarios (Tolstoy & Saha 1996; Hernandez et al. 2000a; Dolphin 2002). Recently, Pasetto et al. (2018) proposed a new model, called GalMod, which is a theoretical population synthesis model able to simulate synthetic surveys of the Milky Way, M31, and able to generate initial conditions for quasi-equilibrium collisionless models. GalMod assumes the Galaxy to be a discrete superposition of several composite stellar populations (CSPs) representing a few nominal significant stellar populations: the thin disk, the thick disk, the stellar halo and the bulge. GalMod immerses these CSPs in a single DM halo component and a hot coronal gas component . A parametric model for the modeled galaxy gravitational potential is computed to secure consistency with the density profiles by solving the Poisson equation. These density profiles are used to generate synthetic Hertzsprung-Russell and CMDs in several photometric bands. Finally, the gravitational potential is used to realize the stellar kinematics.

In the following Sections it will be described in detail the method used in the derivation of the SFHs based on the prescription outlined in Aparicio & Hidalgo (2009) and Hidalgo et al. (2011).

A.2 Basic Concepts and Definitions

It is defined the SFH as a function $\psi(t, z)$ of the time and metallicity, such that $\psi(t, z)\, dtdz$ is the number of stars formed at time t' in the interval $t < t' \leq t+dt$ and with metallicity z' in the interval $z < z' \leq z+dz$, per unit time and metallicity.
$\psi(t, z)$ is a distribution function and can be identified with the usual star formation rate (SFR), but as a function of both time and metallicity.

There are several other functions and parameters related to the SFH that are considered as auxiliary. The IMF, $\phi(m)$ and a function accounting for the frequency and relative mass distribution of binary stars, $\beta(f, q)$, are the main ones. The solution found for the SFH depends on the assumptions made for these functions. Other parameters affecting the solution of $\psi(t, z)$ are distance and reddening, including differential reddening, that are sources of uncertainty linked to the physical properties (Aparicio et al. 2016). But the strongest limitation comes from observational data being related to photon counting statistics,

defective flat-field corrections and sampling the point-spread function (PSF). As a result the photometry is limited is depth and completeness.
Another important source of uncertainty is deeply connected to the methodology used to derive the SFH, in other words the robustness of the method including the accuracy of the stellar evolution libraries from which synthetic populations are simulated as well as the way the best solution is reached. All the above effects combined limit the time resolution and are responsible for the inaccuracies in age determination in the final SFH solutions.

A.3 The Algorithms for the Obtaintion of the Star Formation History

In this section it is explained step-by-step the procedure which has been followed for the derivation of the SFH, in particular paying attention to the various algorithms and the tasks they play. In Figure A.1 can be visualized a summary of the standard execution in form of flow chart. In the following are listed the algorithms used for the derivation of the SFH and their function in the derivation of the SFH.

- Generating the global synthetic stellar population, that means the model (IAC-star).
- Simulating observational effect on the model (obsersin).
- Parametrization and sampling of model and observational data (minniac).
- Solving the equations (IAC-pop).

A.3.1 IAC-star

IAC-star Aparicio & Gallart (2004) is a code that generates synthetic CMDs (sCMDs). Composite stellar populations are calculated on a star-by-star basis, by computing the luminosity, effective temperature, and gravity of each star by direct bilogarithmic interpolation in the metallicity and age grid of a library of stellar evolution tracks. Visual (broadband and HST) and infrared magnitudes are also provided for each star after applying bolometric corrections. The Padova stellar evolution libraries of Bertelli et al. (1994) and Girardi et al. (2000), respectively, and the Teramo stellar evolution library by Pietrinferni et al. (2004), as well as various bolometric corrections libraries are used. The algorithm is in intended to be as general as possible and allows a variety of

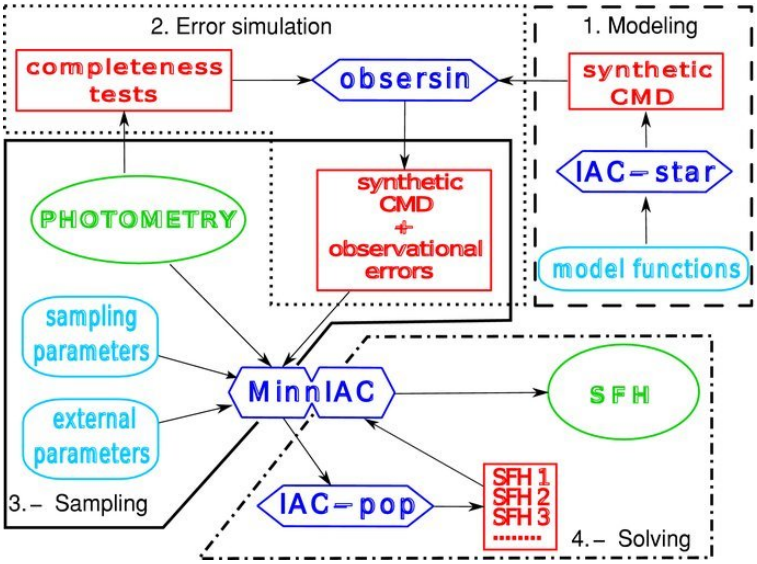

Figure A.1: Data flow diagram followed to obtain the SFHs of the galaxies. Figure from Hidalgo et al. (2011).

imputs for the IMF, SFR, metallicity law and binarity. In summary, IAC-star is used to generate a global synthetic stellar population with a large number of stars with ages and metallicities with a constant distribution over the full interval of variation of $\psi(t, z)$ in time and metallicity.

A.3.2 Obsersin

Once sCMD is generated, in order to compare it to the observational CMD (oCMD), observational effects must be simulated. This step is performed by *obsersin* (Hidalgo et al. 2011) which makes use of the results deriving from the completeness tests. Completeness tests are done by injecting a list of false stars in the observed images and recovering them using the same photometric procedure (for example the same PSF) used for the photometry of real stars. From the list of unrecovered stars and the difference between the injected (m_i) and recovered magnitudes (m_r), *obsersin* uses the following procedure to simulate the observational effects: for any stars from the sCMD with magnitude m_s, a list of false stars with $|m_i - m_s| \leq \epsilon$ is created for each filter, with ϵ being a free input searching interval. From the stars in common to both filters, a single false star is selected by a simple random sampling. If m'_i and m'_r are the injected and recovered magnitudes of the selected false star in a given filter, then $m^e_s = m_s + m'_i - m'_r$ will be the magnitude of the synthetic star with the observational effects simulated. In this way the observational effects are simulated in sCMD star by star.

A.3.3 MinnIAC

IAC-pop uses the method introduced in Aparicio et al. (1997b) for the derivation of SFH, which can be given as a linear combination of simple populations. A SSP is defined by a number of stars with ages and metallicities within small intervals (see Figure A.2). They constitute a set of $n \times m$ models with no star in common between any two of them. Arbitrary stellar populations can be obtained by a linear comination with non-negative coefficients of the simple model of this set. Each SSPs has a CMD associated that is called partial model CMD (pCMD).

With this definition, a sCMD is formed for the sum of all the pCMDs. In order to compare the pCMD with the oCMD, it is defined a set of boxes and stars are counted insiede them. Moreover, in the CMD, are defined several regions, called *bundles*. Each of them is sampled by a uniform grid, but the grid size can differ from one bundle to another, as shown in Figure A.3.

An array M^j_i, containing the number of stars from partial model i populat-

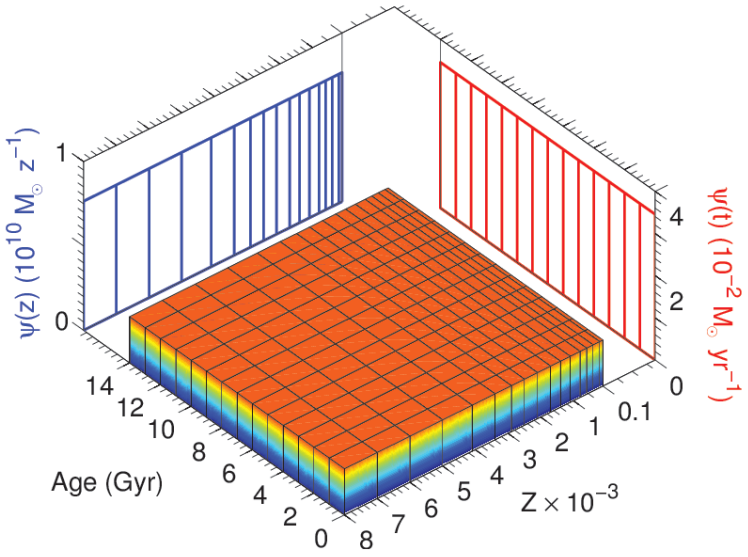

Figure A.2: SFH of the global synthetic population associated with the sCMD. The bars show the SSPs in which the global one has been divided.

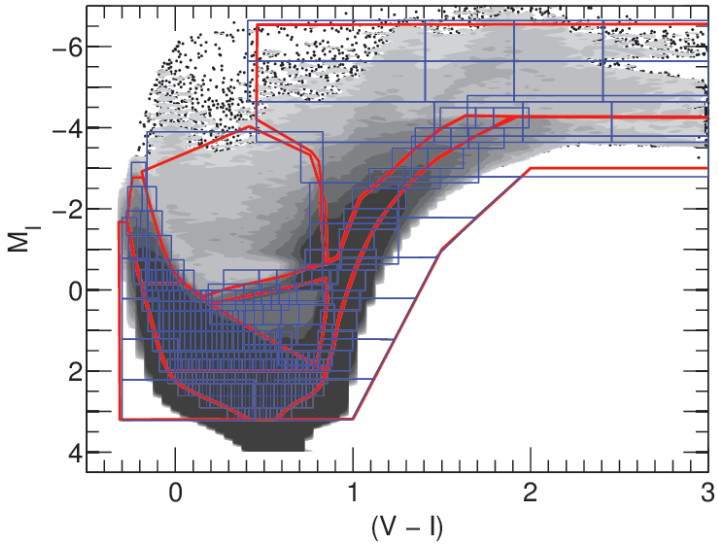

Figure A.3: CMD of a global synthetic population (sCMD). Bundles are shown in red and the grid in blue.

ing the CMD box j is computed. The same operation is made in the oCMD, producing a vector O^j which contains the number of observed stars in the box j. This step defines the parametrization of the CMD. The process is repeated for all the pCMD included in the sCMD and gives the arrays M_i^j, containing the number of stars from partial model i populating the pCMD box j, and O^j, containing the number observed stars in box j. MinnIAC is used to perform this parametrization. MinnIAC minimizes also the dependency of the results on the selection of SSPs and on the size and position of the boxes by introducing offsets in age and metallicity bins which define the SSPs. The age and metallicity interval for each SSPs is fixed.

In addition, for each set of SSPs and/or size and position of the sampling boxes, *MinnIAC* can introduce an offset in colour and magnitude in the oCMD. For each new colour-magnitude point, the process described above is repeated. This produces a manifold of input files which are used by IAC-pop (read in Section A.3.4) to solve the SFH. It is called *model parametrization* to each set of SSPs, position and seze of boxes, and colour-magnitude point. Each model parametrization has associated with it the arrays defined above, M_i^j and O^j.

A.3.4 IAC-pop

With the information provided by *minniac*, the distribution of stars in the CMDs can be calculated for any model SFH as a linear combination of the M_i^j values:

$$M^j = A \sum_i \alpha_i M_i^j \tag{A.1}$$

Where $\alpha_i \geq 0$. A is a scaling constant.
The SFH that best matches the distribution O^j, of the observational CMD can be found using a merit function. In particular Mighell's χ^2_γ (Mighell & Burke 1999) is used:

$$\chi^2_\gamma = A \sum_j \frac{(O^j + min(O^j, 1) - M^j)^2}{O^j + 1} \tag{A.2}$$

It is used $\chi^2_\nu = \chi^2_\gamma / \nu$, where ν is the nuber of freedom degrees. In this case is used $\nu = \kappa - (n \times m)$, where κ is the number of boxes defined in the CMD. The minimization of the χ^2_ν provides the best solution as a set of α_i values. IAC-pop makes use of a genetic algorithm for an efficient searching of the χ^2_ν minimum. This is required due to the large number of the problem dimensions $(n \times m)$.

The solution SFH can be written as

$$\psi(t,z) = A\sum_i \alpha_i \psi_i \tag{A.3}$$

where ψ_i refers to partial model im with i taking values from 1 to $n \times m$, and A is a scaling constant.